

**On the nature and role of absorption and
continuum reprocessing in the X-ray spectra of
obscured Seyfert galaxies**

Nicholas Schurch

Thesis submitted for the degree of
Doctor of Philosophy
at the University of Leicester.

January 2003

X-ray and Observational Astronomy Group
Department of Physics and Astronomy
University of Leicester

UMI Number: U601154

All rights reserved

INFORMATION TO ALL USERS

The quality of this reproduction is dependent upon the quality of the copy submitted.

In the unlikely event that the author did not send a complete manuscript and there are missing pages, these will be noted. Also, if material had to be removed, a note will indicate the deletion.



UMI U601154

Published by ProQuest LLC 2013. Copyright in the Dissertation held by the Author.
Microform Edition © ProQuest LLC.

All rights reserved. This work is protected against
unauthorized copying under Title 17, United States Code.



ProQuest LLC
789 East Eisenhower Parkway
P.O. Box 1346
Ann Arbor, MI 48106-1346

On the nature and role of absorption and continuum reprocessing in the X-ray spectra of obscured Seyfert galaxies

Nicholas J E Schurch

ABSTRACT

This thesis presents an investigation of the X-ray properties of four nearby galaxies, NGC 4151, NGC 7582, Mrk 3 and NGC 4945, all of which harbour a bright, heavily obscured Seyfert nucleus. It explores the implications of the results from these sources for heavily obscured active galactic nuclei (AGN) in general.

The work focuses largely on data from the *XMM-Newton* X-ray satellite, concentrating initially on hard X-ray spectra from the EPIC CCD cameras. The analysis emphasises the complex nature of the X-ray absorption in NGC 4151 and highlights the massive impact that absorption has on the observed X-ray spectrum and variability of all four sources. The range of column densities exhibited (10^{23} cm^{-2} to $>10^{24} \text{ cm}^{-2}$) encompasses both Compton-thin, continuum-dominated sources (such as NGC 4151) and Compton-thick, reflection-dominated sources (*e.g.* Mrk 3 and NGC 4945). The often-subtle role that Compton reflection plays in the X-ray spectrum and variability of these sources is discussed in detail. The source spectra, in each case, contain an intrinsically narrow, neutral, iron $K\alpha$ line emission and a sharp iron K edge, adding to the growing body of evidence which suggests that iron reprocessing features are ubiquitous constituents of the hard X-ray spectra of AGN. The analysis of NGC 4945 demonstrates the enormous impact that a nuclear starburst can have on the X-ray properties of AGN. A preliminary analysis of the soft X-ray spectrum of NGC 4151, revealed by the high spectral resolution *XMM-Newton* RGS instruments, shows the spectrum to be completely dominated by line emission and radiative recombination continua from hydrogen-like and helium-like ions. It is argued that the soft emission originates in photoionized and photoexcited gas located in X-ray/optical ionization cones.

The observational findings presented in this thesis are all generally consistent with the unified AGN picture, in which the major differences between the sources are produced by different orientations with respect to our line-of-sight.

Dedication

Dedicated, from the depths of my heart, to Mum and Dad, my brothers and to those friends who know me best.

“I was just guessing at numbers and figures
Pulling the puzzles apart
Questions of science, science and progress
Do not speak as loud as my heart”

The Scientist - Coldplay

Acknowledgements

First and foremost I'd like to thank my Ph.D supervisor, Bob Warwick. I owe Bob a great debt of gratitude. Without his understanding, guidance, patience, support and endless efforts to help me improve my scientific skills (and my english!), this thesis would have not have been possible. Thank you Bob for knowing when to encourage me, when to put the brakes on and for being the best supervisor I could possibly have asked for.

I also owe a deep debt to my family and I want to thank them all for their love and for being there for all the times I needed them, my family is my rock. I particularly wish to thank Dad for instilling in me a curiosity in the world that has driven me to, and through, this Ph.D and Mum for her open and honest appraisal of any issue I raised with her. Together, their unstinting support, emotionally, intellectually and (not least) financially along with their determination to allow me and my brothers to follow our dreams is something that I am profoundly grateful for. A big thanks also goes to my brothers, Matthew and Chris, for providing an unignorable distraction when I needed it!

To the old 'gang' in Thame, particularly Ricky Sutton, Portvale fan and Pro-Evo soccer star - long may we all be friends, keep in touch (particularly Dr Percy, may he always be remembered). A "bigup wicked" to the Bristol boys and girls - they were times I will never forget (especially drunk Micro-machines at 2 am and the time when Phil...). To assorted other close friends, particularly those in London (Evil Cate, Andy Smith, Joy Judge) and Birmingham (Alex, the Ingleys, Phil & Al and their kids) - thank you for some great times. It is a privilege to know each and every one of you!

I want to send a particularly heartfelt "thank you" out to Richard "funky bear" Ingley, Illya Teideman and Paul Burnham for being the kind of friends that we all wish we had more of. You were there when I needed you, giving me perspective and keeping me sane. You are always welcome wherever I am in life - I owe you.

I'd like to thank all the people that I have had the chance to work with during my time at Leicester, in particular my office mates, both old and new, and the postdocs for providing ample distraction from my work! Thanks to Simon V for teaching me a lot of what I now know. To Kev, for always being there to threaten the computers and for looking smug at my feeble attempts to play chess. To Daz, for many "enlivening discussions" and for often being the other half of the feeble chess games. To Alex, for his single-word contribution to this work (it wouldn't be the same without that word!). To Simon G, for introducing the inter-office XBlast and nearly delaying this thesis considerably. I'd like to thank Kim, Leigh, Pam and Charlotte for putting up with me over the past two or three years and finally to Andrew and Ann-Marie for showing the kind of enthusiasm that only new Ph.D students can show. I also wish to express my gratitude to the postdocs for their help, teaching and guidance, in particular Tim Roberts for his assistance and work on chapter 5 of this thesis and other projects. I'd also like to thank Paula, two and a half years is a long time - look after Austin for me.

I've learnt a lot from you all. You've all been a fine bunch, good drinking and sporting buddies and I will always have fond memories of curry lunches (thank you Taj!), five-aside football and many a fine pint.

On a final note, the XBlast Boyz (JNR, Milky, Saggy, Irish and Dazzler) deserve a special mention. Without them Friday afternoons, and indeed many other afternoons, would have been a lot less bearable (and a lot more productive!). And last (but by no means least) a fond thank you to Amber for watching the sunrise with me, on a cold day.

Declaration

I hereby declare that no part of this thesis has been previously submitted to this or any other university as part of the requirements for a higher degree. The work described herein was conducted by the undersigned except for contributions from colleagues and other workers who are acknowledged in the text.

Nicholas J. E. Schurch
January 2003

Contents

1	Introduction	1
1.1	Overview: Obscured AGN and the unified picture	1
1.2	Heavily obscured AGN; an historical perspective	1
1.3	The current AGN unification picture	12
1.4	The aims of this thesis	15
2	Instrumentation and Physical Processes	17
2.1	Overview: The capabilities of <i>XMM-Newton</i> and physical processes in AGN	17
2.2	The <i>XMM-Newton</i> X-ray observatory	18
2.2.1	Details of the EPIC MOS and PN cameras	19
2.2.2	Details of the RGS instruments	21
2.3	A comparison between <i>XMM-Newton</i> and other X-ray observatories	23
2.3.1	X-ray imaging	23
2.3.2	X-ray spectroscopy	25
2.3.3	Cross-calibration between X-ray satellites	30
2.4	Physical processes in AGN	30

2.4.1	Photoelectric absorption	31
2.4.2	Fluorescent line emission	32
2.4.3	Compton scattering and its inverse	34
3	The hard X-ray spectrum of NGC 4151	38
3.1	Overview: A complex mix of absorption, continuum and reprocessed continuum features.	38
3.2	NGC 4151	39
3.3	The <i>BeppoSAX</i> data and the spectral template model	40
3.4	The <i>ASCA</i> long-look observation	43
3.4.1	Fitting the spectral template model	45
3.4.2	Modelling the spectral variability	47
3.5	The results from <i>BeppoSAX</i> and <i>ASCA</i>	50
3.5.1	The physical state of the warm absorber	50
3.5.2	The properties of the iron $K\alpha$ line	52
3.5.3	The impact of Compton reflection	53
3.5.4	The spectral index versus flux correlation	54
3.6	Conclusions from <i>BeppoSAX</i> and <i>ASCA</i>	55
3.7	The <i>XMM-Newton</i> observations	57
3.7.1	The light-curve	57
3.7.2	The spectral analysis	58
3.8	Details of the <i>XMM-Newton</i> spectrum	61
3.8.1	The iron $K\alpha$ line profile	62
3.8.2	The iron $K\alpha$ line flux	63

3.8.3	The intrinsic width of the narrow iron $K\alpha$ line	64
3.8.4	The deep iron edge - a clue to iron over abundance.	65
3.9	Conclusions from <i>XMM-Newton</i>	65
4	The hard X-ray spectra of Markarian 3 and NGC 7582	67
4.1	Overview: Increasing the absorption.	67
4.2	NGC 7582	68
4.2.1	The <i>XMM-Newton</i> and <i>Chandra</i> observations	69
4.2.2	The light-curve	72
4.2.3	The spectral analysis	72
4.3	Markarian 3	76
4.3.1	The <i>XMM-Newton</i> observations	77
4.3.2	The spectral analysis	78
4.4	Discussion	80
4.4.1	The impact of heavy absorption on NGC 7582 and Mrk 3	80
4.4.2	The implications of Compton reflection	83
4.4.3	Details of the iron $K\alpha$ line	85
4.5	Conclusions from NGC 7582 and Mrk 3	86
5	The hard X-ray spectrum of NGC 4945	87
5.1	Overview: Increasing the absorption and confusing the spectrum!	87
5.2	NGC 4945	88
5.3	The observations	88

5.3.1	The <i>Chandra</i> observation	88
5.3.2	The <i>XMM-Newton</i> observation	89
5.4	Joint imaging with <i>Chandra</i> and <i>XMM-Newton</i>	89
5.5	Joint spectroscopy with <i>Chandra</i> and <i>XMM-Newton</i>	90
5.5.1	The <i>Chandra</i> AGN spectrum	90
5.5.2	The <i>Chandra</i> starburst/X-ray plume spectrum	93
5.5.3	Joint fitting of the composite <i>XMM-Newton</i> and <i>Chandra</i> spectra	94
5.6	Discussion	96
5.6.1	The reprocessing of the AGN continuum	96
5.6.2	The nuclear starburst	97
5.6.3	The X-ray plume	98
5.7	Conclusions	98
6	The soft X-ray spectrum of NGC 4151	100
6.1	Overview	100
6.2	The soft X-ray spectrum of NGC 4151	101
6.2.1	NGC 4151	101
6.3	The <i>XMM-Newton</i> RGS observations of NGC 4151	102
6.4	Modelling the RGS spectrum of NGC 4151	102
6.4.1	The emission lines	104
6.4.2	Temperature diagnostics with radiative recombination continua	104
6.4.3	Plasma diagnostics with helium-like triplets	107
6.4.4	The ionization cone model	108

6.4.5	Fitting the ionization cone model to the RGS spectra	110
6.5	A comparison with NGC 1068 and Mrk 3	112
6.5.1	The comparison with the <i>XMM-Newton</i> RGS spectrum of NGC 1068	112
6.5.2	The comparison with the <i>Chandra</i> HETG observation of Mrk 3	113
6.6	A brief comparison with the <i>XMM-Newton</i> EPIC spectra	114
6.7	Preliminary conclusions from the RGS spectra of NGC 4151	115
7	Final words	118
7.1	Overview: Conclusions and issues for the future	118
7.2	Specific conclusions from this thesis	119
7.3	Five questions for the future	121
	References	126

Chapter 1

Introduction

1.1 Overview: Obscured AGN and the unified picture

Despite the fact that most (if not all) nearby galaxies appear to contain a central supermassive black hole (Magorrian *et al.* 1998), the vast majority of the total energy output of nearby normal galaxies can be attributed solely to their intrinsic stellar populations. Some galaxies however, show optically bright, unresolved nuclear point sources which can be up to a thousand times more luminous than the underlying galaxy (bolometric luminosities between 10^{41} - 10^{48} erg s⁻¹). Optical and X-ray variability indicates that the luminosity from these unresolved nuclear point sources, known as Active Galactic Nuclei (hereafter AGN), must originate from within a region of $\lesssim 1$ pc (3.086×10^{18} cm) in radius. The term AGN encompasses a wide range of objects that often show remarkably different properties. In fact the full complement of AGN constitutes a zoo of different taxonomies and observed properties (Lawrence 1987).

The rest of this chapter provides a brief introduction to the subject of heavily absorbed AGN and the relevance of X-ray observations. Section 1.2 gives a brief summary of the history behind the attempt to unify the plethora of empirically defined AGN types, with an emphasis on the X-ray measurements. Section 1.3 presents the current unified picture of AGN and the components that make up this picture. Finally, Section 1.4 details the overall aims and structure of the rest of the thesis.

1.2 Heavily obscured AGN; an historical perspective

The history of heavily obscured AGN is intimately entwined with that of AGN unification. Indeed, the putative molecular torus present in the unified picture of AGN is solely responsible for the gross distinc-

tions between Type 1 and Type 2 objects, a classification based on the properties of an objects optical line spectra. Type 1 AGN are defined as sources which have optical spectra that show strong, broad, permitted emission lines. Type 2 AGN are defined as sources that have optical spectra that display only narrow, forbidden, emission lines and do not show significant broad line emission. Heavy obscuration was first suggested as the intrinsic cause of the differences between the Type 1 / Type 2 classification of AGN by Rowan-Robinson (1977) in a discussion on the emission line profiles observed in optical AGN spectra, when he suggested that “it is dust surrounding the optical core which attenuates the broad wings and causes the distinction between Type 1 and Type 2 spectra”. The possibility that this obscuration is orientation dependent is noted in the same work. Following this, many conclusions regarding the intrinsic properties of active galaxies were drawn from correlations between the X-ray emission and the optical narrow line and broad-line emission for a sample of 16 objects by Lawrence & Elvis (1982). Much of this analysis was based around the “standard Seyfert nucleus” picture, described for example in Weedman (1977) and Osterbrock (1978). At the time the standard Seyfert nucleus picture was devised, the only Seyferts that had been positively detected in X-rays were NGC 1275 (in fact, this may have been a mis-identification of the Perseus cluster), NGC 4151 (Gursky *et al.* 1971) and NGC 3783 (Cooke *et al.* 1976). Furthermore, virtually all of the conclusions regarding the properties of Seyfert 2 galaxies as a whole were based on the analysis of NGC 1068, which was assumed to be a good representative of Seyfert 2 galaxies as a class.

A major breakthrough came a few years later with the proposal of an AGN unification model by Antonucci (which became affectionately known as the Straw Person Model, hereafter SPM; Antonucci 1982, 1984). Initially focusing on radio galaxies, his work revealed that several prominent radio galaxies showed optical polarisation perpendicular to the radio structure axes and had a significantly less core-dominated radio morphology, in contrast with the other sources in the sample. In one object, 3C 234, the polarisation was very strong, $\sim 14\%$, a value similar to the polarised fraction observed for the well-known Seyfert 2 galaxy NGC 1068 ($\sim 16\%$), prompting the hypothesis that these two objects may well be analogous. The spectropolarimetry of NGC 1068 (Miller & Antonucci 1983) proved to be crucial to our understanding of AGN. The optical spectrum of NGC 1068 observed in polarised light revealed broad, permitted, line emission, that was not observed in the total flux spectrum (Figure 1.1)! Furthermore, the broad lines had equivalent widths identical to those seen in normal Seyfert 1 galaxies.

This strongly suggested that the observed polarisation in this source was the result of the scattering of the optical emission into our line-of-sight by dust grains or electrons in gas aligned with the radio structure axis of the galaxy. In addition, both NGC 1068 and 3C 234 displayed a photon budget problem, in that extrapolating the ultraviolet continuum emission into the optical band did not provide sufficient numbers of ionizing photons to account for the optical narrow line emission (Antonucci 1983, Wilson, Ward & Haniff 1988). This all built into a picture in which the continuum source was enclosed by a geometrically-thick ‘torus’ of material perpendicular to the axes of the radio structure (Figure 1.2). In this model, only photons escaping perpendicular to the torus are capable of being scattered into our line-of-sight. This situation results in us observing only a fraction of the continuum photons, but all of

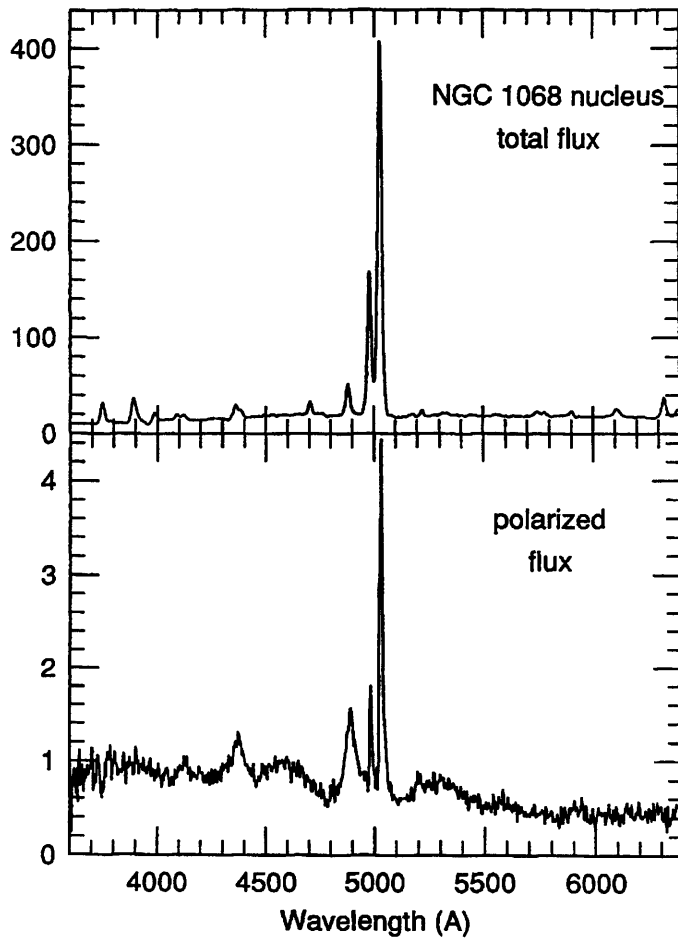


Figure 1.1: Spectropolarimetry of NGC 1068. *Top Panel:* The total optical flux spectrum from NGC 1068. The narrow line features and the lack of broad line features classify this as a Type 2 object. *Bottom Panel:* The polarised flux spectrum from NGC 1068. The obvious broad line features in this spectrum would classify this as a Type 1 object. (Miller, Goodrich & Mathews 1991)

the line photons (resolving the photon budget problem). The photons escaping in the polar direction will become highly polarised by the scattering process, resulting in a polarised Type 1 spectrum being scattered into our line-of-sight, in contrast to the Type 2 spectrum sampled by the direct line-of-sight to the central source. This was the first strong evidence for the “hidden Seyfert 1 nucleus” in the core of heavily obscured AGN.

Over the last two decades, the development of ever more powerful telescopes has resulted in the extensive study of Seyfert 2 galaxies across the electromagnetic spectrum. However since this thesis focuses on the X-ray spectra of heavily obscured AGN, the rest of this brief history will concentrate on describing the recent developments regarding heavily obscured AGN from an X-ray perspective. The first detections of Seyfert 2 galaxies in X-rays were reported by Kriss, Canizares & Ricker (1980) as part of a series of observations of 37 Seyferts with the *EINSTEIN* X-ray Observatory. Of the 14 Seyfert 2 galaxies

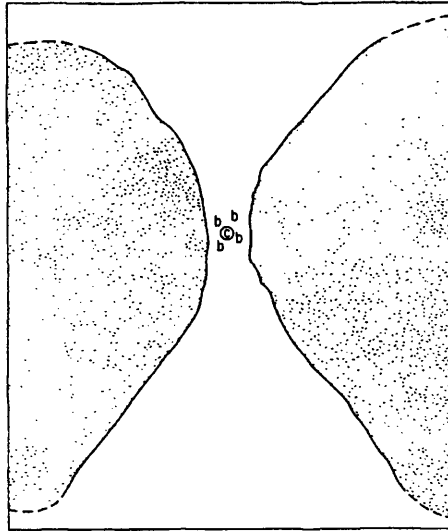


Figure 1.2: Diagrammatic representation of the central regions of an AGN, showing a continuum source (C) and broad-line clouds (b) surrounded by a geometrically and optically thick disk. This representation was first presented by Antonucci (1984) as a model for the observed properties of NGC 1068.

included in this sample, 4 were positively detected in the 0.5-4.5 keV band (Mrk 78, Mrk 348, Mrk 507 and NGC 4507). The *EINSTEIN* X-ray spectra from the Seyfert 2 galaxies were considerably steeper than the spectra from the Seyfert 1 objects but, given that a smooth transition in luminosity was observed between Seyfert 1's and Seyfert 2's, it was suggested that Seyferts 2 galaxies may simply be intrinsically less luminous examples of Seyfert 1 sources. As it turns out, this simplistic interpretation is incorrect, with Seyfert 2 galaxies showing a large range of intrinsic luminosities (*e.g.* $\sim 10^{40}$ - 10^{44} erg s $^{-1}$; Turner *et al.* 1997a) very comparable to the range of luminosities observed for Seyfert 1 galaxies. There is now growing evidence (*e.g.* Kinkhabwala *et al.* 2002) that the soft X-ray spectrum of Seyfert 2 galaxies is composed largely of photoionized emission lines from an extended Narrow Line Region (NLR); this point is discussed in more detail in Chapter 6.

By the late 1980's soft X-ray emission from Seyfert 2 galaxies was a well known phenomenon, but it wasn't until 1988 that the first clear hard X-ray detection of a Seyfert 2 galaxy, NGC 1068, was published (Elvis & Lawrence 1988). The X-ray spectrum from the first *EXOSAT* observation of NGC 1068 was extremely flat and showed a possible (though very weak) detection of fluorescent iron $K\alpha$ line emission (Figure 1.3). The lack of any observed variability in NGC 1068 and the extremely flat nature of the hard X-ray spectrum strongly suggested that the direct line-of-sight to the continuum in NGC 1068 is completely obscured (*e.g.* $N_H \sim 10^{25}$ cm $^{-2}$)! The nature and components of the X-ray spectrum, in conjunction with the spectropolarimetry results, all supported the unified picture of AGN proposed by Antonucci (1984).

As an aside here I note that the well known Seyfert 1 galaxy, NGC 4151, which occupies a large part of the work in this thesis, was one of the first Seyferts detected in X-rays and, in fact, Gursky *et al.*

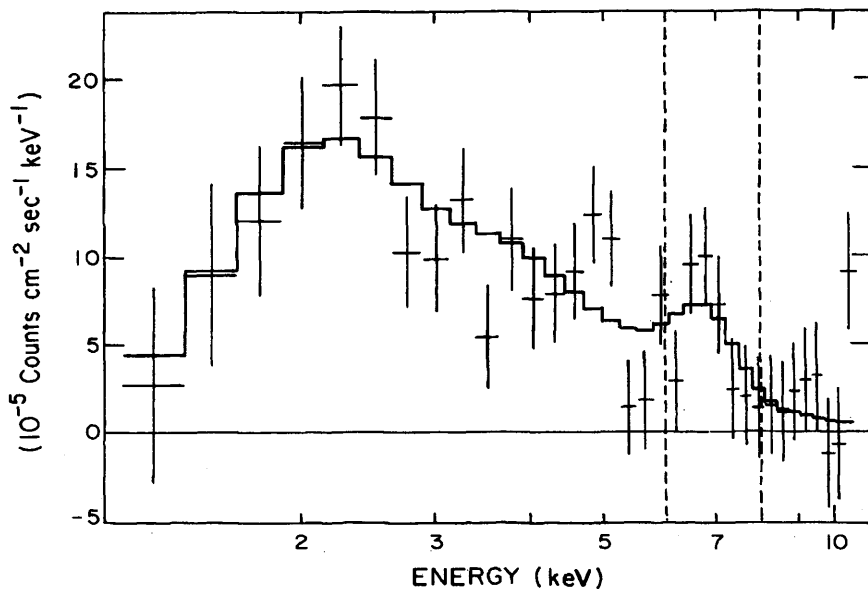


Figure 1.3: The unfolded X-ray spectrum from the first *EXOSAT* observation of NGC 1068. This was the first clear detection of hard X-ray emission from a Seyfert 2 galaxy. The best-fit to the data (shown here as a solid line) is a model incorporating a simple absorbed power-law continuum plus a single Gaussian line to represent the possibility of iron $K\alpha$ emission. (Elvis & Lawrence 1988)

(1971) detected X-ray emission from NGC 4151 up to ~ 7 keV despite it being classified optically as a Seyfert 1. More recent observations of NGC 4151 have unearthed considerably evidence for a large X-ray absorbing column comparable to those seen in Seyfert 2 galaxies. Detailed background information specific to NGC 4151 is presented at the beginning of Chapter 3 and will not be discussed further here.

Over the next few years, X-ray observations of bright Seyfert 2 galaxies (for example, Mrk 348; Warwick *et al.* 1989, NGC 4388 Hanson *et al.* 1990) with *Ginga* revealed hard X-ray spectra characterised by a power-law continuum with a photon index relatively typical of AGN in general (*i.e.* $\Gamma \sim 1.7$; Turner & Pounds 1989) and line-of-sight X-ray column densities somewhat smaller than that observed in NGC 1068 (*e.g.* $N_H \sim 10^{23} \text{ cm}^{-2}$ in the case of Mrk 348). The spectral index of the power-law continuum, the relatively high 0.5-10 keV luminosity ($\sim 1.1 \times 10^{43} \text{ erg s}^{-1}$ for Mrk 348, *c.f.* $\sim 3 \times 10^{41} \text{ erg s}^{-1}$ for NGC 1068) and the range of substantial, but not overwhelming, column densities were all consistent with a picture of Seyfert 2 galaxies in which the putative torus is geometrically-thick but not necessarily always Compton-thick. More spectral evidence for this picture came from Mrk 3. Observed with *Ginga* in 1989 (Awaki *et al.* 1990), the hard X-ray spectrum of Mrk 3 was flat ($\Gamma = 1.3 \pm 0.3$) with a strong iron $K\alpha$ emission line and the largest X-ray absorbing column density ever directly measured for a Seyfert galaxy at that time ($6_{-2}^{+3} \times 10^{23} \text{ cm}^{-2}$). Concurrent optical spectropolarimetric studies of Seyfert 2 galaxies revealed at least four additional examples of Seyfert 2's with hidden broad line regions, one of which was Mrk 3 (the others being Mrk 348, Mrk 463E and NGC 7674; Miller & Goodrich 1990). The consistency between the X-ray spectral properties and the broad lines found in polarised optical light

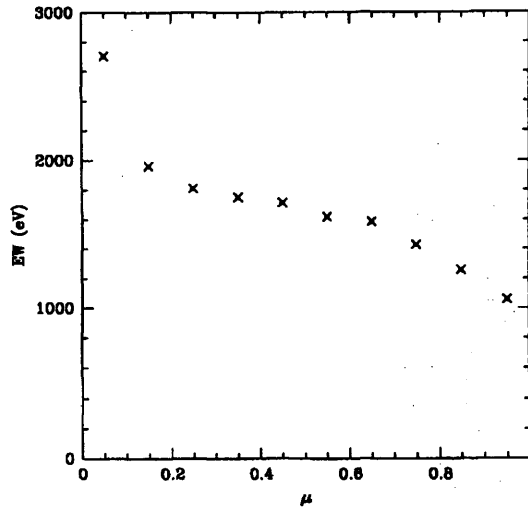


Figure 1.4: The equivalent width (EQW) of the neutral iron $K\alpha$ fluorescent line from a Compton-thick (*i.e.* $N_H > 1.5 \times 10^{24} \text{ cm}^{-2}$) torus as a function of the cosine of the inclination angle (μ). (Matt, Brandt & Fabian 1996)

dramatically strengthened the case for the hidden Type 1 nucleus in both Mrk 3 and Mrk 348.

The following few years saw an explosion in the number of Seyfert 2 galaxies detected in X-rays, largely from observations with the *Ginga* satellite (*e.g.* Hanson *et al.* 1990, Awaki *et al.* 1991a, Awaki *et al.* 1991b, Mulchaey, Mushotzky & Weaver 1992). The absorbing column densities in the observed Seyfert 2 galaxies ranged from 10^{22} - 10^{24} cm^{-2} and the presence of UV emission combined with the observed hard X-ray absorption argued strongly for a specific geometry for AGN which must have the general properties highlighted in the unified AGN model (Mulchaey, Mushotzky & Weaver 1992). Many of the X-ray spectra also displayed evidence for strong iron $K\alpha$ line emission, as predicted by the unified AGN picture. Optical spectropolarimetry continued to have considerable success in detecting broad line features in polarised light with the detection of Type 1 optical spectra in yet another 4 Seyfert 2 galaxies (Mrk 477, Mrk 1210, NGC 7212, and Was 49b; Tran, Miller & Kay 1992). By the mid-nineties more than 20 Seyfert galaxies had been detected in hard X-rays (Smith & Done 1996) and the spectra from these sources not only showed considerable evidence for the high absorbing column densities and an iron $K\alpha$ line, but also began to indicate the presence of a strong Compton reflection component that was initially associated with reflection off a cold accretion disk (George & Fabian 1991, Matt, Perola & Piro 1991, Ghisellini, Haardt & Matt 1994). This new component to the X-ray spectrum of heavily obscured Seyferts was invoked to explain both the extremely flat spectra of some of the sources and the presence of a strong iron $K\alpha$ line.

The neutral Compton reflection component was found to be significant in more than half of the 23 Seyfert 2 galaxies in the sample analysed by Smith & Done (1996). In each of the sources where the reflection component was found to be significant, strong iron $K\alpha$ line emission was also detected suggesting that at least some of the iron line flux may be associated with the neutral Compton reflection. It was also

recognised that a cold accretion disk is not the only region of an AGN capable of producing neutral Compton reflection (Ghisellini, Haardt & Matt 1994, Krolik, Madau & Życki 1994). According to Smith & Done (1996) “there is also a possibility of an additional reflection component from optically thick parts of the molecular torus”.

In sources where the observed Compton reflection component and the iron $K\alpha$ line are associated with reprocessing in the torus, the properties of these components, such as the iron $K\alpha$ line equivalent width (EQW), can provide diagnostics of the physical properties of the torus. Identifying the warm scattering gas in the AGN with the warm absorbers seen in Seyfert 1 galaxies implies a torus opening angle of between 55° - 70° (Ghisellini, Haardt & Matt 1994). The properties of the iron $K\alpha$ line emission associated with Compton reflection from the molecular torus were calculated by Matt, Brandt & Fabian (1996) and Krolik, Madau & Życki (1994) and it was shown that the expected EQW of the iron $K\alpha$ line in a “Compton-thick” (*i.e.* $N_H > 1.5 \times 10^{24} \text{ cm}^{-2}$) Seyfert 2 was typically greater than 1 keV (Figure 1.4). At this point the only Seyfert 2 with an observed EQW greater than 1 keV was NGC 1068 (Awaki *et al.* 1991a), further strengthening the interpretation of NGC 1068 as a Compton-thick source. The possibility of torus reflection as a strong contribution to the X-ray spectrum was initially rejected by the model fits to the *Ginga* spectra, but it is an idea that has since re-surfaced. Around this time it was also recognised that the nature of the absorbing column density in these objects will have a profound impact on the X-ray spectrum (Smith & Done 1996). Specifically, ionized absorbing material produces a low-energy cut-off that is considerably less sharp than the standard ‘cold’ absorption and this can produce an abnormally flat spectral form (this point is discussed in detail in Chapter 3).

In 1993 the Advanced Satellite for Cosmology and Astrophysics (*ASCA*) X-ray telescope was launched by Japan and almost immediately it began observing individual Seyfert galaxies. *ASCA* was the first X-ray astronomy mission to combine imaging capabilities with a broad (0.3-10.0 keV) pass band, good spectral resolution, and a large effective area. *ASCA* was also the first X-ray astronomy satellite to use CCD detectors. As part of a series of observations with *ASCA*, covering 25 Type 2 AGN, Turner *et al.* (1997b) identified 6 objects (NGC 1068, NGC 4945, NGC 2992, Mrk 3, Mrk 463 and Mrk 273) that they conclude are completely dominated by reprocessed X-rays (this conclusion was drawn from X-ray spectra, variability and [O III] line emission arguments). These extreme examples of the Type 2 class of AGN, with absorbing column densities $\gg 10^{24} \text{ cm}^{-2}$, showed considerable evidence for ionized emission below 3 keV, although in all but one case it was not possible to distinguish between re-emission from warm absorbing material or thermal emission from a nuclear starburst. The one exception to this was Mrk 3 which did not show significant starburst contamination and in this case Turner *et al.* (1997b) concluded that the spectrum below 3 keV was dominated by emission from gas that is *more* highly ionized than the warm absorbing gas typically observed in Seyfert 1 galaxies. This conclusion regarding the nature of the soft excess was a significant advance over the previous hypothesis, namely that the soft X-ray emission in Type 2 AGN was generated entirely by scattering of the direct continuum emission into our line-of-sight. Although *ASCA* spectra were not of sufficient quality to clearly resolve individual features in the soft X-ray spectrum, Griffiths *et al.* 1998 tentatively suggested that a broad feature at 0.9 keV

in the soft X-ray spectrum of Mrk 3, which they interpreted as O VIII recombination, is indicative of a photoionized medium rather than thermal emission from hot gas. The remaining sources in the sample of heavily obscured Seyferts used in Turner *et al.* (1997a) showed a remarkable variety of spectral forms and variability properties, although the mean spectral index of the underlying hard X-ray continuum from this study ($\Gamma \sim 2$) is remarkably similar to that found for Seyfert 1 galaxies around the same time (Nandra & Pounds 1994), supporting the AGN unification schemes. In an even larger study, a sample of 45 heavily obscured Seyfert galaxies (Risaliti, Maiolino & Salvati 1999) found that 75% of the Seyfert 2 galaxies in the sample were very heavily absorbed ($N_H > 10^{23} \text{ cm}^{-2}$), and that around 50% of them were Compton-thick sources ($N_H > 10^{24} \text{ cm}^{-2}$). In contrast, the X-ray spectra from the sources classified as Seyfert 1.8 and 1.9 galaxies were best modelled with a considerably smaller average absorbing column. The large fraction of Compton-thick objects strongly implies that the majority of the obscuring material in heavily obscured Seyferts is located within a radius of a few tens of parsecs from the nuclear continuum source, consistent with the AGN unification schemes.

One of the most significant scientific results to come out of the *ASCA* mission was the detection of iron $K\alpha$ line emission in AGN spectra with a skewed line profile suggesting that the line was being relativistically broadened and hence must originate in material very close (within a few Schwarzschild radii) to the supermassive black hole core of the AGN (Figure 1.5). The first clear example of a broad, skewed, iron $K\alpha$ line profile in the X-ray spectrum of an AGN came from a long *ASCA* observation of the famous Seyfert 1, MGC-6-30-15 (Tanaka *et al.* 1995; Figure 1.6). Following this discovery, Nandra *et al.* (1997) and Reynolds (1997) studied more than 20 Seyfert 1 galaxies and found that the iron line profiles in most of these sources were significantly broader than the spectral response of *ASCA*. In a similar vein, Turner *et al.* (1998) studied the iron $K\alpha$ line profiles observed in the *ASCA* spectra of a sample of 25 Type 2 AGN and found that the majority of the sources showed line profiles indicative of the reprocessing of nuclear X-rays in a face-on accretion disk, very similar to the line profiles observed in the Seyfert 1 galaxies. The inferred face-on orientation of the accretion disks in these sources from is not in good agreement with the predictions of the unified AGN models, which predict that the inner regions of Seyfert 2 galaxies are viewed edge on.

The generic view of Seyfert 2 galaxies resulting from the numerous *ASCA* observations was one of a complex set of sources displaying a large range of luminosities, a large range of absorbing columns, significant Compton reflection emission, complex soft X-ray emission components associated with either a nuclear starburst or with a warm absorber intrinsic to the AGN and, finally, a fluorescent iron $K\alpha$ line with a complex, relativistically broadened line profile. Despite this picture there is a strong body of evidence which indicates that the hard X-ray properties of Type 2 AGN depends largely (if not solely) on a single parameter, the absorbing column density along the line of sight (Bassani *et al.* 1999), in accordance with the unified model.

Some of the complexities of this picture were addressed with observations by the *BeppoSAX* X-ray satellite, launched in 1996 by the Italian Space Agency. With its combination of wide bandpass (0.1-

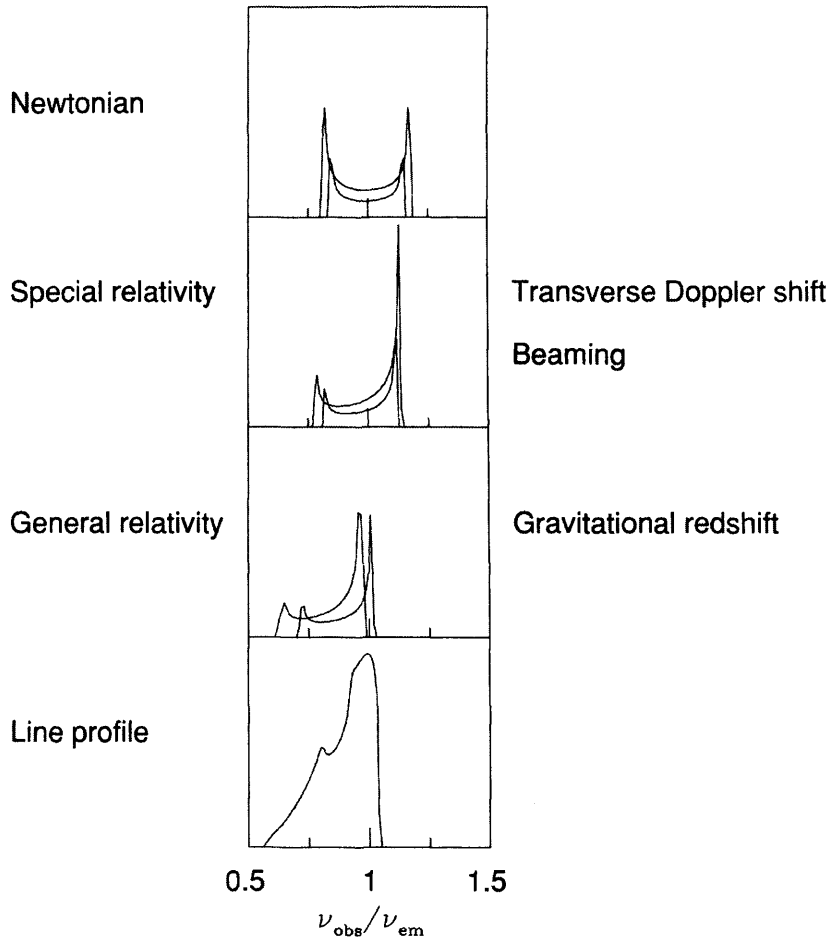


Figure 1.5: The emission and physical processes that combine to make the relativistically broadened iron $K\alpha$ line profile observed in Seyfert galaxies. *Top Panel:* Symmetric double-peaked profiles from two narrow annuli on a non-relativistic disk. *Upper-middle Panel:* Adding the effect of relativistic beaming and transverse Doppler-shifts to the two line profiles shown in the Top Panel. *Lower-middle Panel:* Adding the effects of gravitational redshift to the total line profiles. *Bottom Panel:* The total line profile integrated over a range of annuli and including all of the above effects. (Fabian *et al.* 2000)

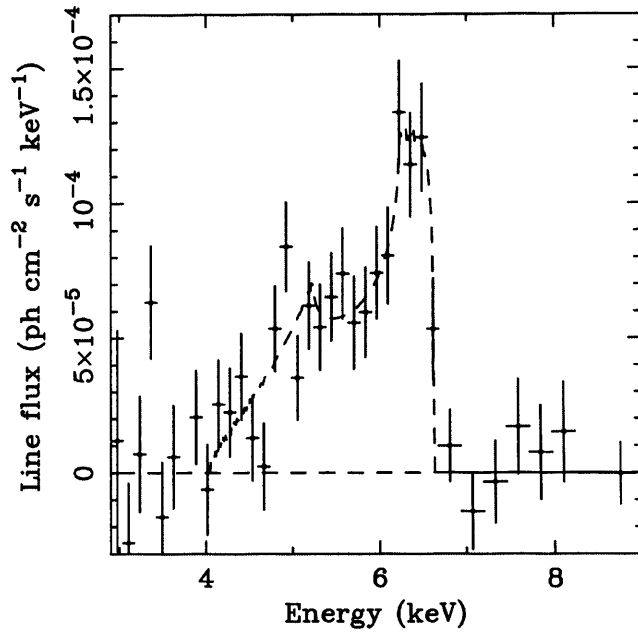


Figure 1.6: The iron $K\alpha$ line profile observed by *ASCA* in MGC-6-30-15 (Tanaka *et al.* 1995). Only the SIS data are shown here for simplicity. The dotted line shows the best-fit line profile from an externally illuminated accretion disk around a Schwarzschild black-hole (Fabian *et al.* 1989).

300 keV) and good spectral resolution, *BeppoSAX* observed 20 Compton-thin Seyfert 2 galaxies and 7 Compton-thick Seyfert 2 galaxies. The observations of the Compton-thin sources (Risaliti 2002) confirm the ubiquitous presence of a Compton reflection component in the X-ray spectra of the observed Seyfert 2 galaxies. The large bandpass of *BeppoSAX* was particularly important in providing the tightest possible constraints on the properties of the Compton reflection components observed in these sources because the Compton reflection continuum peaks at ~ 30 keV (Section 2.4.3), well outside the bandpass of many other X-ray astronomy satellites. All the low column density sources showed strong iron $K\alpha$ line emission, with EQW's between 100-300 eV, the majority of which did *not* show the broadened line profile described previously. These results are in good agreement with the unified AGN schemes, implying that the problematic broad iron $K\alpha$ line profiles found in the *ASCA* data may be artefacts of the spectral modelling of the *ASCA* data (this is discussed in detail in Chapter 3). The Compton-thick sources observed with *BeppoSAX* (Matt *et al.* 2000) follow in this mould, showing ubiquitous Compton reflection and strong iron $K\alpha$ line emission. In several of the sources there were indications that the Compton reflection component may originate in ionized material, however the data were not of sufficient quality to tightly constrain the properties of the ionized reflector. The two brightest Compton-thick AGN observed with *BeppoSAX* (NGC 4945 and Circinus) also showed marginal evidence of a mild (*i.e.* less than a factor of two) overabundance of iron relative to solar iron abundance.

The advent of the *XMM-Newton* and *Chandra* X-ray satellites is beginning revolutionise our understanding of heavily obscured AGN. Chapter 2 gives a brief description of the details of the *XMM-Newton* satel-

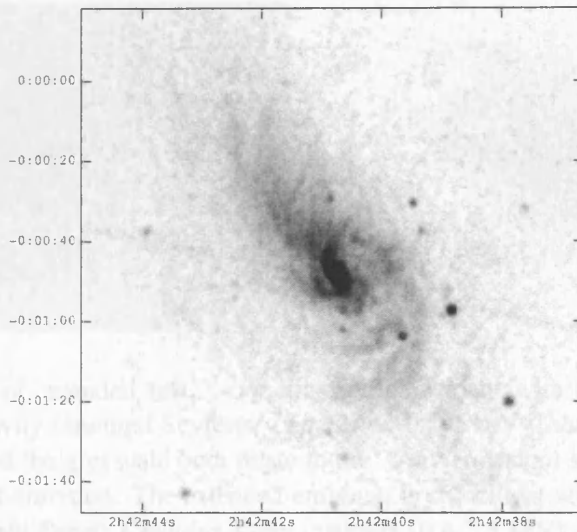


Figure 1.7: Grayscale *Chandra* image of NGC 1068. The image has been smoothed with a $0.5''$ Gaussian kernel. The linear feature running across the nucleus is an instrumental effect. (Young, Wilson & Shopbell 2001)

lite and its instruments, however for a complete description of *XMM-Newton*, *Chandra* and their relative capabilities, see Jansen *et al.* 2001 and Weisskopf *et al.* 2002 (and references therein), respectively. The extremely high spatial resolution of *Chandra* is yielding an unparalleled view of the X-ray emission from the nuclear regions of galaxies, helping to resolve source confusion issues and often revealing considerable extended X-ray emission. A recent *Chandra* observation of the archetypal Seyfert 2, NGC 1068, has revealed an incredibly detailed and complex X-ray morphology in this nearby source, including the bright, compact AGN core and considerable extended emission (Figure 1.7). The extended emission is tightly correlated with the [O III]($\lambda 5007$) emission, detected by the *Hubble Space Telescope* (HST), and clearly traces the spiral arms and other structures out to a considerable distance from the nucleus of the galaxy. The nuclear soft X-ray emission is extended in the same direction as the optical line emission and the radio emission, coinciding with the optical narrow line ionization cone in NGC 1068. There is considerable evidence that extended soft X-ray emission associated with the optical narrow line ionization cones is a common feature in AGN, particularly in heavily obscured AGN. Extended soft X-ray emission associated with the optical narrow line ionization cones is also detected in Mrk 3, although with poorer spatial resolution due to the distance of Mrk 3 (Sako *et al.* 2000; Figure 1.8: Left Panel), and in NGC 4151 (Ogle *et al.* 2000; Figure 1.8: Right Panel). The properties of this emission are discussed in more detail in chapter 6 of this work.

At the time of writing, the *XMM-Newton* EPIC CCD spectra of only 3 heavily obscured AGN galaxies have been published outside of this work (NGC 4138; Foschini *et al.* 2002, NGC 4258; Pietsch & Read 2002 and UGC 4203; Guainazzi *et al.* 2002) and hence the work presented in this thesis represents not only the first publication of these recent observations of individual heavily obscured sources, but it also represents a large fraction of the *XMM-Newton* observations of heavily obscured AGN pub-

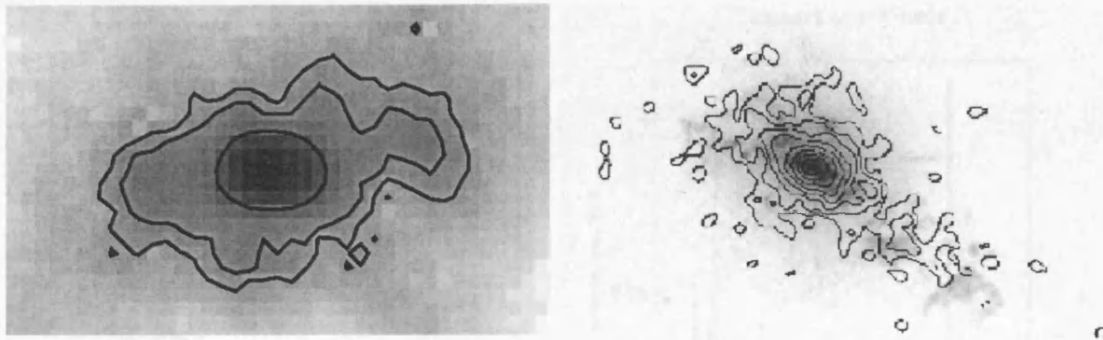


Figure 1.8: Examples of extended soft X-ray emission coincident with the optical narrow line ionization cones in heavily obscured Seyferts. *Left Panel:* 0.5-4 keV *Chandra* ASIS-S image of Mrk 3 (the contours and the greyscale both relate to the X-ray emission) showing the unresolved core and faint extended emission. The extended emission is coincident with the [O III] emission (Sako *et al.* 2000). *Right Panel:* *Chandra* X-ray contours (0.4-2.5 keV) overlaid on an HST [O III] image of NGC 4151, clearly demonstrating the co-spatial nature of the soft X-ray and optical line emission gas. (Ogle *et al.* 2000)

lished so far. In addition to the high spatial resolution afforded by *Chandra*, the large collecting area of *XMM-Newton* and the high resolution X-ray spectroscopy capabilities (in the form of X-ray grating and CCD instruments) of both missions across the whole 0.1-12 keV band is beginning reveal many new details of the X-ray emission from heavily obscured AGN, a prime example of which is the Circinus galaxy, a well known Seyfert 2. A recent *Chandra* grating observation has confirmed that the hard X-ray spectrum of this source is dominated by Compton reflection with a strong iron line emission (Figure 1.9) and has reinforced many of the conclusions drawn from previous observations of this source with *ASCA* and *BeppoSAX*. On the other hand, the nature of the soft X-ray emission was revealed to be remarkably different to that inferred from the previous observations of Circinus. The soft X-ray spectrum from the *Chandra* High-Energy Transmission Grating (HETG) is dominated by X-ray emission lines, the measured properties of which currently provide the tightest constraints yet on the detailed nature of the soft X-ray emission in this source (Sambruna *et al.* 2001). A *Chandra* observation of Mrk 3 revealed a very similar picture, namely that the soft X-ray spectrum is composed of a multitude of X-ray emission lines (Sako *et al.* 2000). Recent observations of NGC 1068 with the Reflection Grating Spectrometers (RGS) on *XMM-Newton* have provided the highest signal-to-noise, high-resolution, soft X-ray spectrum of a Seyfert 2 galaxy so far, giving us a uniquely detailed view of the origin and properties of the ionized emitting gas in this source (Kinkhabwala *et al.* 2002). This observation is discussed in detail and compared to the RGS spectrum of NGC 4151 in chapter 6.

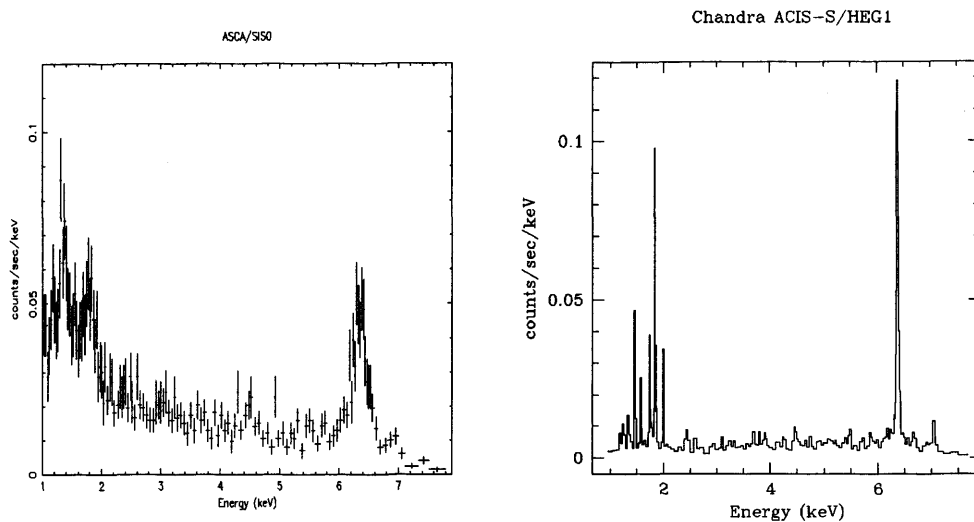


Figure 1.9: A comparison of CCD and grating X-ray spectra. *Left Panel:* ASCA SIS CCD spectrum of the Circinus galaxy (Matt, Brandt & Fabian 1996). *Right Panel:* Chandra High-Energy Transmission Grating (HETG) spectrum of the Circinus galaxy (Sambruna *et al.* 2001)

1.3 The current AGN unification picture

The X-ray spectra of the heavily obscured AGN presented in this thesis have been analysed from the point of view of the unified picture of the AGN nucleus. As such it is important that the reader has a clear understanding of the current unified AGN picture. The latest incarnation of AGN unification is best (and most often) described by a modified version of the cartoon figure presented in Urry & Padovani (1995) for radio loud objects (Figure 1.10). In this picture the various observed empirical ‘types’ of AGN are reproduced by a product of the orientation of the nucleus with respect to our line-of-sight and whether the source is radio-loud or radio-quiet (all the sources presented in this thesis are radio-quiet). The radio-quiet picture is composed of the following components:

1. A central black hole with a mass in the region of 10^6 - $10^9 M_{\odot}$ (see Rees 1984 and references therein for a review of the black hole models for AGN).
2. A hot accretion disk ($\sim 10^6$ K). Matter pulled towards the black hole loses angular momentum through viscous or turbulent interactions forming a disk-like structure around the central black hole. The loss of gravitational potential energy by the in-falling material in this disk as it is pulled onto the central black hole powers the output of the whole AGN system at all wavelengths, from gamma-rays to radio synchrotron emission. The exception to this is if the black hole has appreciable spin, in which case it is possible to extract energy electromagnetically from the black hole itself (Wilms *et al.* 2001).
3. A corona of hot electrons surrounding the accretion disk. It is this hot corona of electrons that is

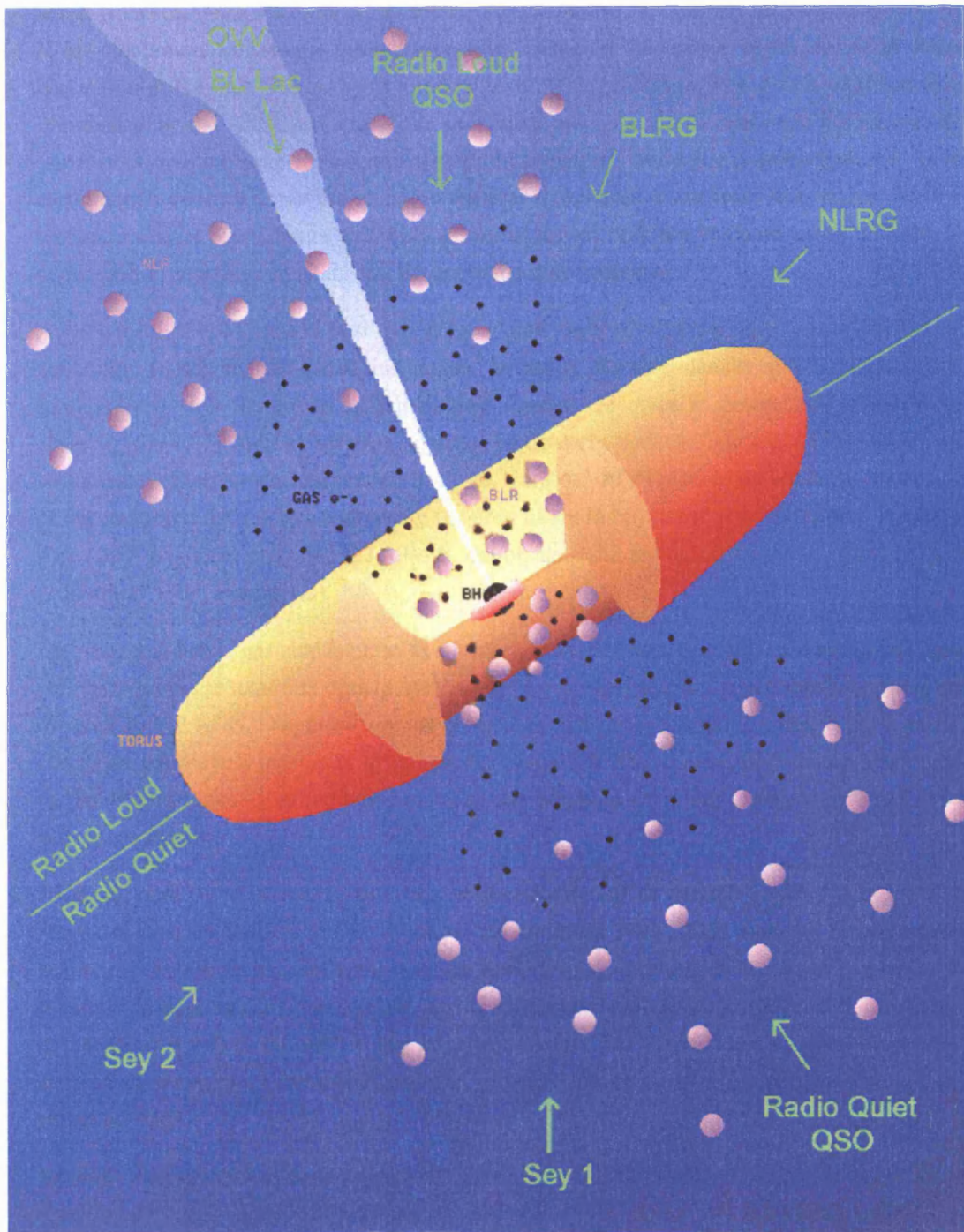


Figure 1.10: A schematic (not to scale) of the current paradigm for the unification of the various types AGN (Urry & Padovani 1995)

thought to be responsible for the high-energy AGN continuum emission, produced by the thermal Comptonization of soft seed photons from the accretion disk (Section 2.4.3; Zdziarski, Poutanen & Johnson 2000; Petrucci *et al.* 2000). An alternative mechanism for the production of the X-ray continuum emission is through magnetic flaring on the surface of the accretion disk (*e.g.* Nayakshin & Kazanas 2001). Such a model predicts that small regions of the accretion disk are illuminated by the X-ray emission from individual magnetic flares, and each flaring region will travel in co-rotation with the accretion disk. In principle, future X-ray telescopes will have the capability to detect the moving emission features that would result from this model. Such a detection, amongst other things, will be a powerful test of both the mechanism by which the X-ray continuum is generated in AGN and the accretion disk geometry.

4. A thick torus of cold gas and dust that, from a large range of viewing angles, obscures the central continuum source and the broad-line region. In reality, the size, density and homogeneity of the torus is likely to be unique to each individual source. However, in general the properties of the absorber should be similar between sources, particularly between sources with similar intrinsic luminosities. Despite the implication from the ‘cartoon’ AGN picture shown here, the outer edge of the obscuring torus is not necessarily (or even likely to be) sharp or well defined. In fact, when Antonucci originally proposed the SPM he deliberately did not define the outer limits of the torus (Antonucci 1984; Figure 1.2).
5. Fast moving, dense, gas clouds close to the black hole. These clouds produce the broad lines that are observed in the total flux optical spectra of Type 1 AGN and the polarized flux optical spectra of some Type 2 AGN. Diagnostics of the properties (size, bulk motion etc) the Broad-Line Region (BLR) are particularly important given that the optical classification of AGN results almost entirely on the relative visibility of the broad features that originate from this region (Antonucci 1984 and references therein).
6. Uniform, optically-thin, warm scattering region composed of ionized gas and dust that extends from the inner regions of the BLR out to the extended NLR. This material is responsible for scattering the optical line emission into our line-of-sight, resulting in the Type 1 observed in the polarized optical flux of Type 2 AGN, and is also responsible for any scattered X-ray continuum emission observed in the soft X-ray spectra of AGN. The ionized gas in this component also contributes strongly to the soft X-ray line emission observed in a growing number of heavily obscured AGN.
7. Slow moving gas clouds further out from the black hole. These clouds, with the warm scattering medium, form the extended NLR and are responsible for the narrow lines observed in the total flux optical spectra of Type 2 AGN, and also contributes to the soft X-ray line emission observed in a growing number of heavily obscured AGN. This region is extended on scales of hundreds of parsecs.

To get an idea of the scales involved in this picture, the Schwarzschild radius of a $10^8 M_{\odot}$ black hole is $\sim 3 \times 10^{13}$ cm and the accretion disk emits in a region between $\sim 1-30 \times 10^{14}$ cm from the centre of the system. The broad line clouds are located at a distance of around $\sim 2 \times 10^{16}$ cm and the inner radius of the torus is located between $10^{17}-10^{18}$ cm. On the largest scales, the NLR can extend out to approximately $10^{18}-10^{20}$ cm (Urry & Padovani 1995). Typical 2-10 keV X-ray luminosities for radio-quiet AGN range from $\sim 5 \times 10^{39}-10^{46}$ erg s $^{-1}$ (e.g. NGC 7743; Terashima, Ho & Ptak 2000 and PDS 456; Reeves *et al.* 2000). Radio-loud AGN can be up to 100 times brighter still, but it is likely that this is a direct result of the X-ray emission in these cases being relativistically beamed.

1.4 The aims of this thesis

The work presented in this thesis primarily concerns the hard X-ray spectroscopy of four, nearby, bright, heavily obscured Seyfert galaxies. This analysis has two main aims:

1. To emphasize the extremely complex nature of the X-ray absorption observed in heavily obscured AGN and to stress the massive impact that this absorption has on the observed properties of the X-ray variability and the X-ray spectrum.
2. To highlight the role of continuum reprocessing in the observed X-ray spectra of AGN, specifically underlining the strong impact that even mild levels of Compton reflection can have on conclusions drawn from the X-ray spectra of AGN and demonstrating the ubiquitous nature of emission and absorption features arising from transitions in iron atoms and ions.

The AGN studied here have a range of absorbing column densities (from 10^{23} cm $^{-2}$ to $>10^{24}$ cm $^{-2}$) and are presented in order of increasing absorption. All of the sources show strong evidence for Compton reflection and features arising from continuum reprocessing by iron. The work focuses largely on the analysis of recent data from the *XMM-Newton* X-ray satellite. Chapter 2 discusses some of the capabilities of this amazing observatory, particularly in the context of earlier X-ray observatories. Chapter 2 also briefly discusses some of the basic physical processes required to produce the X-ray spectrum of heavily obscured AGN. Chapter 3 begins the discussion of the individual sources, presenting a detailed analysis of the hard X-ray spectrum of the well-known Seyfert 1.5 galaxy, NGC 4151, from 3 separate X-ray satellites. In Chapter 4 the analysis of the hard X-ray *XMM-Newton* spectra of two sources, NGC 7582 and Markarian 3, which exhibit significantly heavier X-ray absorption than NGC 4151, are used to emphasize the effects of increasing absorption on the X-ray spectra of heavily obscured AGN. Chapter 5 is devoted to the analysis of the *XMM-Newton* EPIC hard X-ray spectrum of the Compton-thick AGN in NGC 4945, where the apparently simple extrapolation from the heavily obscured sources in the previous chapter is complicated by the introduction of a powerful nuclear starburst that strongly influences the appearance of this source. The final observational chapter, chapter 6, shifts the focus of the analysis to the

soft X-rays and describes the preliminary analysis and modelling of the extremely high-resolution, high signal-to-noise, reflection grating spectrum of NGC 4151. The final chapter presents the most significant conclusions from the work presented in this thesis and identifies some of the important questions which future work on heavily obscured AGN may help to answer.

Chapter 2

Instrumentation and Physical Processes

2.1 Overview: The capabilities of *XMM-Newton* and physical processes in AGN

Launched in 1999, the *XMM-Newton* X-ray observatory, with its three high-throughput X-ray telescopes and a 30 cm optical/UV telescope, represents a significant step forward for many types of astrophysical investigation. *XMM-Newton* is targeted towards X-ray spectroscopy and its features are particularly well-suited to the spectral study of AGN. Particular features that result in *XMM-Newton*'s unprecedented capability for astrophysical X-ray spectroscopy are a large collecting area, good spatial resolution imaging and medium-to-high spectral resolution spectroscopy across a wide energy range (0.1-15 keV). Observations with *XMM-Newton* are producing the best X-ray spectra of heavily obscured AGN yet taken and much of the analysis presented in this thesis is based on observations with the *XMM-Newton* X-ray observatory.

Section 2.2 presents a description of the *XMM-Newton* observatory and gives a brief summary of the capabilities of each of the major X-ray instruments. The comparison of the strengths and weaknesses of *XMM-Newton* with those of other X-ray observatories is discussed in Section 2.3. This section also briefly highlights the current state of the cross-satellite calibration between *XMM-Newton* and other X-ray satellites.

Finally, Section 2.4 gives a brief description of some of the physical processes that are responsible for the observed X-ray spectrum of AGN in general. Much of this will be familiar to readers with a background in astrophysics and the intention of the discussion presented here is to bring these physical processes to the forefront of the readers mind, rather than on providing a complete theoretical description of the mechanisms involved.

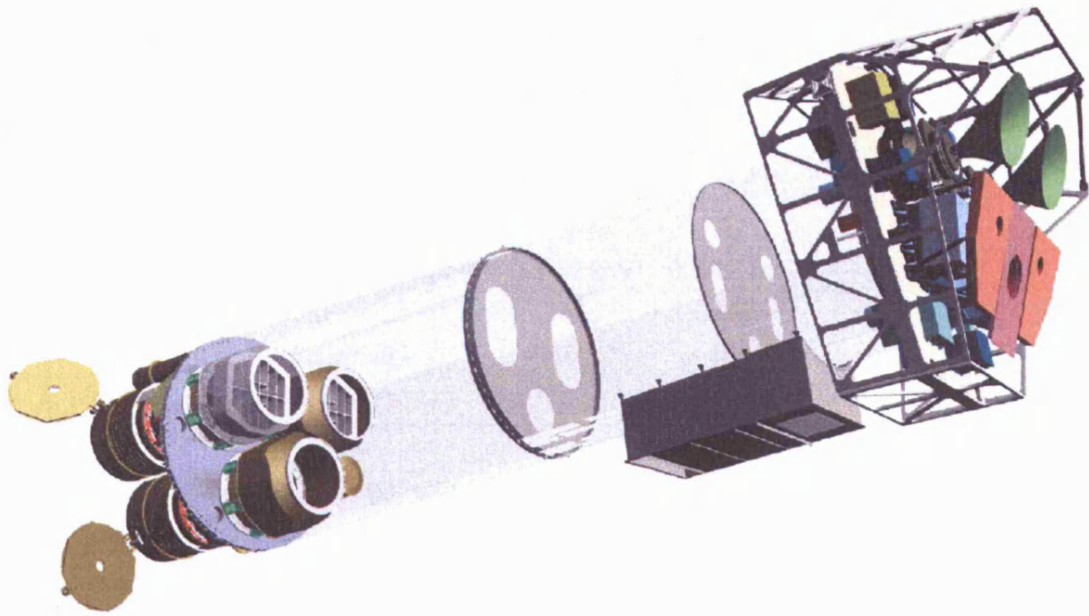


Figure 2.1: The *XMM-Newton* X-ray observatory. The mirror modules, two of which are equipped with reflection grating arrays, are visible to the left. The focal plane instruments are shown on the right, the EPIC MOS cameras with their radiators (black/green “horns”), the EPIC PN radiator (purple) and the RGS detector assembly (light blue and orange). The OM telescope is not shown here. (Dahlem 2002)

2.2 The *XMM-Newton* X-ray observatory

The *XMM-Newton* observatory is the second of four “cornerstone” European Space Agency missions defined in the Horizon 2000 Programme. The satellite carries three Wolter type-1 X-ray telescopes with a combination of high angular resolution CCDs (EPIC) and high spectral resolution reflection grating spectrometer (RGS) instruments at their foci. The observatory also has a 30 cm optical/UV telescope with a micro-channel plate CCD detector in its focal plane. Figure 2.1 shows the layout of the instruments and the mirror modules on the satellite. The technical information presented in the beginning of this section relies heavily on information from the *XMM-Newton* Science Operations Website[†], with particular reference to the *XMM-Newton* Users Handbook[‡] (Dahlem 2002).

The Wolter type-1 X-ray telescopes on *XMM-Newton*, each made of 58 nested mirror shells, are the largest effective area, focusing, X-ray telescopes yet flown, with a total effective area (at 1.5 keV) of 4650 cm². The mirrors achieve a point-spread function (PSF) with a full width at half maximum (FWHM) $\sim 6''$ and a half-energy width (HEW; the width at which 50% of the total energy from the observed source is encircled by the PSF) of $\sim 15''$. Two of the X-ray telescopes are equipped with a combination of an EPIC MOS CCD detector and an RGS instrument. The RGS grating assembly (RGA) intercepts

[†]<http://xmm.vilspa.esa.es/>

[‡]http://xmm.vilspa.esa.es/external/xmm_user_support/documentation/uhb/XMM_UHB.html

Table 2.1: The basic characteristics of the EPIC MOS and PN detectors.

	EPIC MOS	EPIC PN
CCD size	600x600	400x384
pixel size	1.1"x1.1"	4.1"x4.1"
Field of view	30'	30'
Usable bandpass	0.3-10 keV	0.3-12 keV
PSF	6"	6.6"
Sensitivity	$\sim 10^{-14}$	$\sim 10^{-14}$
	(erg s ⁻¹ cm ⁻²)	

$\sim 45\%$ of the radiation focused by the Wolter mirrors and disperses this onto a linear strip of CCDs. The third X-ray telescope does not have an RGS instrument associated with it and consequently the back illuminated EPIC PN CCD detector at the prime focus receives $\sim 90\%$ more flux than either of the two EPIC MOS detectors. If not prohibited by external factors (*e.g.* target brightness constraints) all six *XMM-Newton* science instruments (EPIC MOS 1 and 2, EPIC PN, RGS 1 and 2 and the OM) are operated simultaneously. *XMM-Newton* has been placed in a highly elliptical orbit which results in continuous target visibility of up to 40 hours, a major advantage for studies of source variability.

2.2.1 Details of the EPIC MOS and PN cameras

Figure 2.2 shows the layout for the EPIC MOS and EPIC PN X-ray CCD detectors on *XMM-Newton* operated both in full window (FW) and small window (SW) mode. Table 2.1 details the basic characteristics of the EPIC MOS and PN detectors.

The EPIC MOS detectors consist of 7 identical, front-illuminated CCD chips. The individual CCDs are offset with respect to each other, closely following the curvature of the focal surface of the Wolter telescopes. The two MOS detectors are rotated by 90° relative to each other to minimise the data loss from any single observation. The EPIC PN detector consists of 12 CCD chips on a single wafer substrate and consequently the PN CCDs are not vertically offset from each other. The PSF of the X-ray telescopes is well sampled by the MOS CCDs, a result of the small pixel size in comparison to the mirror PSF, however this is not the case for the PN detector where the CCD pixel size is directly comparable to the PSF of the X-ray mirrors. The poor PSF sampling of the PN CCDs is compensated for by the increased X-ray flux incident on the PN instrument and as a result of the increased statistical quality of the EPIC PN data, the absolute spatial position capabilities of the two types of EPIC detector are, in practice, very similar (S. Sembay. *Priv. Comm*). The spectral resolution of the EPIC detectors, as a function of photon energy is shown in Figure 2.3. Good spectral resolution is required at energies where prominent line emission is expected in the X-ray spectra of astronomical sources. Of particular importance in the X-ray

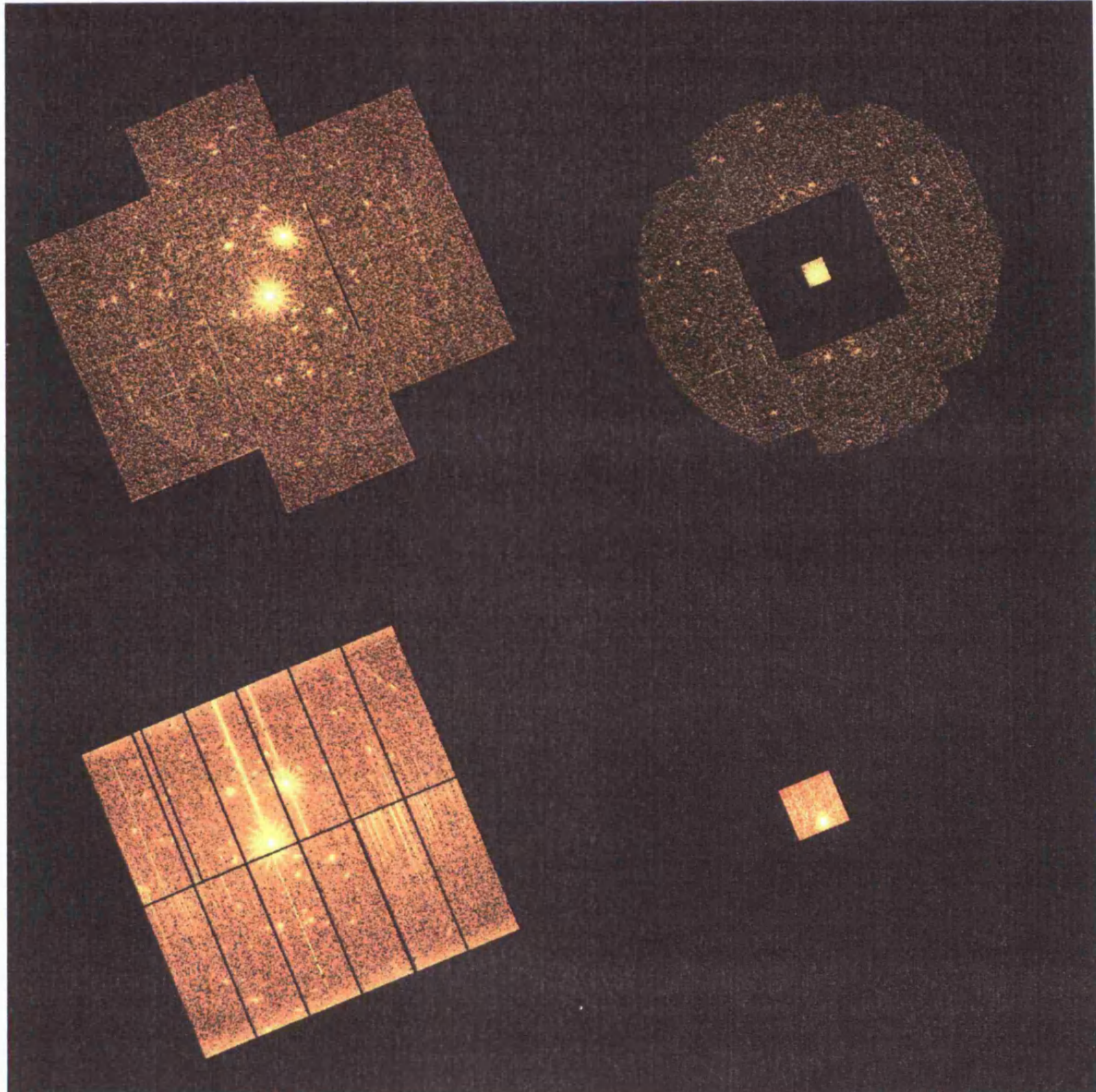


Figure 2.2: The layout of the EPIC Detectors in full window (FW) and small window (SW) mode. The images used in this example show the Seyfert nucleus of NGC 4151 at the prime focus of the EPIC detectors (see chapter 3), the BL Lac, MS 1207.9+3945, located $\sim 5'$ to the north of NGC 4151, and many point sources associated with the galactic disk of NGC 4151. *Upper-Left*: MOS 1, FW mode. *Upper-Right*: MOS 1, SW mode. *Lower-Left*: PN, FW mode. *Lower-Right*: PN, SW mode. A readout stripe is associated with each bright source in the PN FW mode image. The bright chip edges near the outside edge of the detector, and the fainter streaks that are *not* associated with specific sources, are low energy noise features and can be removed by energy filtering the data.

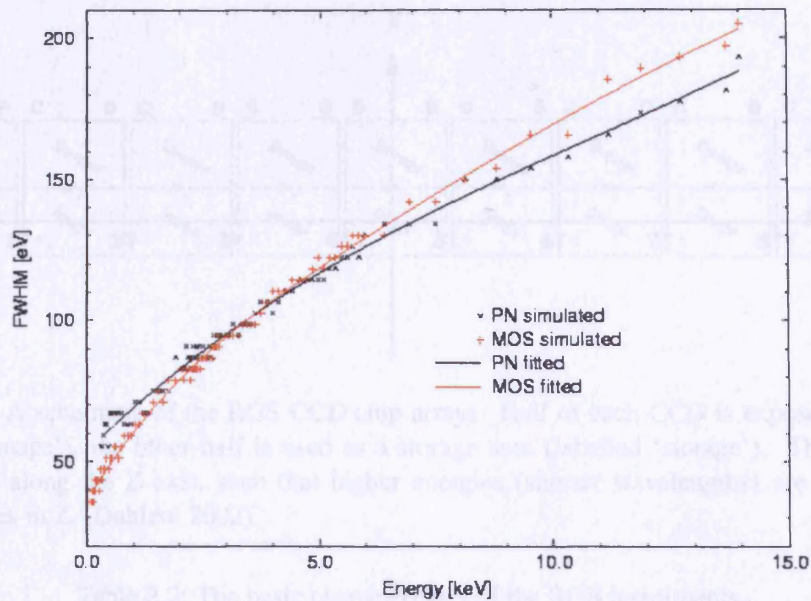


Figure 2.3: The EPIC MOS and PN energy resolution (FWHM) as a function of energy.†

study of AGN is the region around the iron $K\alpha$ line (~ 6.4 keV) where both types of EPIC detectors have good spectral resolution (~ 130 eV).

2.2.2 Details of the RGS instruments

Figure 2.4 shows the layout for the RGS CCD chips. Table 2.2 details the basic characteristics of the RGS instruments.

The RGS instruments associated with two of the X-ray telescopes on *XMM-Newton* each consist of a reflection grating assembly (RGA) and an RGS focal camera (RFC). The RGS instruments are designed for high spectral resolution X-ray spectroscopy and in order to maximize the science impact of the instrument, the energy range covered by the RGS was chosen to encompass a region that exhibits a particularly high density of X-ray emission lines, including the L shell transitions of heavy elements like Fe and Ni and K shell transitions of lighter elements, such as N, O, Ne, Mg, and Si. The RFC consists of a linear array of 9, back-illuminated, MOS CCDs, located along the dispersion direction of the RGA. Each CCD has 1024×768 pixels, half of which is exposed to the sky, while the other half is used as a data storage area. The field of view in the cross-dispersion direction is determined by the width of the exposed regions of the CCDs ($5'$), in the dispersion direction the aperture of RGS covers the entire FOV of the *XMM-Newton* mirrors however the response of the RGS decreases significantly for off-axis sources. There have been technical problems with two of the RGS CCDs (CCD 4 in RGS 2 and CCD 7 in RGS 1), which has resulted in these CCDs having less than half their original effective area. This

†http://www.xmm.ac.uk/onlines/uhb/xmm_uhb.html

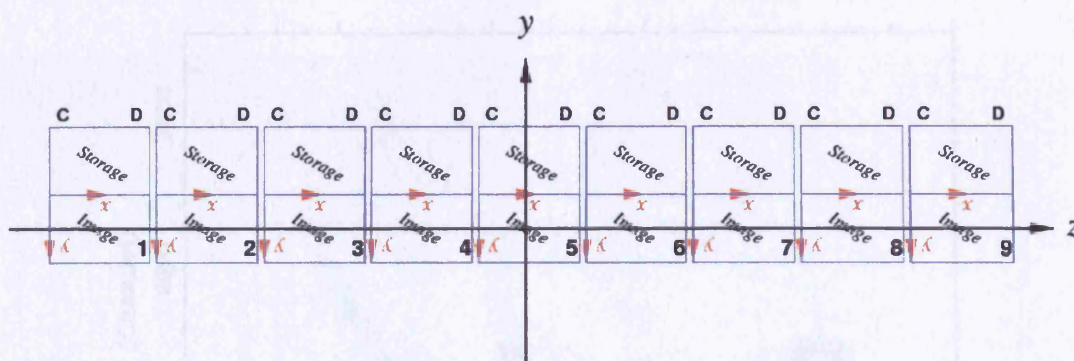


Figure 2.4: A schematic of the RGS CCD chip arrays. Half of each CCD is exposed to the sky (labelled ‘image’), the other half is used as a storage area (labelled ‘storage’). The dispersion direction is along the Z axis, such that higher energies (shorter wavelengths) are dispersed to higher values in Z. (Dahlem 2002)

Table 2.2: The basic characteristics of the RGS instruments.

RGS	
CCD size	1024x348
pixel size	2.5''x2.5'' ^a
Field of view	5'
Usable bandpass	0.35-2.5 keV
Sensitivity ^b	~8×10 ⁻⁵
Resolution	100-800 λ/Δλ

^a2.5'' corresponds to $9 \times 10^{-3} \text{ \AA}$ in the dispersion direction

^bO VII (0.57 keV) line flux in photons $\text{cm}^{-2} \text{ s}^{-1}$ for a 10 ks observation

significantly reduces the RGS capabilities over the wavelength ranges covered by the damaged CCDs. The inter-chip gaps between two adjacent CCDs corresponds to a spectral gap of between $\sim 85 \text{ m\AA}$ at short wavelengths and $\sim 45 \text{ m\AA}$ at long wavelengths. The RGAs produce several reflection orders of dispersed spectra with each successive order showing a decrease in sensitivity but an increase in spectral resolution (*e.g.* Figure 2.10).

The X-rays are reflected into the 1st and 2nd spectral orders with the highest efficiency and these are expected to produce the useful data in the majority of astronomical sources. The count rate in the 2nd spectral order is about a factor of 3 less than the count rate in the 1st spectral order. The spectral orders overlap spatially on the CCD detectors of the RFC, however separation of the spectral orders can be achieved by using the intrinsic energy resolution of the CCDs'. Figure 2.5 shows the X-ray spectrum (from NGC 4151) dispersed onto an RFC array and split into the spectral orders by the energy resolution of the CCD's (this is the so-called ‘banana plot’). The 1st (lower) and 2nd (upper) spectral orders are prominent and are clearly separated in the vertical direction (*i.e.* in CCD energy space).

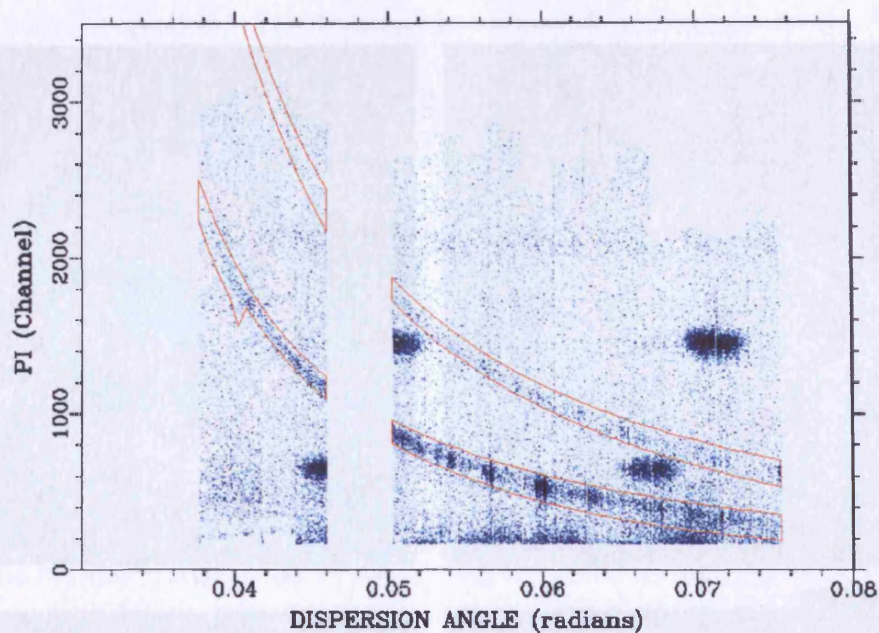


Figure 2.5: The RGS 1 ‘banana plot’ from a 60 ks observation of NGC 4151. This illustrates the mechanism used for separating 1st and 2nd spectral orders in RGS data. Standard data selection regions for the spectral orders are indicated by the red curves. The effects of low energy noise can be seen at the bottom of the image and the signals from the calibration sources (short horizontal features) are also clear.

2.3 A comparison between *XMM-Newton* and other X-ray observatories

2.3.1 X-ray imaging

In comparison with earlier X-ray satellites, *XMM-Newton*’s imaging capabilities are excellent. The spatial resolution of *XMM-Newton* is considerably superior to that of earlier hard X-ray satellites (e.g. *ASCA* and *BeppoSAX*), as demonstrated by Figure 2.6. For comparison, the Upper Panels of Figure 2.6 show false-colour X-ray images from an *ASCA* observation of NGC 4945. The spatial resolutions of the instruments on *BeppoSAX* are similar to that of the *ASCA* GIS instrument and, for simplicity, are not shown here. The Bottom-Left Panel of the same figure shows the *XMM-Newton* image of the same galaxy. *XMM-Newton* clearly resolves considerably more of the galaxy’s complex X-ray morphology than either of the *ASCA* instruments, although the SIS image does tentatively suggest the extended nature of the source (I note here that the double-peaked nature of the nucleus in the *ASCA* SIS image is caused by a chip-gap between two of the SIS CCDs, as is the rather abrupt termination of the northern edge of the galaxy). With a PSF of $\sim 6''$ (FWHM), images from *XMM-Newton* are of comparable spatial resolution to images from the High Resolution Imager (HRI) instrument on the *ROSAT* soft X-ray satellite, however the *XMM-Newton* images cover a considerably greater energy range and, thanks to its large effective area, are of considerably greater statistical quality.

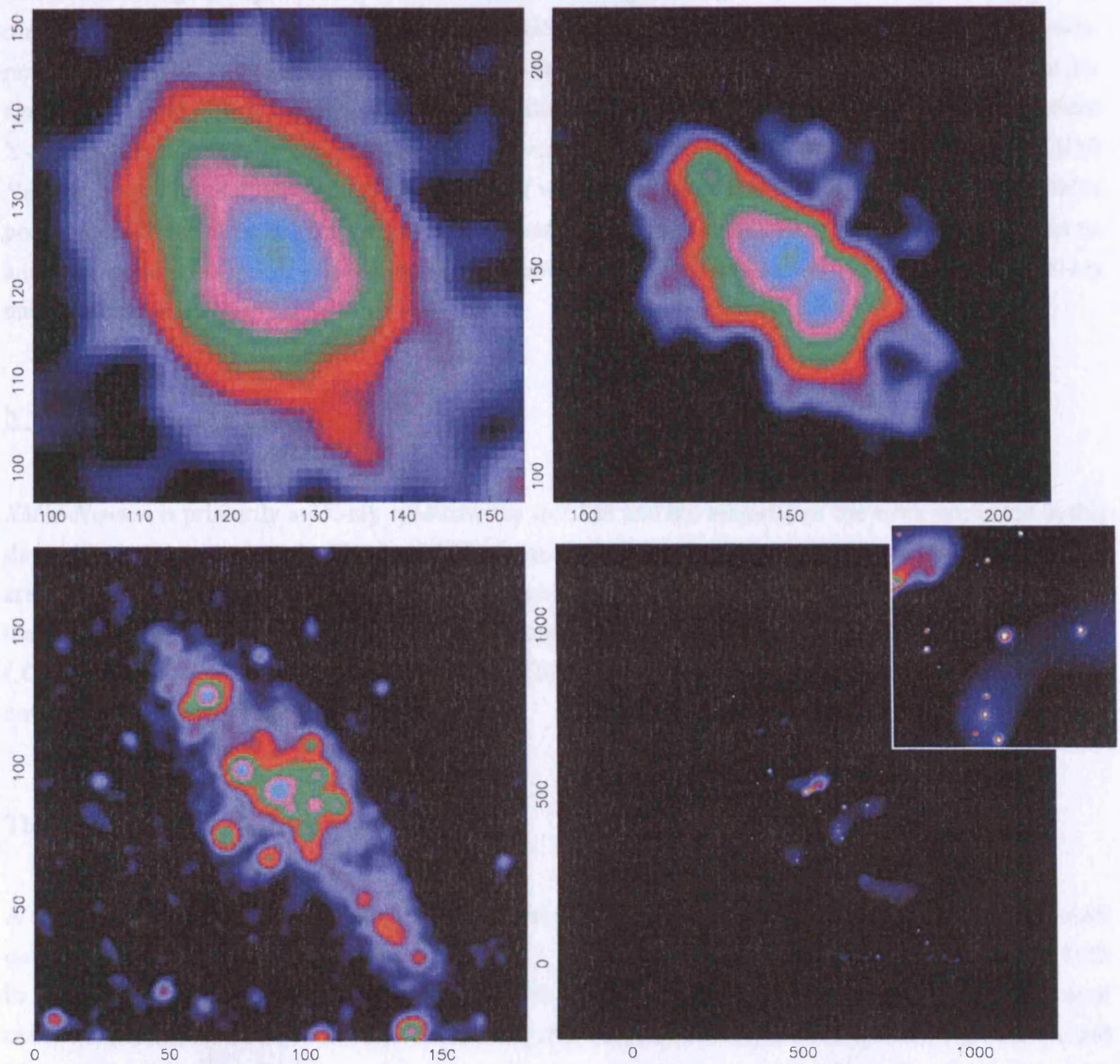


Figure 2.6: A comparison of X-ray imaging capabilities. The four, false-colour, logarithmically scaled images are of the Seyfert 2 Galaxy NGC 4945 from different X-ray satellites. Each image is $12'$ on a side and is centred on the nucleus of the galaxy. *Upper-Left Panel:* ASCA GIS image from a 63 ks observation. The image has $13'' \times 13''$ pixels and been smoothed with a $40''$ Gaussian kernel. *Upper-Right Panel:* ASCA SIS image from a 63 ks observation. The image has $6'' \times 6''$ pixels and been smoothed with a $18''$ Gaussian kernel. *Lower-Left Panel:* XMM-Newton EPIC image from a 25 ks observation (see chapter 4 for details). The image has $4'' \times 4''$ pixels and been smoothed with a $8''$ Gaussian kernel. *Lower-Right Panel:* Chandra ACIS-S image from a 34 ks observation (again, see chapter 4 for details). The image has $0.492'' \times 0.492''$ pixels and been adaptively smoothed with a Gaussian kernel. The inset shows a blow-up of a $1.5'$ square region, $\sim 1'$ (120 pixels) to the west-southwest of the nucleus of the galaxy, highlighting the numerous point sources resolved by the Chandra observation that are not easy to see in the larger scale image. This is an example of the greatly superior spatial resolving power of Chandra.

The overall imaging capabilities of *XMM-Newton* are, in general, greatly exceeded by those of *Chandra* (Figure 2.6: Lower-right panel and inset) which, with a PSF of less than $0.5''$, has the best spatial resolution of any X-ray imaging satellite ever launched. In comparison to *XMM-Newton* the *Chandra* image of NGC 4945 clearly resolves both the point source population of the galaxy and the bright extended X-ray emission near the nucleus. *Chandra* resolves many of the “point sources” evident in the *XMM-Newton* image into multiple point sources, most of which are likely to be hard X-ray binaries. Despite its poorer spatial resolution in comparison with *Chandra*, the exceptionally high throughput and moderate angular resolution of *XMM-Newton* make it somewhat more sensitive to low surface brightness X-ray emission than *Chandra*.

2.3.2 X-ray spectroscopy

XMM-Newton is primarily an X-ray spectroscopy mission and the majority of the work presented in this thesis is spectroscopy based. The nested X-ray mirrors on *XMM-Newton* make it the largest effective area focusing X-ray telescope ever launched, resulting in a uniquely sensitive observatory for studying the X-ray universe. The large collecting area is combined with the moderate spectral resolution EPIC CCD cameras and the high spectral resolution RGS instruments resulting in high quality X-ray spectra covering a wide energy range.

The EPIC cameras

A comparison of the effective areas of the *XMM-Newton* EPIC instruments with the individual detectors on other X-ray observatories is shown in Figure 2.7. This figure highlights the great improvements, both in increased effective area and increased bandwidth, that have been made with the current generation of observatories (*XMM-Newton* and *Chandra*) compared to previous X-ray observatories (e.g. *ASCA* and *BeppoSAX*). The large features in the effective area curves at ~ 0.3 , ~ 0.5 , ~ 1.7 and ~ 2.4 keV are the result of carbon, oxygen, silicon and gold in the structure of the CCD detectors and the X-ray mirrors. The large apparent difference between the EPIC MOS and the EPIC PN detectors is due to the imposition of the RGAs on the telescopes with the MOS detectors at their focus. It is interesting to note that a single EPIC MOS detector (Pink) and the *Chandra* ACIS-S instrument (Light Blue) are extremely comparable in terms of overall effective area but that the *XMM-Newton* EPIC instruments afford a somewhat greater effective area at hard energies while the *Chandra* ACIS-S instrument has a greater effective area at energies below ~ 2 keV.

A comparison of the spectra from the earlier X-ray observatories to the *XMM-Newton* EPIC detectors is shown in Figure 2.8 using the *ASCA* SIS detector as an example of the best X-ray spectra from earlier missions and the *XMM-Newton* EPIC PN detector as an example of the best CCD spectra from *XMM-Newton*. Several considerable differences are immediately apparent. The massive difference in

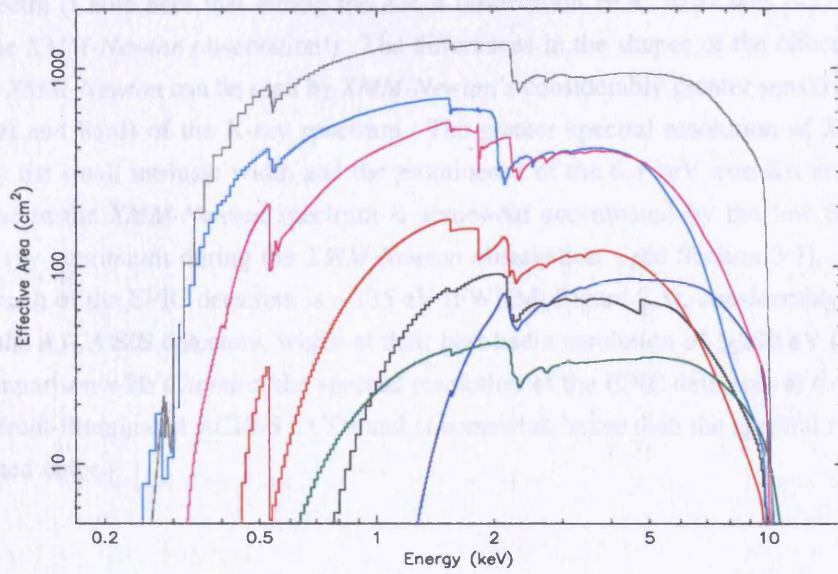


Figure 2.7: The effective areas (Logarithmic scale) of individual instruments on recent X-ray astronomy satellites (Black=ASCA GIS, Red=ASCA SIS, Green=BeppoSAX LECS, Dark Blue=BeppoSAX MECS, Light Blue=Chandra ACIS-S, Pink=XMM-Newton EPIC MOS, Grey=XMM-Newton EPIC PN).

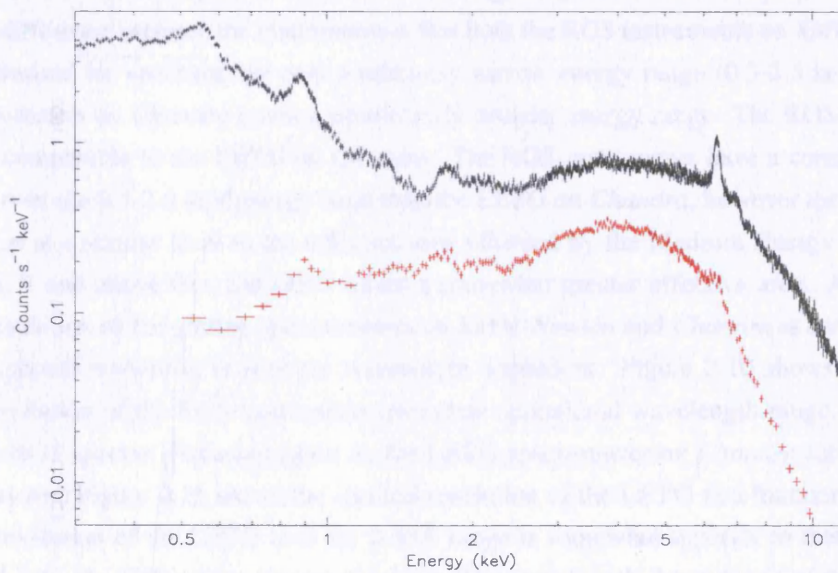


Figure 2.8: A comparison of the XMM-Newton EPIC PN (Black) and ASCA SIS (Red) spectra for NGC 4151. The ASCA spectrum shown here is from a 100 ks observation while the XMM-Newton spectrum is from a 60 ks observation.

the effective areas (shown in Figure 2.7) is immediately apparent in the comparison of the counts present in the two spectra (I note here that during the *ASCA* observation NGC 4151 was ~ 3.5 times brighter than during the *XMM-Newton* observation!). The differences in the shapes of the effective area curves for *ASCA* and *XMM-Newton* can be seen by *XMM-Newton*'s considerably greater sensitivity towards the ends (both soft and hard) of the X-ray spectrum. The greater spectral resolution of *XMM-Newton* is highlighted by the small intrinsic width and the prominence of the 6.4 keV iron $K\alpha$ emission line (although the line in the *XMM-Newton* spectrum is somewhat accentuated by the low flux level of the underlying X-ray continuum during the *XMM-Newton* observation - see Section 3.7). At 6.4 keV the resolution of each of the EPIC detectors is ~ 135 eV (FWHM; Figure 2.3), considerably better than the resolution of the *ASCA* SIS detectors, which at their best had a resolution of $\gtrsim 200$ eV (FWHM) at this energy. In comparison with *Chandra*, the spectral resolution of the EPIC detectors at 6.4 keV is similar to that of the front-illuminated ACIS-S CCDs and is somewhat better than the spectral resolution of the back-illuminated chips.

The RGS

The RGS instruments on *XMM-Newton*, along with the Low Energy Transmission Grating (LETG) and the High Energy Transmission Grating (HETG) on *Chandra*, are the first X-ray grating spectroscopy instruments to form an integral part of major X-ray astronomy observatories. A direct comparison between the effective areas of the gratings on *Chandra* and on *XMM-Newton* is presented in Figure 2.9 and strongly demonstrates the complementary nature of the grating instruments on each observatory. The most obvious difference between the instruments is that both the RGS instruments on *XMM-Newton* (Lower panel) are optimised for spectroscopy over a relatively narrow energy range (0.3-2.5 keV), whereas the grating spectrometers on *Chandra* cover a significantly broader energy range. The RGS instruments are most directly comparable to the LETG on *Chandra*. The RGS instruments have a considerably greater effective area over the 0.3-2.5 keV energy band than the LETG on *Chandra*, however the combined RGS effective area is at a similar level to the effective area afforded by the Medium Energy Grating (MEG) at about 1.5 keV and above this, the MEG offers a somewhat greater effective area. A comparison of the spectral resolution of the grating spectrometers on *XMM-Newton* and *Chandra* is complicated by the fact that the spectral resolution is strongly wavelength dependent. Figure 2.10 shows the variation of the spectral resolution of the RGS instruments over their operational wavelength range, for both the 1st and 2nd order RGS spectra. Focusing again on the LETG spectrometer on *Chandra* for the comparison with *XMM-Newton*, Figure 2.11 shows the spectral resolution of the LETG as a function of wavelength. The spectral resolution of the LETG over the 0-35Å range is somewhat superior to that of the RGS instruments, although the differences are not dramatic. The wavelength dependency of the LETG is also somewhat steeper than that of the RGS instruments, resulting in the LETG having considerably higher spectral resolution at long wavelengths.

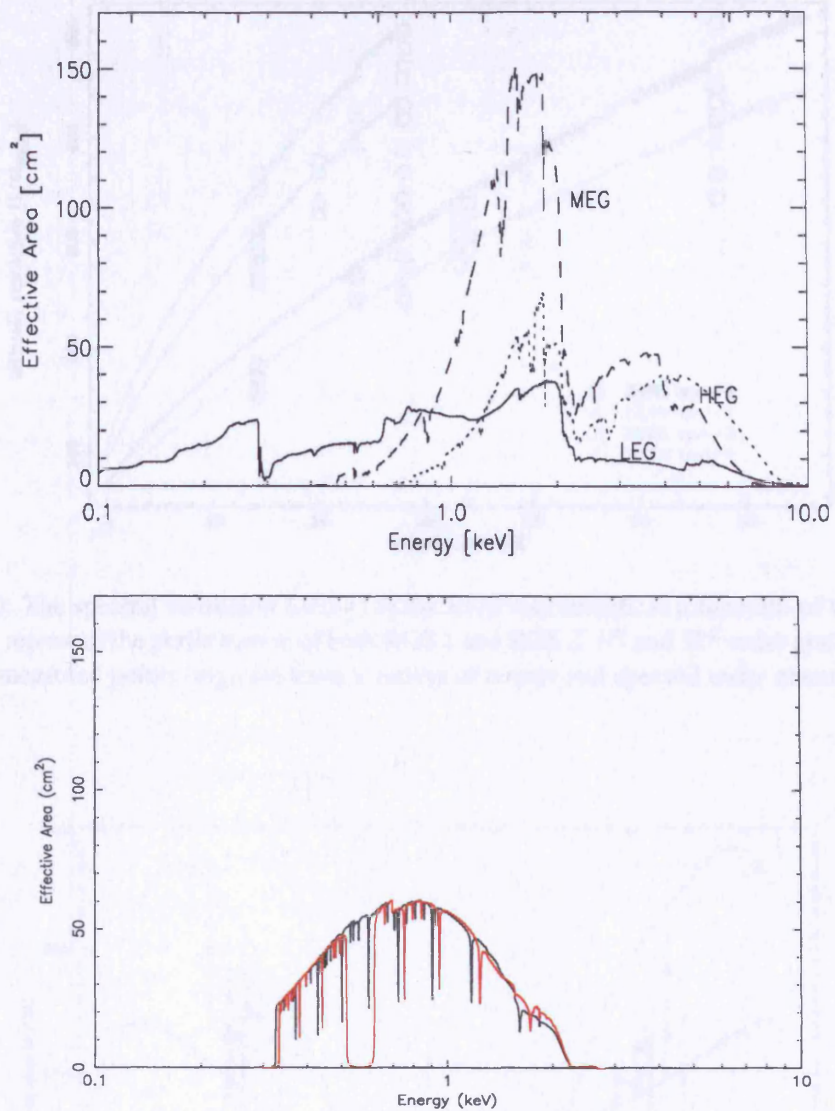


Figure 2.9: A comparison of the effective area of the *Chandra* LETG, HETG and the *XMM-Newton* RGS instruments. *Upper Panel:* The *Chandra* LETG (Solid line), MEG (Dashed line) and HEG (Dotted line) effective area curves (liner scale) (CXC 2002)[†]. The HETG instrument is a combination of the Medium Energy Grating (MEG) and the High Energy Grating (HEG) displayed separately here. The effective area curves shown here are for the co-added 1st order spectra and do not include chip-gap effects. *Lower Panel:* The *XMM-Newton* RGS 1 (Black) and RGS 2 (Red) effective area curves, on the same scale as the *Chandra* plot. The effective area curves for the RGS instruments also refer to the co-added 1st order spectra however these plots do include chip-gap effects and, as an example, the effects of one of the failed RGS CCDs is also shown.

[†]<http://cxc.harvard.edu/udocs/docs/>

2.3.3 Cross-calibration between X-ray satellites

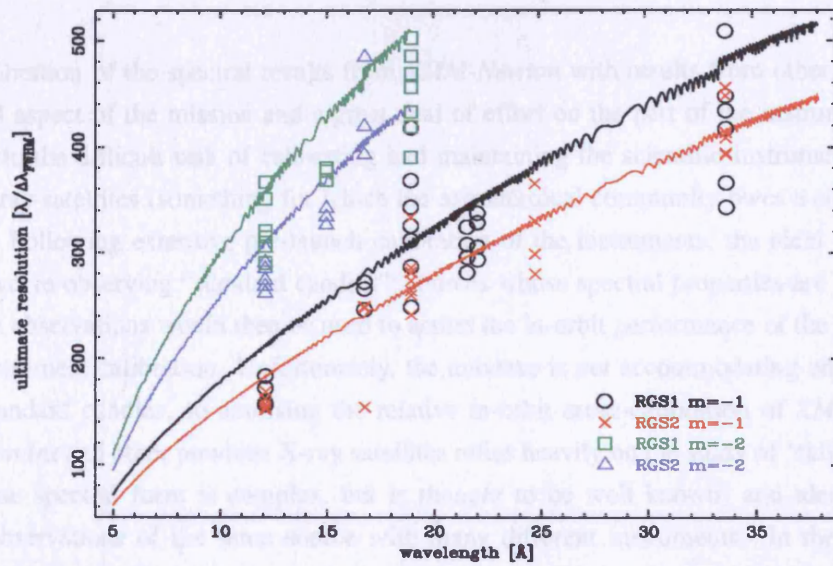


Figure 2.10: The spectral resolution ($\lambda/\Delta\lambda$) of the RGS instruments as a function of wavelength. The curves represent the performance of both RGS 1 and RGS 2, 1st and 2nd order grating spectra. Individual measured points originate from a variety of targets and spectral order extractions

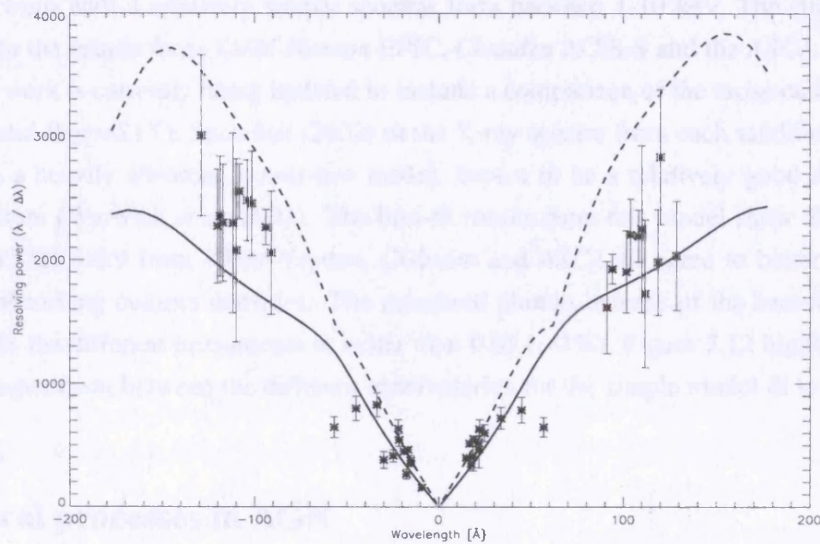


Figure 2.11: LETG spectral resolution ($\lambda/\Delta\lambda$) as a function of wavelength. The conservative solid curve is based on plausible in-flight values of the aspect, focus, and grating period uniformity. The dotted line is the theoretical performance of the LETG. The data points are derived from observations of Capella and Procyon. The curve is based only on spectral lines that are considered to be unaffected by line-blending at the LETG resolution.

2.3.3 Cross-calibration between X-ray satellites

The cross-calibration of the spectral results from *XMM-Newton* with results from other X-ray satellites is an essential aspect of the mission and a great deal of effort on the part of the instrument calibration teams goes into the difficult task of calibrating and maintaining the scientific instruments, particularly on current X-ray satellites (something for which the astronomical community owes a considerable debt of gratitude). Following extensive pre-launch calibration of the instruments, the ideal in-orbit calibration would involve observing “standard candles”; sources whose spectral properties are simple and well known. These observations would then be used to assess the in-orbit performance of the instruments and update the instrument calibration. Unfortunately, the universe is not accommodating enough to provide convenient standard candles, so assessing the relative in-orbit cross-calibration of *XMM-Newton* with respect to *Chandra* and other previous X-ray satellites relies heavily on the study of ‘calibration sources’ (sources whose spectral form is complex, but is *thought* to be well known) and ideally involves simultaneous observations of the same source with many different instruments. In the absence of the possibility of simultaneous observations, observations of spectrally constant calibration sources can be used, and hence much of the cross-calibration results mentioned briefly here are based on the spectral analysis of the galactic supernova remnant G21.5-0.9 (the sources 1E0102.0-7219 and MS1054.4-0321 are also included in the study referenced here, but their contribution to the conclusions given here are minor; Snowden 2002). G21.5-0.9 is an extended, crab-like SNR (*i.e.* it displays a centre-filled X-ray morphology) that is relatively heavily absorbed ($2.3 \times 10^{22} \text{ cm}^{-2}$; Warwick *et al.* 2001), but provides a constant spectrum with a relatively simple spectral form between 1-10 keV. The study by Snowden (2002) compares the results from *XMM-Newton* EPIC, *Chandra* ACIS-S and the *ASCA* SIS and GIS instruments (this work is currently being updated to include a comparison of the cross-calibration between *XMM-Newton* and *BeppoSAX*). Snowden (2002) fit the X-ray spectra from each satellites observation of G21.5-0.9 with a heavily absorbed power-law model, known to be a relatively good representation of the X-ray spectrum (Warwick *et al.* 2001). The best-fit results from this model show that the measured X-ray fluxes of G21.5-0.9 from *XMM-Newton*, *Chandra* and *ASCA* all agree to better than $\sim 10\%$, as do the best-fit absorbing column densities. The measured photon indexes of the best-fit power-law are consistent across the different instruments to better than 0.05 ($\sim 3\%$). Figure 2.12 highlights the quality of the spectral agreement between the different observatories for the simple model fit to this SNR.

2.4 Physical processes in AGN

This section provides a brief description of some of the physical processes that are responsible for producing and modifying the X-ray emission from AGN. The aim of this is to bring the basic characteristics of these processes to the forefront of the readers mind and to highlight the niche that each occupies in the unified AGN picture.

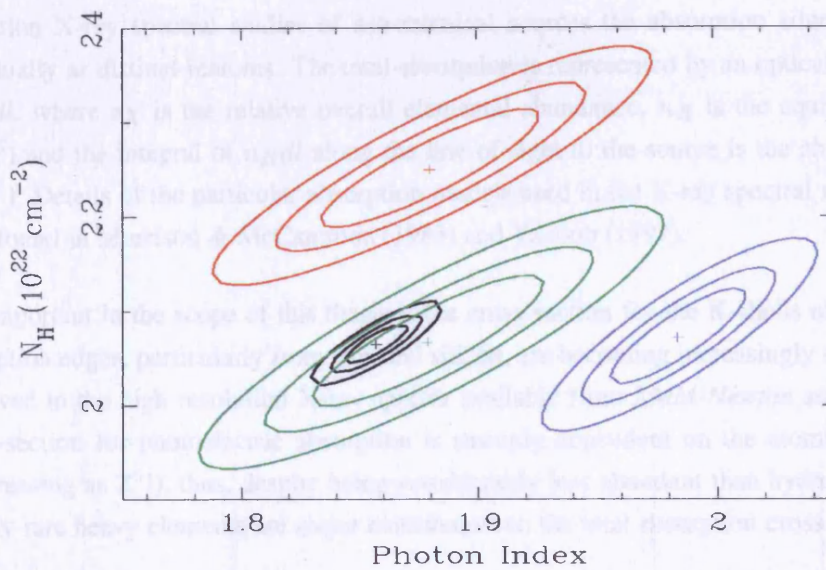


Figure 2.12: Confidence contours of absorbing column density vs. power-law photon index from the spectral fitting of *XMM-Newton* EPIC (Black), *Chandra* ACIS-S (Red) and *ASCA* SIS (Green) and GIS (Blue) observations of the SNR G21.5 -0.9. (Snowden 2002)

The overviews presented here are largely based on the excellent descriptions given in the series of books by Longair (1997) and the comprehensive astrophysics text by Carroll & Ostlie (1996).

2.4.1 Photoelectric absorption

Photoelectric absorption is the dominant process by which ultraviolet/soft X-ray photons lose energy. It is a process common in many astrophysical situations ranging from the opacity of the solar interior and stellar atmospheres to the absorption responsible for the hard X-ray spectrum of distant Type 2 quasars. The process is based fundamentally on the photoelectric effect, first presented by Einstein (1905), in which a photon with an energy $h\nu$ (where ν is the frequency of the photon) can eject electrons that have a binding energy of $E \leq h\nu$, with any remaining energy from the absorption manifesting itself as the kinetic energy of the ejected electron. The details of photoelectric absorption depend on the cross-sections for absorption of the atoms that constitute the absorbing material. The absorption cross-section for any given atomic species is extremely wavelength dependent. The energy levels within an atom for which $h\nu = E$ are known as absorption edges because, while it is impossible for photons with an energy less than E to eject an electron from this energy level, all photons with an energy greater than E are capable of ejecting the electron. For a photon with sufficient energy to eject an electron from the energy level in question, the cross-section for photoelectric absorption decreases as $\nu^{-3.5}$. The total absorption cross-section for an absorbing medium is given by the X-ray absorption coefficient $\sigma_X(\lambda)$ that, for any given wavelength, is the sum of the absorption cross-sections from all the atomic species that contribute to the opacity of the absorber.

In low resolution X-ray spectral studies of astronomical sources the absorption edges cannot be resolved individually as distinct features. The total absorption is represented by an optical depth $\tau_X(\lambda) = z_X \sigma_X(\lambda) n_H dl$, where z_X is the relative overall elemental abundance, n_H is the equivalent hydrogen density (cm^{-3}) and the integral of $n_H dl$ along the line of sight to the source is the absorption column density (cm^{-2}). Details of the particular absorption models used in the X-ray spectral modelling in this thesis can be found in Morrison & McCammon (1983) and Yaqoob (1997).

Particularly important in the scope of this thesis is the cross-section for the K-shells of atoms, because K-shell absorption edges, particularly from iron and silicon, are becoming increasingly common discrete features resolved in the high resolution X-ray spectra available from *XMM-Newton* and *Chandra*. The K-shell cross-section for photoelectric absorption is strongly dependent on the atomic number, Z , of the atom (increasing as Z^5 !), thus, despite being considerably less abundant than hydrogen and helium, astrophysically rare heavy elements are major contributors to the total absorption cross-section.

2.4.2 Fluorescent line emission

Fluorescent line emission is a combination of the absorption of energy from a photon by an electron in an atom and the radiation of some or all of this energy at a characteristic wavelength. The energy release following the absorption process is the result of an excited electron making a transition from a high energy level to a lower energy level (Figure 2.13) and is radiated as a single photon. The discrete nature of the energy levels in the atom results in each atomic transition having a specific amount of energy associated with it and hence every transition from one particular atomic energy level to another results in a photon with a specific wavelength (Figure 2.13; Right Panel). The separation of the energy levels is different for each atomic species and consequently the wavelength of a photon from a specific atomic transition is also dependent on the atomic species.

Despite the theoretical implication that all the photons from a specific atomic transition have precisely the same wavelength, observed spectral emission lines have a broadened line profile. There are several origins for this line broadening that affect all spectral lines. Spectral lines have a ‘natural width’ from the fact that the energy of any individual photon cannot have a precisely defined value, according to the Heisenberg uncertainty principle. The thermal motions of the atoms that produce the line emission also broaden the spectral lines. This is known as Doppler broadening and is dependent on the square-root of the temperature of the emitting material. The resulting line profile is known as a Voigt profile. In addition, collisional broadening, caused by a collision or close encounter with a nearby atom that perturbs the electron orbitals of the emitting atom, also affects spectral lines and is also dependent on the square-root of the temperature of the emitting material. In some cases, where the lines are produced in regions with extreme physical conditions, the profile can be additionally broadened and even skewed in shape by, for example, special and general relativistic effects (see Section 1.2).

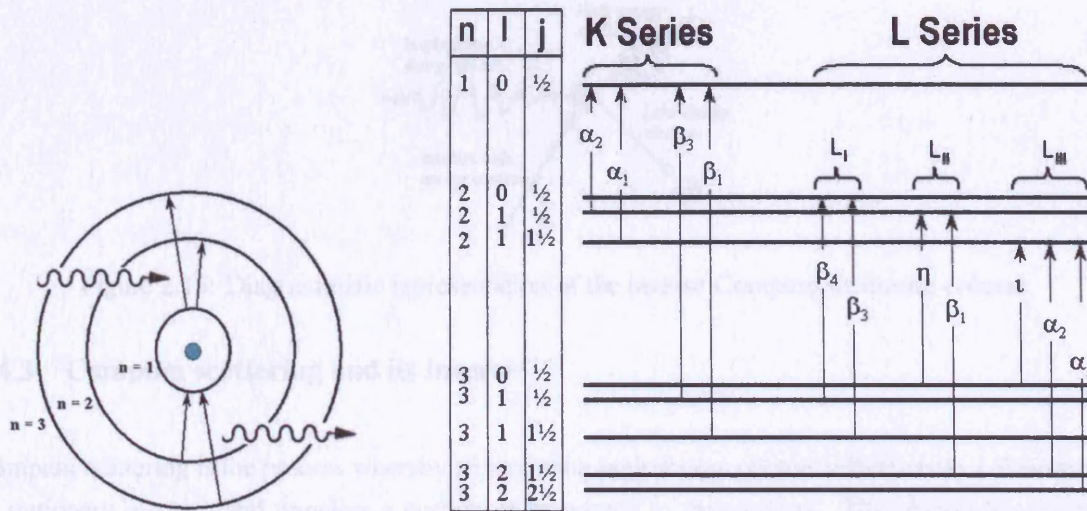


Figure 2.13: Fluorescent line emission. *Left Panel:* A simplified schematic of the absorption (top) and emission processes (bottom) processes that produce the K-shell line emission in an atom. Only electron transitions responsible for the $K\alpha$ ($n=2 \rightarrow n=1$) and $K\beta$ ($n=3 \rightarrow n=1$) emission lines are shown in this diagram for simplicity. *Right Panel:* X-ray energy level diagram showing the K series (transitions to the K-shell) and L series (transitions to the L-Shell) transitions in a heavy atom. The diagram shows the transitions permitted by the $\Delta l = \pm 1$; $\Delta j = -1, 0$ selection rules. Only the $n=1, 2$ and 3 shell transitions are shown on this diagram for simplicity and the principle quantum numbers of the energy levels are shown on the left of the energy level diagram (adapted from Richtmyer, Kennard & Lauitsen 1955).

Particularly important in the scope of this thesis are the fluorescent $K\alpha$ lines from neutral, astrophysically abundant, ‘metals’ (‘metals’ here refers to any atomic species other than hydrogen and helium), particularly those from neutral iron and silicon. Neutral iron $K\alpha$ emission lines have been previously observed in low resolution X-ray spectra of AGN and with the advent of high resolution X-ray spectroscopy the details of the iron $K\alpha$ line emission and the presence of $K\alpha$ line emission from neutral silicon and other heavy elements is becoming increasingly common.

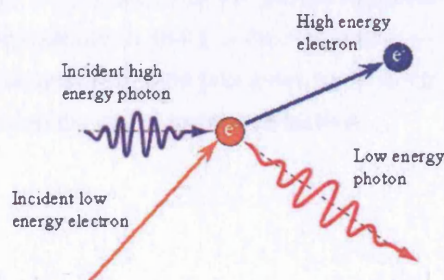


Figure 2.14: Diagrammatic representation of the Compton scattering process

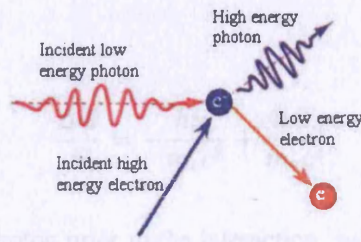


Figure 2.15: Diagrammatic representation of the inverse Compton scattering process

2.4.3 Compton scattering and its inverse

Compton scattering is the process whereby an incoming high energy photon collides with a slow-moving or stationary electron and transfers a portion of its energy to the electron. The photon leaves the interaction with an increased wavelength, and the electron leaves the interaction with an increased kinetic energy (Compton 1923a, Compton 1923b). This is shown diagrammatically in Figure 2.14. Traditionally the wavelength change from a single Compton scattering is described in terms of the fractional increase in wavelength of the photon, given by:

$$\frac{\Delta\lambda}{\lambda} = \frac{h\nu_0}{m_e c^2} (1 - \cos\theta) \quad (2.1)$$

where m_e is the mass of the electron, ν_0 is the frequency of the photon prior to the collision and θ is the scattering angle. $h\nu_0/m_e c^2$ is known as the “Compton wavelength” and has a value of $h\nu_0/m_e c^2 = 0.025\text{\AA}$ (~ 510 keV). The inverse of this process occurs when an extremely high energy (*i.e. a relativistic*) electron collides with a lower energy photon and transfers some of its energy to the photon. This results in the photon leaving the interaction with a decreased wavelength and the electron leaving the interaction with a decreased kinetic energy. This is shown diagrammatically in Figure 2.15. The effect of this energy gain on the frequency of a photon with $h\nu \ll \gamma m_e c^2$, following a single inverse Compton scattering from a high energy electron, is that $\nu \approx \gamma^2 \nu_0$ where ν is the photon frequency following the interaction, ν_0 is the photon frequency prior to the interaction and γ is the relativistic γ -factor of the high energy electron. Compton scattering and its inverse are prominent processes in the X-ray emission from AGN particularly in producing the hard X-ray continuum and Compton reflection.

Thermal Comptonization

The process of Comptonization in general refers to the scenario where Compton scattering or inverse Compton scattering primarily determines the X-ray spectrum of a source. If the population of electrons involved in the Compton scattering has a thermal distribution of velocities with a characteristic temperature, T_e , then the net energy change of a photon involved in a single thermal Comptonization collision is

given by:

$$\frac{\Delta E}{E} = -\frac{h\nu_0}{m_e c^2} + \frac{4kT_e}{m_e c^2} \quad (2.2)$$

where ν_0 is the frequency of the photon prior to the interaction, m_e is the mass of the electron and k is the Boltzmann constant. This equation establishes a clear set of scenarios in which energy is transferred between the electron and photon involved. In the scenario where $h\nu_0=4kT_e$ no energy is transferred between the particles, in the case where $h\nu_0 > 4kT_e$ energy is transferred from the photons to the electrons and in the scenario where $h\nu_0 < 4kT_e$ energy is transferred to the photons. In many AGN models, a corona of hot electrons with a thermal distribution surrounds the accretion disk and the thermal emission from the accretion disk itself provides a source of soft (*i.e.* low energy) photons. The soft disk photons are Comptonized in the hot electron corona and are sufficiently up-scattered to produce the observed X-ray spectrum. Figure 2.16 shows a simulated thermal Comptonized X-ray continuum spectrum (Wilms 1998). The total continuum from thermal Comptonization, in this case, is extremely flat between 0.1 and ~ 30 keV and can be well approximated by a power-law, however it is possible to construct physical conditions that will significantly reduce the average number of scatterings a photon undergoes. This will result in a smaller contribution to the overall spectrum from the higher scattering orders producing a total spectrum that may show significant spectral curvature and in this case the 0.1-30 keV spectrum may not be well approximated by a power-law.

The production of X-rays through magnetic flaring on the surface of the accretion disk is an alternative mechanism for generating the underlying X-ray continuum. This mechanism also relies on Comptonization for the production of the X-ray emission however in this case the electrons involved in the interaction are travelling relativistically along the magnetic field lines in the flares and have a non-thermal distribution. This produces an X-ray continuum with a somewhat different spectral shape (Wardziński & Zdziarski 2001 and references therein). A concise description of the Comptonization process can be found in Pozdnyakov, Sobol & Sunyaev (1983) and for details of the vital role of thermal Comptonization in AGN see, for example, Haardt & Maraschi (1993); Zdziarski *et al.* (1994); Zdziarski, Johnson & Magdziarz (1996); Zdziarski, Poutanen & Johnson (2000) and Petrucci *et al.* (2000).

Compton reflection

Compton reflection is not a genuine ‘reflection’ process, rather it is the product of photoelectric absorption and Compton scattering. For photon energies of ~ 15 keV or less the optical depth for photoelectric absorption in cold, neutral, gas is considerably greater than that of Compton scattering, resulting in most of the incident photons with these energies being absorbed. Conversely, Compton scattering dominates over photoelectric absorption for photon energies much greater than 15 keV and these photons are down-

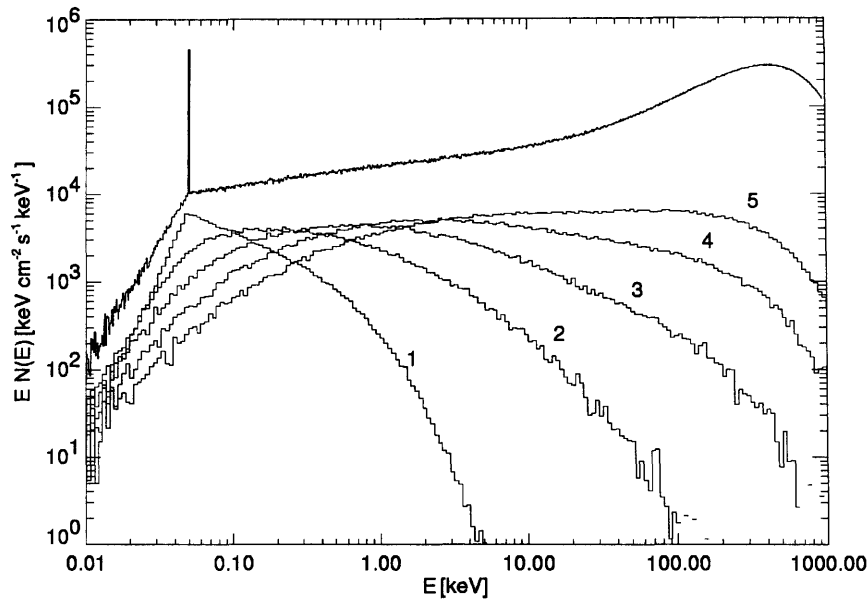


Figure 2.16: The X-ray spectrum produced by thermal Comptonization from a sphere of hot gas with an optical depth $\tau=5$ and a uniform electron temperature of $T_e \sim 205$ keV. Seed photons were injected with an energy of 50 eV from a point source at the centre of the sphere. The spectra labelled 1-5 are the emerging spectra for the scattering orders (*i.e.* the photons that have undergone 1-5 scatterings respectively) and the top spectrum is the total resulting spectrum. (Wilms 1998)

scattered to a lower energy. Each successive Compton scattering reduces the energy of the photon until it is either absorbed or scattered out of the medium. The resulting combination of these effects produces a spectrum with a broad hump peaking around 30 keV. Figure 2.17 shows the simulated Compton reflection spectrum from a cold slab of gas (with solar elemental abundances) that is irradiated by a power-law X-ray continuum. Figure 2.17 clearly highlights the additional impact that heavy elements (particularly iron), present in the reflecting medium, have on the resulting Compton reflection spectrum. The heavy elements impact the spectrum at energies less than ~ 10 keV, primarily in the form of an imprinted iron K edge at ~ 7.1 keV and the associated iron $K\alpha$ and $K\beta$ emission lines at ~ 6.4 and ~ 7.0 keV, respectively.

In the unified AGN picture Compton reflection can originate from several locations, namely the central accretion disk or from the material that forms the putative molecular torus. In the first case the Compton reflection spectrum can be strongly affected by ionization effects, particularly if the reflecting material is located in the inner regions of the accretion disk where the underlying X-ray continuum is thought to strongly ionize the accretion disk material. This can significantly alter the shape of the resulting Compton reflection spectrum, particularly below ~ 10 keV. Compton reflection from neutral material in the outer regions of the disk or from the cold, neutral, material of the torus will produce a spectrum similar to that shown in Figure 2.17. It is important to note that the Compton reflection spectrum from a torus or the outer accretion disk is expected to respond slowly to the *time-averaged* level of the central X-ray continuum, and as such there is no specific reason why the flux of the Compton reflection component should be directly related to the flux of the X-ray continuum at any given moment. This is not the case for

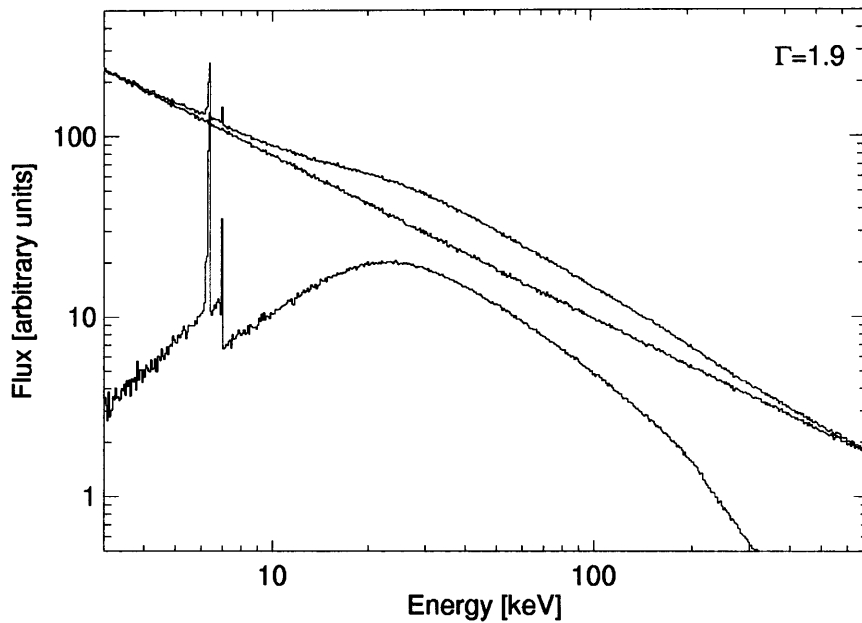


Figure 2.17: Compton reflection spectrum from a slab of cold material (with solar element abundances) irradiated by a power-law X-ray continuum spectrum. The spectrum at the bottom is the resultant Compton reflection spectrum and the top two spectra show the incident power-law continuum and the total resulting X-ray spectrum from the incident and reflected spectra. Note the strong iron K-shell features imprinted on the reflection spectrum. (Wilms 1998)

Compton reflection produced in the inner regions of the accretion disk, close to the region responsible for the production of the X-ray continuum, which is expected to respond rapidly to changes in the continuum flux (although its response may be complicated, for example, by rapid changes in the ionization of the reflecting material in response to changes in the X-ray continuum flux).

Chapter 3

The hard X-ray spectrum of NGC 4151

3.1 Overview: A complex mix of absorption, continuum and reprocessed continuum features.

This chapter presents a detailed analysis of the complex hard (2.5-12 keV) X-ray spectrum of the bright nearby Seyfert galaxy NGC 4151. The chapter concentrates on two main areas. The first part reports on the analysis of *BeppoSAX* and *ASCA* data and highlights both the complex nature of the X-ray absorption inherent to NGC 4151 and the strong impact of Compton reflection on the properties of the X-ray spectrum. The absorption arises in both warm (*i.e.* partially photoionized) and cold gas present in the line-of-sight to the active nucleus of the source, which impacts on the X-ray spectrum between 2-6 keV. A 1-100 keV spectral template model, which incorporates both complex absorption and Compton reflection, was constructed utilizing the large bandpass and medium spectral resolution afforded by *BeppoSAX*. The spectral template model is then applied to an archival *ASCA* long-look of NGC 4151 with a remarkable degree of success, highlighting that it is the level of the continuum which is the main driver of the complex spectral variability exhibited by NGC 4151. The second part of the chapter details the analysis of the recent *XMM-Newton* observations of NGC 4151, using the template spectral model developed in the earlier sections of the chapter. Again the template model does an excellent job of modelling the hard X-ray spectrum, reinforcing the earlier conclusions. However the majority of the *XMM-Newton* data analysis focuses on the properties of the iron K-shell features imprinted on the X-ray spectrum. The spectral modelling highlights the lack of any strong relativistically broadened iron $K\alpha$ line and provides a strong hint that the cold medium present in the NGC 4151 nucleus has an iron abundance at least twice the solar value.

The chapter is organised as follows. Section 3.2 describes some of the extensive background and history regarding the X-ray study of NGC 4151. The spectral template model is specified in Section 3.3 and

the relevant spectral parameters are determined using a recent, long, *BeppoSAX* observation. Section 3.4 gives the details of the *ASCA* long-look observation and an outline of the relevant data reduction, along with a characterisation of the flux and spectral variability apparent in the source light-curve. Detailed spectral modelling of the *ASCA* data is described in Section 3.4.1 and Section 3.4.2, focusing on the evidence for a photoionized absorber. Section 3.5 discusses the implications of these results in the context of both previous and future studies. The most recent observations of NGC 4151 from *XMM-Newton* are introduced and discussed in Section 3.7, including detailed modelling of the EPIC spectra focusing on the iron features observed in the spectrum. Section 3.8 discusses the implications of the *XMM-Newton* analysis, particularly with reference to the recent *Chandra* observation of NGC 4151.

3.2 NGC 4151

The Seyfert galaxy NGC 4151 was identified as an X-ray source over thirty years ago (Gursky *et al.* 1971). As one of the brightest AGN accessible in the X-ray band, it has been extensively studied by missions such as *EXOSAT*, *Ginga*, *ROSAT*, *ASCA*, *CGRO* and more recently *RXTE*, *BeppoSAX*, *Chandra* and *XMM-Newton*. This observational focus has revealed that the X-ray spectrum of NGC 4151 from 0.1-100 keV is comprised of a complex mixture of emission and absorption components, probably originating at a variety of locations from the innermost parts of the putative accretion disk, out to the extended NLR of the galaxy. Given this spectral complexity it remains to be seen whether NGC 4151 should or should not be considered as an archetype of its class (Ulrich 2000; Zdziarski *et al.* 2002).

The intrinsic X-ray to γ -ray continuum emanating from the active nucleus of NGC 4151 appears to be produced by the thermal Comptonization of soft seed photons (e.g. Section 2.4.3; Haardt & Maraschi 1993; Zdziarski *et al.* 1994; Zdziarski, Johnson & Magdziarz 1996; Zdziarski, Poutanen & Johnson 2000; Petrucci *et al.* 2000). Features associated with continuum reprocessing in material surrounding the active nucleus are also present, in the form of Compton reflection and iron K fluorescence features (e.g. Maisack & Yaqoob 1991; Yaqoob *et al.* 1995; Zdziarski, Johnson & Magdziarz 1996; Warwick *et al.* 1996; Piro *et al.* 2002, Zdziarski *et al.* 2002). Below ~ 5 keV the hard X-ray continuum is strongly cut-off by photoelectric absorption in a substantial ($N_H \sim 10^{23} \text{ cm}^{-2}$) line-of-sight gas column density (e.g. Holt *et al.* 1980; Yaqoob *et al.* 1993; Weaver *et al.* 1994a; Weaver *et al.* 1994b).

One of the long-standing problems in X-ray studies of NGC 4151 has been to understand the exact nature and origin of this absorption. X-ray observations show very clearly that the cut-off is not as abrupt as one might expect for absorption in a uniform slab of cold solar abundance material (i.e. the increase in opacity with decreasing photon energy is less rapid than predicted for a uniform cold absorber). Various solutions have been suggested including an inhomogeneous cold absorber (the partial covering model; Holt *et al.* 1980; Weaver *et al.* 1994b), an absorber with grossly non-solar abundances (Yaqoob & Warwick 1991) and the partial photoionization of the absorbing medium (i.e. the warm absorber model, e.g. Krolik

& Kallman 1984). However, none of these has provided a satisfactory explanation of the nature of the absorber or the processes which gives rise to the large changes in the absorption apparent in NGC 4151 on timescales of days or longer (Yaqoob, Warwick & Pounds 1989; Yaqoob *et al.* 1993). Unfortunately the presence of additional soft X-ray emission components which first appear at ~ 2 keV and dominate the spectrum below ~ 1 keV (Weaver *et al.* 1994a; Warwick, Done & Smith 1995) dramatically complicates the situation. *EINSTEIN* and *ROSAT* High Resolution Imager (HRI) measurements (Elvis, Briel & Henry 1983; Morse *et al.* 1995) and, more recently, observations by *Chandra* (Ogle *et al.* 2000; Yang, Wilson & Ferruit 2001) have revealed that much of this soft emission emanates from a spatially resolved (~ 1.6 kpc) highly ionized plasma coincident with the optical NLR of the galaxy.

A second long-standing issue for X-ray studies of NGC 4151 has been the nature and origin of the iron $K\alpha$ emission line. Some earlier studies based on *ASCA* observations concluded that the profile of the iron $K\alpha$ line is complex and may be composed of an intrinsically narrow component plus a relativistically broadened line feature (Yaqoob *et al.* 1995; Wang, Zhou & Wang 1999). Furthermore the broad line profile has been reported to be variable on timescales of 10^4 s, corresponding to an emitting region of < 0.02 AU, suggesting an origin close to the supermassive black hole presumably in the inner regions of a putative accretion disk (Wang, Wang & Zhou 2001). However, alternative interpretations of the broadband *ASCA* spectra do not require the presence of an extremely broad iron line in NGC 4151 (Schurch & Warwick 2002; Takahashi, Inoue & Dotani 2002). The correct interpretation of the nature of the iron $K\alpha$ line remains controversial.

3.3 The *BeppoSAX* data and the spectral template model

The broad bandpass of the instruments on *BeppoSAX* is of tremendous help when attempting to constrain the form of the hard X-ray spectrum of NGC 4151. During the period 1996-1999, NGC 4151 was observed three times with *BeppoSAX* (Schurch & Warwick 2002; Piro *et al.* 2002). The observation used here was carried out in January 1999, and provides the best signal to noise ratio of the available *BeppoSAX* datasets. X-ray data from three of the four instruments on *BeppoSAX* [namely the Low-Energy Concentrator Spectrometer (LECS), Medium-Energy Concentrator Spectrometer (MECS) and Phoswich Detection System (PDS) instruments - see Parmar *et al.* 1997, Boella *et al.* 1997, Frontera *et al.* 1997 respectively] were obtained from the Agenzia Spaziale Italiana (ASI) Science Data Centre. In the case of the LECS and MECS instruments, source spectra were pre-processed via standard *BeppoSAX* procedures using on-source extraction regions of $6'$ and $4'$ radius respectively. Standard blank-sky background files were available for the LECS and MECS whereas in the case of the PDS instrument, background-subtracted source spectra were supplied directly. The spectra were accumulated over the full observation giving an effective on-source exposure time of 83 ks in the MECS and roughly half this for the other instruments.

The BL Lac object MS 1207.9+3945 is located $\sim 5'$ to the north of NGC 4151. The contamination of the NGC 4151 spectra is negligible for the MECS instrument ($\sim 2\%$) but, on the basis of the Piro *et al.* (2002) figures, the contamination may be as high as $\sim 20\%$ in the LECS at ~ 1 keV. In practice the presence of this source in the LECS instrument will have little overall impact on our spectral fitting (given the relatively soft spectrum of the BL Lac - Warwick, Done & Smith (1995)).

Spectral fitting was carried out using the XSPEC (v11.0.1) software package with the Sept 1997 instrument response matrices. For this purpose the source spectra were grouped to give a minimum of 20 counts per bin to allow the use of χ^2 minimisation techniques (e.g. Yaqoob 1998; Protassov *et al.* 2002) and the data below 1 keV from the LECS instrument were excluded to avoid complications relating to the form of the soft X-ray emitting components and the presence of the BL Lac. A template spectral model is adopted for the spectral fitting that includes the following emission components:

1. A power-law continuum with a normalization, A_1 , and photon index, Γ , exhibiting a high energy break at 100 keV;
2. A neutral Compton-reflection component (modelled by the `pexrav` model in XSPEC; Magdziarz & Zdziarski 1995) with only the reflection scaling factor, R , as a free parameter (in this model the reflection scaling parameter is defined such that $R=1$ corresponds to Compton-reflection from a uniform slab of material that covers 2π steradians of the sky as viewed from the emitting source). The parameters relating to the incident continuum were tied to those of the hard power-law component. In addition $\cos i$ was fixed at 0.5 and the metal abundance in the reflector was fixed at the solar value;
3. An iron $K\alpha$ emission line of intensity $I_{K\alpha}$ and a centroid energy $E_{K\alpha}$ (with an intrinsic line width $\sigma_{K\alpha}$ set to 0.1 keV, based on previous analysis of ASCA datasets not presented in this work);
4. A second power-law continuum is included as a gross parameterisation of all the additional soft X-ray emitting components. The power-law slope is coupled to that of the primary hard continuum power-law, but with the normalization, A_2 , as a free parameter. This representation is *not* intended as a physical interpretation of the soft X-ray emission. The soft X-ray emission is known to be comprised largely of emission lines (Ogle *et al.* 2000), and the nature and details of this emission are discussed in detail in Chapter 6.

As noted earlier, the complex absorption of the hard X-ray continuum in NGC 4151 has previously been modelled in number of ways, with arguably the most successful approach being the partial covering model (sometimes referred to in the literature as a dual absorber model e.g. Holt *et al.* 1980; Yaqoob & Warwick 1991; Weaver *et al.* 1994b). In the partial covering scenario a fraction, f_{cov} , of the hard continuum is absorbed by a cold gas column density, $N_{H,1}$, whilst the remaining fraction of the continuum emission, $1 - f_{cov}$, intercepts a smaller column density, $N_{H,2}$. Despite the success of this

Table 3.1: The results of fitting the template spectral model to the *BeppoSAX* data. The notation d-o-f stands for degrees of freedom.

Model Parameter	Best-Fit Value	Units
$N_{H,warm}$	$23.9^{+0.9}_{-0.9}$	10^{22} cm^{-2}
$N_{H,cold}$	$3.4^{+1.1}_{-0.8}$	10^{22} cm^{-2}
Γ	$1.65^{+0.02}_{-0.03}$	
R	$0.37^{+0.18}_{-0.15}$	
$\log(\xi)$	$2.48^{+0.06}_{-0.03}$	
A_1	$4.6^{+0.2}_{-0.2}$	$10^{-2} \text{ photon keV}^{-1} \text{ cm}^{-2} \text{ s}^{-1}$
A_2	$1.8^{+0.1}_{-0.1}$	$10^{-3} \text{ photon keV}^{-1} \text{ cm}^{-2} \text{ s}^{-1}$
$E_{K\alpha}$	$6.37^{+0.03}_{-0.02}$	keV
$I_{K\alpha}$	$3.4^{+0.4}_{-0.3}$	$10^{-4} \text{ photon cm}^{-2} \text{ s}^{-1}$
χ^2	832	
d-o-f	815	

model, the analysis presented here focuses on a model employing the same number of free parameters but with the absorber stratified along the line-of-sight rather than perpendicular to it. In this scenario the complex absorber is represented as a product of two absorption components, namely a warm column density, $N_{H,warm}$, and a cold gas column, $N_{H,cold}$. The warm absorption is modelled using an XSPEC multiplicative table model, previously generated via the photoionization code XSTAR (Griffiths 1999; Kallman & Krolik 1997). The ionization state of the warm gas is governed by an ionization parameter, given by:

$$\xi = \frac{L_{ion}}{n r^2} \quad (3.1)$$

Where L_{ion} is the source luminosity in the 0.0136-13.6 keV bandpass (erg s^{-1}). n is the number of hydrogen atoms/ions in the gas (cm^{-3}) and r is the distance from the central source to the inner edge of the warm cloud (cm). The form of the ionising continuum was adopted from Krolik & Kriss (1995). For further details of the photoionization modelling see Griffiths *et al.* (1998) & Griffiths (1999). The cold absorption was represented by the **wabs** model in XSPEC which is based on the absorption cross-sections tabulated in Morrison & McCammon (1983). Solar abundances in both the warm and cold absorber are assumed.

The adopted spectral model assumes that *only* the hard power-law continuum is subject to the complex absorption. However absorption arising in the line-of-sight column density through our own Galaxy is

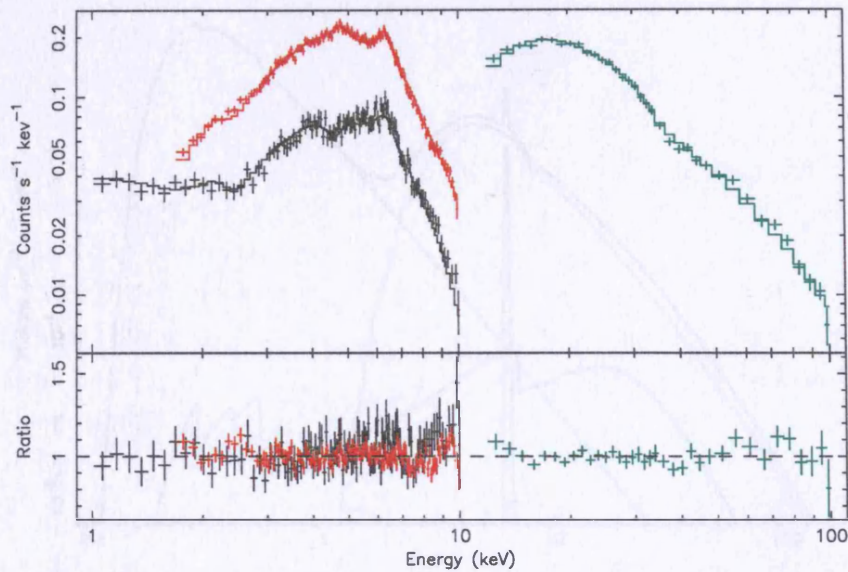


Figure 3.1: The *BeppoSAX* LECS (black), MECS (red) and PDS (green) data fitted with the template spectral model. *Upper panel*: The count rate spectra and best-fit model. *Lower panel*: The ratio of the data to the best-fit model.

applied to all four emission components ($N_{H,Gal} = 2 \times 10^{20} \text{ cm}^{-2\dagger}$).

The results of fitting this spectral template to the *BeppoSAX* data are listed in Table 3.1, which details the best-fitting values for the nine free parameters of the model. The quoted errors (here as elsewhere in the thesis) are 90% confidence levels as defined by a $\Delta\chi^2=2.71$ criterion (*i.e.* assuming one interesting parameter).

The template spectral model provides an excellent fit to the *BeppoSAX* data as illustrated in Figure 3.1. Figure 3.2 shows the corresponding best-fitting model spectrum.

3.4 The ASCA long-look observation

Having defined the spectral template from *BeppoSAX*, the focus of the spectral modelling now shifts to the final observation of NGC 4151 carried out by *ASCA* during the period 12th-25th May, 2000. This exceptionally long observation (~ 13 days) was carried out during the last phase of the *ASCA* programme, fully meriting its description as a “long-look”. The *ASCA* payload included four X-ray telescopes, two equipped with Solid-state Imaging Spectrometers (SIS) and two with Gas Imaging Spectrometer (GIS) instruments. All the relevant datasets pertaining to the SIS and GIS instruments were obtained from the *ASCA* public archive at the High-Energy Astrophysics Science Archive Research Centre (HEASARC[†]).

[†]<http://heasarc.gsfc.nasa.gov/>

[‡]<http://heasarc.gsfc.nasa.gov/>

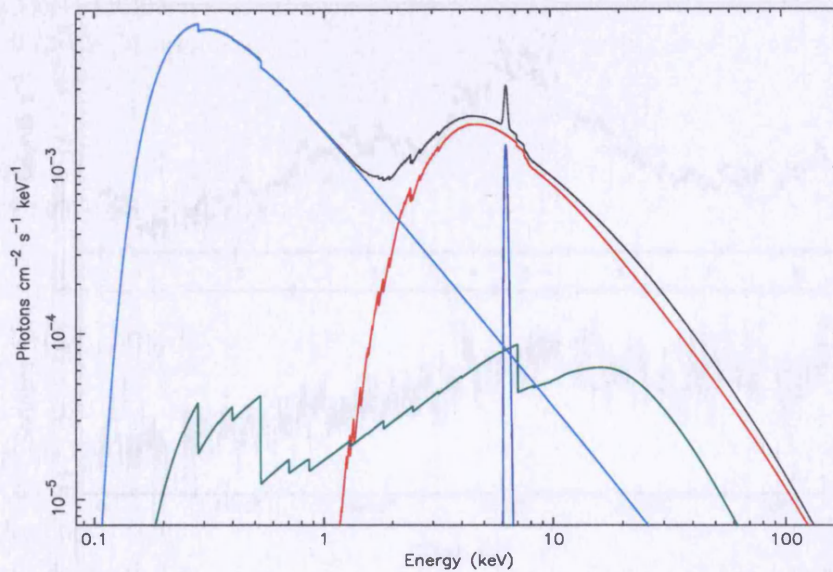


Figure 3.2: The spectral template model giving the best-fit to the *BeppoSAX* data. There are four emission components comprising of an absorbed hard power-law continuum (red), neutral Compton reflection (green), a neutral iron $K\alpha$ fluorescence line (dark blue) and a second power-law providing a gross representation of the soft X-ray emitting components (light blue). All the emission components are subject to Galactic absorption.

Standard screening criteria and data reduction techniques were employed using software routines within the FTOOLS software package. During the long-look observation the SIS instruments were operated in single CCD mode with the nearby BL Lac object positioned at the very edge or just off-chip in the SIS-0 and SIS-1 instruments respectively. In an attempt to reduce both the impact of the instrument background and the contamination from the BL Lac to negligible proportions, a $1'$ radius source extraction circle was used for the extraction of the SIS data. Compared to a more standard $3'$ radius extraction cell, this reduced the 1-10 keV SIS count rate by $\sim 11\%$. For the GIS data a $3'$ radius source extraction region was used and a background spectrum was taken from an off-source region in the GIS field of view.

As discussed recently in Turner *et al.* (2001b), towards the end of the missions life the *ASCA* SIS detectors showed a significant degradation in efficiency at lower energies, which was probably due to increased dark current levels and decreased Charge Transfer Efficiency (CTE), producing SIS spectra which diverge from each other and from the GIS data. Furthermore, data from the latter phases of the mission (specifically AO-8 and later observations) revealed a non-linear evolution of the SIS CTE. An interim solution, released on 13th February, 2001, by the *ASCA* guest observer facility (in the form of the CTE correction file *sisph2pi_130201.fits*), has been applied to the data analysed here which reduces some but not all of the spectral inconsistencies (see Section 3.4.1). To minimize the impact of the remaining spectral uncertainties arising from the poor low-energy calibration of the SIS instruments (e.g. Appendix A of Weaver, Gelbord & Yaqoob 2001), in this analysis the SIS data was restricted to the 1-10 keV band. The total accumulated on-source exposure was 285 ks in the SIS and 435 ks in the GIS detectors.

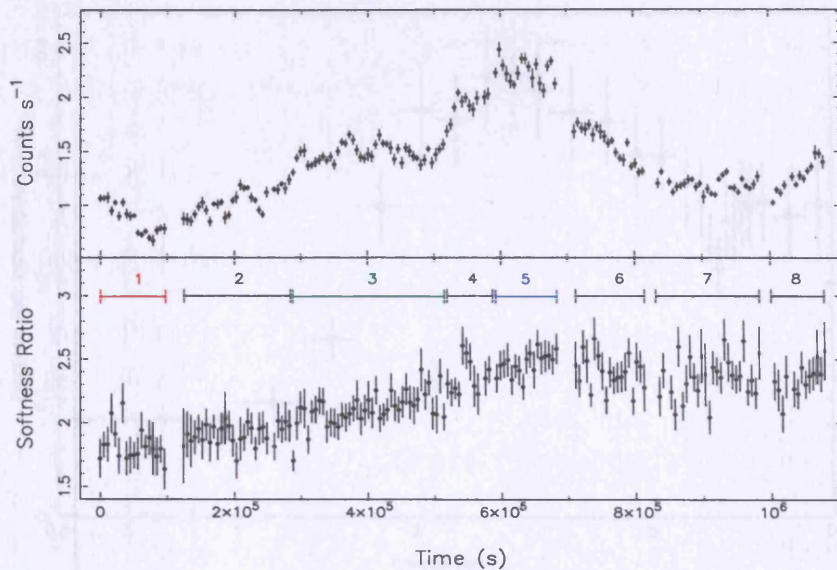


Figure 3.3: *Upper panel:* the combined SIS 1-10 keV X-ray light-curve from the long-look ASCA observation. *Lower panel:* The variation of the 2-5 keV/5-10 keV softness ratio during the observation. The horizontal bars illustrate how the observation was split into eight time segments for the spectral analysis. The coloured horizontal bars indicate the segments for which spectra are shown in Figure 3.6.

The light-curve in the full 1-10 keV band is shown in Figure 3.3 for the combined SIS instruments. An almost identical light-curve is obtained for the combined GIS instruments demonstrating that, at least in terms of the broad-band variability, the two SIS and GIS instruments produce very similar results. During the ~ 13 day observation the source shows a significant brightening by a factor of more than three followed by a comparable decline. The fastest variation is a flux increase of $\sim 35\%$ in roughly 12 hours. Figure 3.3 also shows the 2-5 keV/5-10 keV softness ratio versus time (again, for simplicity only the SIS data are shown here). The brightening of the source is clearly associated with significant spectral softening, although the spectrum remains relatively soft during the subsequent decline in flux.

The spectral variability exhibited by NGC 4151 is dramatically emphasised by the fractional rms variability amplitude as a function of energy (Edelson *et al.* 2002), shown in Figure 3.4. This demonstrates, in a model independent fashion, the steep rise in the amplitude of the variability above 1 keV to a maximum at ~ 3 keV, followed by a shallow decline at higher energies. There is also a hint of a dip at the energy of the iron $K\alpha$ line (6.2-6.6 keV), implying that the iron $K\alpha$ line may be considerably less variable than the underlying hard X-ray continuum.

3.4.1 Fitting the spectral template model

In order to study the precise nature of the spectral variability exhibited by NGC 4151, the long-look observation was broken up into eight sections utilizing gaps in the light-curve to define section boundaries

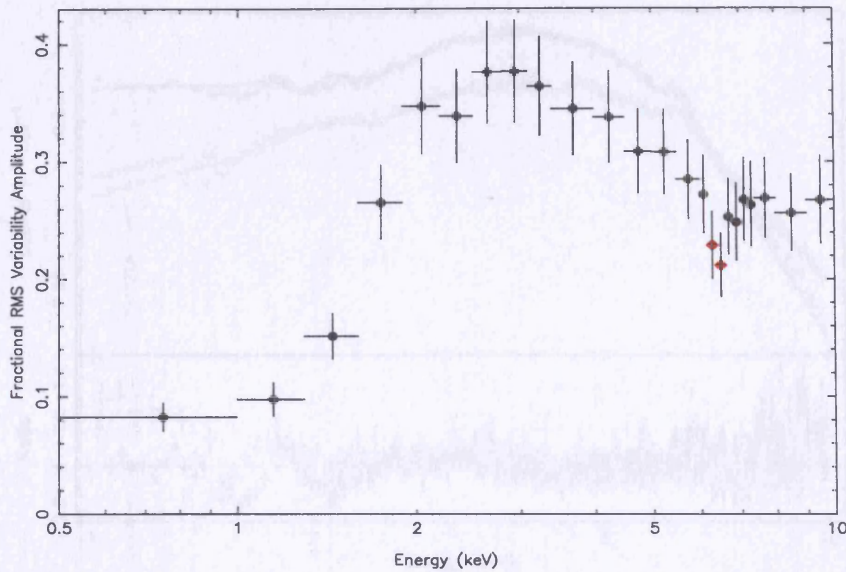


Figure 3.4: The fractional rms variability amplitude as a function of energy calculated for the ASCA long-look observation (SIS data).

as illustrated in the lower panel of Figure 3.3. Appropriate response matrices and ancillary response files were constructed using standard FTOOLS routines and the spectra were again binned to a minimum of 20 counts per bin to allow the use of χ^2 minimisation techniques in the spectral fitting.

Here the goal is to explain the softening of the spectrum as the continuum rises and the subsequent lack of spectral evolution during the continuum decline in terms of photoionization effects. In the context of the template spectral model discussed earlier, the spectral softening implies changes in the ionization of the warm absorber driven by variations in the underlying continuum. However, the persistent soft nature of the spectrum as the underlying continuum flux declines implies considerable complexity in the behaviour of the warm absorber.

The template spectral model was tightly restricted when it was fit to the ASCA data, partly due to the limitations imposed by ASCA's restricted bandpass and partly based on the expected variability properties of the individual components in the model. All but three of the spectral parameters in the template model are fixed at the values derived from the *BeppoSAX* observation (Table 3.1). The remaining parameters are those expected to vary on sufficiently short timescales to be significantly different from the values measured with *BeppoSAX*. The three parameters permitted to vary are the normalization of the hard power-law continuum, A_1 , the normalization of the soft X-ray power-law, A_2 , and the ionization parameter, ξ . The column densities of the warm and cold absorbing components are kept fixed, as is the slope of the underlying continuum and the parameters of the iron $K\alpha$ line. For the Compton reflection component, the actual component flux was fixed at the *BeppoSAX* level (rather than only fixing the scale parameter R).

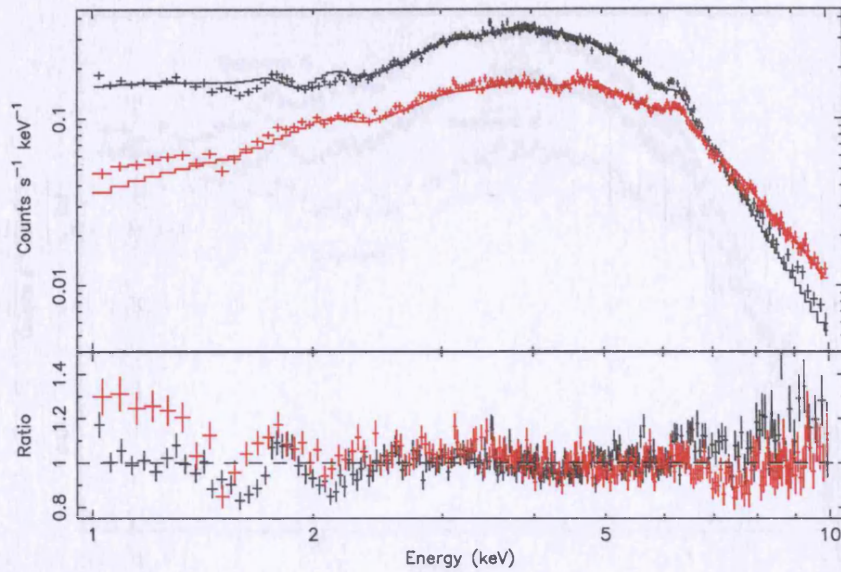


Figure 3.5: A comparison of the best-fitting spectral template model to the combined SIS (black) and GIS-2 (red) spectra from time segment 3 of the long-look observation. *Upper panel:* The count rate spectra and best-fit model. *Lower panel:* The ratio of the data to the best-fit model. Note the discrepancies between the SIS and GIS are most evident below ~ 2 keV and above 8 keV.

Comparing the SIS and GIS instruments

Before proceeding with the *ASCA* spectral analysis the degree of inconsistency between the SIS and GIS instruments was investigated. A comparison of the residuals when the template spectral model is fitted to the SIS and GIS-2 spectral data from time segment 3 is shown in Figure 3.5. As noted earlier these correspond to data extracted with a $1'$ radius source cell in the case of the SIS and a $3'$ radius cell for the GIS. Discrepancies between the two datasets are most evident below 2 keV and above 8 keV. The contamination of the GIS spectrum by the BL Lac accounts for most of the excess flux in the GIS spectra at low energies, in fact the GIS data extracted within a $1'$ radius cell (thereby greatly reducing the BL Lac contribution) agree reasonably well with the SIS data, although this leads to a $\sim 60\%$ reduction of the counts in the spectrum. The problem at the high energy end is similar in character to that reported by Turner *et al.* (2001b) in a comparable *ASCA* long-look observation of the narrow-line Seyfert 1 galaxy Akn 564. Here, a somewhat different approach was taken to that employed by Turner *et al.* (2001b). In the subsequent analysis *only* spectra derived from the SIS data are used. For this study the exclusion of the soft BL Lac flux is a useful advantage that outweighs the spectral uncertainty above 8 keV, since a very tightly constrained model of the hard continuum (via the adopted spectral template) is employed. In any case, the main aim of this analysis is to characterize the spectral changes rather than to determine precise values for spectral parameters. Consistency checks show that very similar results to those reported in Section 3.4.2 for the SIS data are obtained from the GIS data (in fact somewhat better reduced χ^2 are recorded) provided that an extra soft component representative of the BL Lac contribution is included in the spectral modelling.

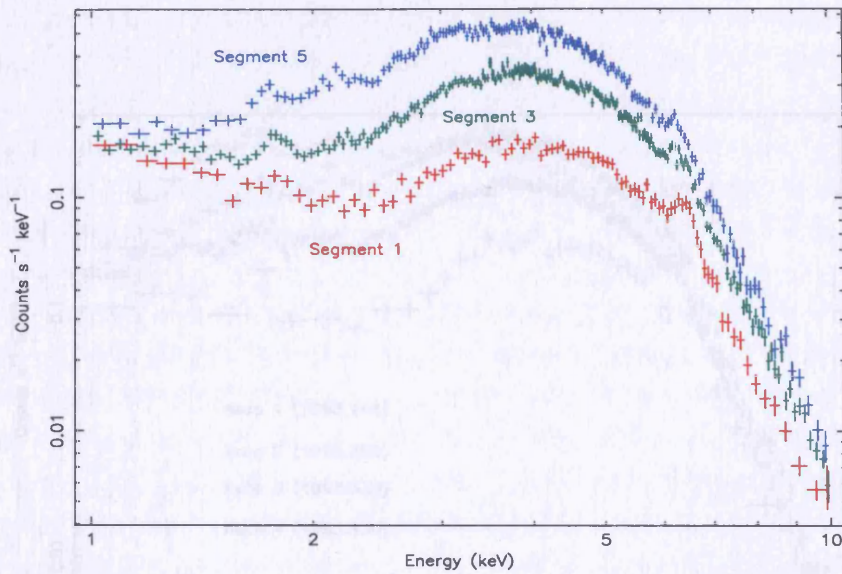


Figure 3.6: The 1-10 keV combined SIS spectrum of NGC 4151 as measured in three time intervals during the *ASCA* long-look observation.

3.4.2 Modelling the spectral variability

Figure 3.6 compares the SIS spectra from time segments 1, 3 and 5 of the long-look observation during which the source count rate in the 1-10 keV band increased by over a factor of 3. These SIS spectra illustrate that the level of the hard continuum rises by a factor of ~ 2 and that it is the marked softening of the spectrum in the 2-6 keV band that accounts for the greater than 2 factor in the count rate increase (*cf.* Figure 3.4).

The results of fitting the constrained spectral template model simultaneously to the spectra from the eight segments of the long-look observation are given in Table 3.2. Overall the model provides a reasonable representation of the eight spectral datasets with a combined χ^2 of 4616 for 3665 d-o-f (degrees of freedom). In this and the following spectra fits the largest residuals are in range 1-2 keV, where the simple power-law model of the soft emission components is clearly a gross over-simplification (Ogle *et al.* 2000). However, the presence of these 1-2 keV residuals, which remain relatively constant (*cf.* Figure 3.4), are very unlikely to influence the interpretation of the observed spectral variations in terms of a variable warm absorber. Interestingly the spectral variation revealed by the long-look data largely encompasses the range of spectral forms exhibited by NGC 4151 in earlier *ASCA* observations (*cf.* Figure 3.6 with Figure 3.7). In fact the template spectral model provides a good description of *all* the available datasets from the previous seven years of observation by both *ASCA* and *BeppoSAX* (not presented here), with a range of ionization parameter values not dissimilar to those derived from the *ASCA* long-look.

If some of the parameter constraints are relaxed then further improvements in the fit to the *ASCA* long-look segments can be obtained. For example, if $E_{K\alpha}$ and $I_{K\alpha}$ are allowed to vary (but with the parameter

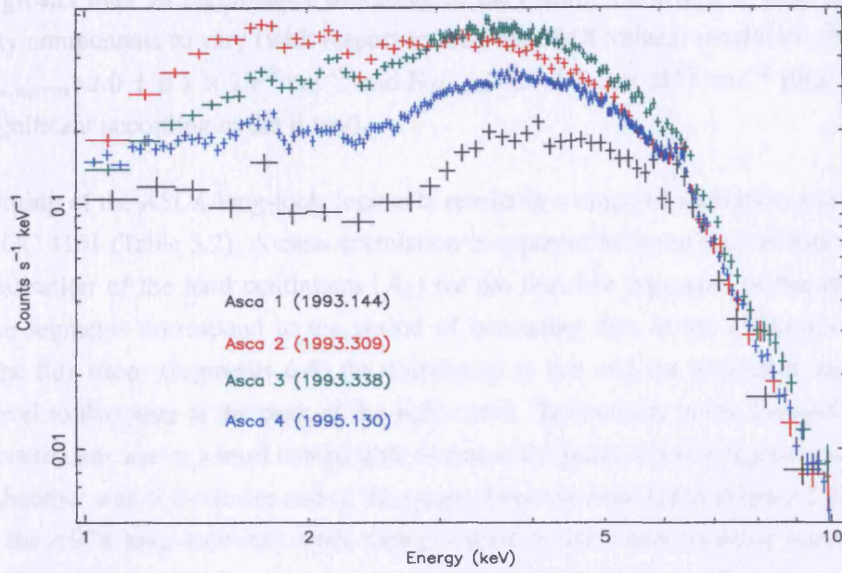


Figure 3.7: The 1-10 keV X-ray spectrum of NGC 4151 as measured by ASCA in the period 1993-1995. These are count rate spectra from the SIS-0 detector only.

Table 3.2: Results from the spectral fitting of the eight time segments of the ASCA long-look data.

Segment	$\log(\xi)$	A_1^a	A_2^b
1	$2.483^{+0.009}_{-0.009}$	$1.99^{+0.04}_{-0.04}$	$0.82^{+0.03}_{-0.03}$
2	$2.513^{+0.007}_{-0.005}$	$2.58^{+0.04}_{-0.04}$	$0.80^{+0.02}_{-0.02}$
3	$2.554^{+0.006}_{-0.002}$	$3.79^{+0.03}_{-0.05}$	$0.85^{+0.02}_{-0.03}$
4	$2.615^{+0.004}_{-0.013}$	$4.59^{+0.10}_{-0.01}$	$0.85^{+0.07}_{-0.02}$
5	$2.644^{+0.001}_{-0.011}$	$5.25^{+0.08}_{-0.01}$	$0.87^{+0.06}_{-0.01}$
6	$2.636^{+0.003}_{-0.009}$	$3.50^{+0.05}_{-0.03}$	$0.88^{+0.03}_{-0.01}$
7	$2.630^{+0.004}_{-0.009}$	$2.42^{+0.03}_{-0.02}$	$0.93^{+0.03}_{-0.03}$
8	$2.643^{+0.006}_{-0.008}$	$2.51^{+0.04}_{-0.03}$	$0.94^{+0.04}_{-0.04}$

^a 10^{-2} photon $\text{keV}^{-1} \text{cm}^{-2} \text{s}^{-1}$ at 1 keV

^b 10^{-3} photon $\text{keV}^{-1} \text{cm}^{-2} \text{s}^{-1}$ at 1 keV

value tied across the eight spectral datasets), then a $\chi^2=4552$ for 3663 d-o-f is obtained, with the best fit values of $E_{K\alpha}=6.395 \pm 0.012$ keV and $I_{K\alpha}=2.2^{+0.2}_{-0.3} \times 10^{-4}$ photon $\text{cm}^{-2} \text{s}^{-1}$ (this improvement is significant at greater than 5σ significance according to the F-test). As a further step, allowing the two column density components to vary (with respect to the *BeppoSAX* values) results in $\chi^2=4295$ for 3661 d-o-f with $N_{H,warm}=2.0 \pm 0.1 \times 10^{23} \text{ cm}^{-2}$ and $N_{H,cold}=4.6 \pm 0.2 \times 10^{22} \text{ cm}^{-2}$ (this improvement is also highly significant according to the F-test).

The spectral fitting of the *ASCA* long-look segments results in a range of ionization states for the warm absorber in NGC 4151 (Table 3.2). A clear correlation is apparent between the ionization parameter (ξ) and the normalisation of the hard continuum (A_1) for the first five segments of the observation (Figure 3.8) [these segments correspond to the period of increasing flux in the light-curve (Figure 3.3)]. However as the flux drops (segments 6-8) the correlation is lost and the ionization state remains at a comparable level to that seen at the peak of the light-curve. In contrast, in the *BeppoSAX* observation, although the continuum was at a level comparable to that at the peak of *ASCA* light-curve, the ionization of the warm absorber was at the lower end of the range observed with *ASCA* (Figure 3.8). The observed correlation in the *ASCA* long-look data lends strong support to the warm absorber interpretation for the observed absorbing column. Furthermore, I argue in Section 3.5.1 that the lack of a sustained correlation between ionization level and the continuum flux, is not inconsistent with the warm absorber description of the absorbing column.

The normalization of the soft power-law component, A_2 , varies by $\sim 15\%$ during the *ASCA* long-look observation. Bearing in mind that much of the soft emission in NGC 4151 originates in the spatially extended component recently imaged by *Chandra*, (Ogle *et al.* 2000; Yang, Wilson & Ferruit 2001), these results would suggest that there may be some leakage of the hard continuum flux through the absorber down to ~ 1 keV (Figure 3.4), whereas in the current spectral modelling the variability cut-off is nearer to 2 keV. Since the complex absorption in NGC 4151 is likely to arise from gas exhibiting a range of ionization parameters, our two component (cold + warm gas) model must, at best, represent only a coarse approximation to the real situation. A second possible explanation for the observed variability is that a small fraction of the continuum flux is scattered into our line-of-sight from material in the vicinity of the broad line region. The scattered continuum flux would avoid the absorption seen by the rest of the nuclear flux. The contribution of scattered continuum flux to the soft X-ray spectrum of NGC 4151 is discussed in more detail in Chapter 6.

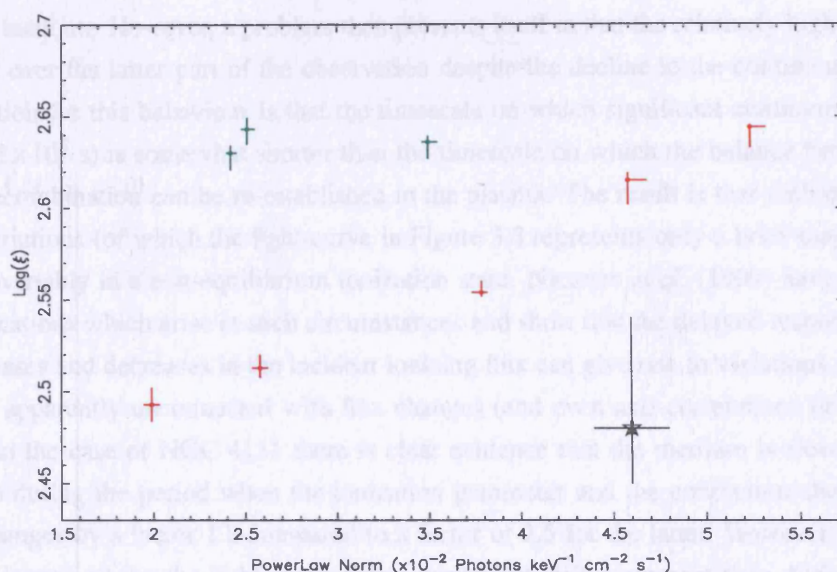


Figure 3.8: Correlation between ionization parameter (ξ) and the normalization of the hard power-law continuum for the eight segments of the *ASCA* long-look observation. The red points mark the segments where the light-curve is rising, the green points mark the segments where the light-curve is falling. The point marked by the star symbol is from the *BeppoSAX* observation; the error bar is larger in this case due to the additional free parameters in the spectral fitting.

3.5 The results from *BeppoSAX* and *ASCA*

3.5.1 The physical state of the warm absorber

One of the major advantages of the warm absorber description of the complex absorption in NGC 4151 is that it is based on a physical model that is, in principle, readily testable. For example, given sufficient spectral resolution, sensitivity and dynamic range, the true ionization state of the warm gas can be determined directly from the absorption edges present in the X-ray spectrum. A further key diagnostic, somewhat more in tune with current measurement capabilities in the case of heavily absorbed sources such as NGC 4151, is that the ionization state of the warm gas should track the intensity of the ionizing radiation field, albeit in a complex fashion (Nicastro *et al.* 1999). In contrast the popular partial covering (or dual absorber) models are based on rather arbitrary, constructed geometries that are very difficult to verify observationally.

Previous studies of NGC 4151 have failed to demonstrate in an unambiguous fashion that the absorbing medium in NGC 4151 does respond to changes in the level of the incident hard continuum (Yaqoob, Warwick & Pounds 1989; Fiore, Perola & Romano 1990; Warwick *et al.* 1996; Piro *et al.* 2002). However, the *ASCA* long-look observation provides an excellent opportunity to study the response of the absorber to continuum changes. The correlation between ionization parameter and the level of the hard continuum apparent over the rising part of the light-curve would appear to be the signature of a partially

photoionized medium. However, a problem then presents itself in that the relatively high ionization state is maintained over the latter part of the observation despite the decline in the continuum level. A possible explanation for this behaviour is that the timescale on which significant continuum variations are occurring ($\sim 3 \times 10^5$ s) is somewhat shorter than the timescale on which the balance between photoionization and recombination can be re-established in the plasma. The result is that with quasi-continuous continuum variations (of which the light-curve in Figure 3.3 represents only a brief snapshot) the warm absorber is invariably in a non-equilibrium ionization state. Nicastro *et al.* (1999) have discussed some of the complications which arise in such circumstances and show that the delayed response of a medium to sharp increases and decreases in the incident ionizing flux can give rise to variations in the ionization state that are apparently unconnected with flux changes (and even anti-correlations of ionization level with flux!). In the case of NGC 4151 there is clear evidence that the medium is slow to respond; for example even during the period when the ionization parameter and the continuum show a correlation, the former changes by a factor 1.8 compared to a factor of 2.5 for the latter. However, the fact that the degree of ionization tracks the light-curve better during the rising segment than during the decline is consistent with the fact that $t_{ion} \propto L_{ion}^{-1}$, as is evident from Figure 1 of Nicastro *et al.* (1999).

The parameter values for the warm absorber in NGC 4151 are similar to one of the standard cases considered by Krolik & Kriss (2001) [although the assumed form of underlying continuum is somewhat modified with respect to the version in Krolik & Kriss (1995), which has been adopted in the present work]. Taking $\xi=300$ and $L_{ion}=10^{44}$ erg s $^{-1}$ as representative values for the warm absorber in NGC 4151 and taking the distance of the warm medium from the continuum source to be ~ 1 pc, then the inferred gas density is $n \approx 4 \times 10^4$ cm $^{-3}$. Table 1 in Krolik & Kriss (2001) gives the corresponding equilibration timescales for selected ions in such a plasma. The warm absorber cut-off is best measured between 2-6 keV, where absorption edges due to the hydrogen- and helium-like ions of Mg, Si, S, Ar and Ca will be of importance (although not individually resolvable in the *ASCA* data). For these ions the relevant equilibration timescales are typically between $1-8 \times 10^6$ s. Additionally, the measured column density for the warm absorber in NGC 4151 of $\sim 2 \times 10^{23}$ cm $^{-2}$ implies $r_{max} \sim 0.5$ pc (Krolik & Kriss 2001), which in turn (since $t_{ion} \propto r^2$), requires a factor 4 reduction in the equilibration timescales quoted by Krolik & Kriss. Nevertheless it is still true that the variability timescale in NGC 4151 is short enough for the warm absorber to be continuously out of ionization equilibrium as required. Since different ions reach their equilibrium abundance, for a given flux of ionizing radiation, on different timescales, the detailed form of the absorption cut-off will depend on the luminosity history of the source stretching back over a period equal to the longest relevant equilibration timescale, which in NGC 4151 will be $\sim 10^7$ s.

3.5.2 The properties of the iron $K\alpha$ line

In this work the iron $K\alpha$ emission is modelled in a very simple fashion, namely as a single narrow line at an energy appropriate to cold (*i.e.* neutral or low ionization) material. In the long-look *ASCA* observation, the measured line flux was $2.2_{-0.3}^{+0.2} \times 10^{-4}$ photons cm $^{-2}$ s $^{-1}$, with no strong evidence for any variations

in either the line intensity or in the line profile during the observation. The *BeppoSAX* observation measures a somewhat higher flux (at the 3σ level) suggesting the possibility of line flux variations. The lack of significant variability on timescales of about a year suggests that the origin of this narrow component is in a medium located well outside of the immediate surroundings of the nuclear source (*i.e.* not in a putative accretion disk), but does not exclude the region occupied by the warm absorber. The predicted range of iron ionization states in the warm medium is FeXVI-FeXXI with the associated $K\alpha$ line emission ranging in energy from 6.4-6.6 keV. Since the measured line energy excludes much of this range, it is likely that the bulk of the line equivalent width (which ranges from 82-195 eV during the eight segments of the observation, depending on the continuum level in each case) derives from less strongly photoionized material located further from the nucleus than the warm medium identified here. The cold absorber in this model cannot realistically account for the observed iron $K\alpha$ flux, since this would require the cold absorbing material to subtend a full 4π steradians as viewed from the central source and to have an iron abundance a factor ~ 3 higher than solar.

In contrast with previous claims suggesting a complex broad iron line structure in NGC 4151 (Yaqoob *et al.* 1995; Wang, Zhou & Wang 1999; Wang, Wang & Zhou 2001; Yaqoob *et al.* 2001), no compelling evidence to include a relativistically broadened line is present in any of the modelling undertaken in this work (the best fit intrinsic line width of the “narrow” line in the *ASCA* data was 110 ± 20 eV but this may over estimate the true line width given the SIS calibration uncertainties; Section 3.4.1). The lack of any variability in the line profile during the observation contrasts with earlier claims of line profile variability in NGC 4151 on 10^4 s timescales Wang, Wang & Zhou (2001).

Clearly a very extended broad line profile is easily confused with a continuum form that includes a non-negligible contribution from Compton reflection and is modified by a complex absorption. If this continuum is mis-modelled then the complex variable nature of the underlying continuum and the absorption may easily manifest itself as apparent variability in the broad line profile. The details of the iron $K\alpha$ line properties in NGC 4151 are discussed considerably more extensively in Section 3.8, utilizing newly acquired data from *XMM-Newton*.

3.5.3 The impact of Compton reflection

The presence of Compton reflection, the form of which is shown in Figure 3.2, has a significant impact on the X-ray spectrum of NGC 4151 from 4 keV right out to 50-60 keV. The parameters of the Compton reflection continuum in NGC 4151 are well constrained by a combination of the good signal to noise, large bandpass, spectra from *BeppoSAX*, particularly significant is the energy range encompassed by the PDS instrument. Despite the limited statistics afforded by the PDS instrument, the PDS data are sensitive to the curvature of the spectrum introduced by a Compton reflection component at energies >10 keV (Risaliti 2002). A model including Compton reflection provides a significantly improved fit (at $>3\sigma$) to the PDS spectrum in comparison to a simple power-law model. The origin for the neutral Compton

reflection continuum lies in Compton-thick material possibly associated with the putative molecular torus and, in moderate to heavily absorbed Seyferts (Seyfert 1.5's-Seyferts 2's), this component is expected to be a strong contribution [and possibly even the dominant contribution in some sources, *e.g.* Mrk 3 (Chapter 4); NGC 4945 (Chapter 5)] to the hard X-ray spectrum (Risaliti 2002).

The most noticeable effects of Compton reflection on the form of the observed X-ray spectrum are a significant hardening of the spectrum, particularly at high energies, the introduction of a significant change of the continuum shape in the 4-10 keV range and the addition of a strong absorption edge at ~ 7.1 keV associated with neutral iron. Arguably the most significant of these effects is the impact that the reflection continuum has on the 4-10 keV X-ray spectrum of NGC 4151. The curvature and variability in this range were previously interpreted as evidence for a relativistically broadened iron $K\alpha$ line emission however, the model including a modest Compton reflection component accurately models this region of the X-ray spectrum. The implication here is that mis-modelling (or indeed the absence of) the reflection continuum can result in the spurious detection of a feature that appears to be consistent with a relativistically broadened iron $K\alpha$ line. Such spurious detections can be avoided with the use of large bandpass data where the reflection component can be well constrained. I note that while reflection strongly impacts on the detection of relativistically broadened iron $K\alpha$ lines in more absorbed Seyferts, in Seyfert 1's the reflection continuum is, relative to the direct continuum, a smaller contribution to the X-ray spectrum and, hence, relativistically broadened iron $K\alpha$ lines detected in these objects (*e.g.* MCG-6-30-15; Fabian *et al.* 2002) are less likely to be spurious detections.

3.5.4 The spectral index versus flux correlation

Previous observations of NGC 4151 with both *EXOSAT* and *Ginga* revealed an apparent correlation between the spectral index measured in the 2-10 keV band and the level of the underlying continuum (Perola *et al.* 1986; Yaqoob & Warwick 1991; Yaqoob *et al.* 1993). Figure 3.9 shows a compilation of measurements from *EXOSAT* and *Ginga* (taken from Yaqoob *et al.* 1993) which suggests that as the source brightens the photon index steepens, from $\Gamma \sim 1.35$ to $\Gamma \sim 1.7$, at which point the correlation saturates. Yaqoob *et al.* (1993) also note that the spectral slope changes occur on roughly the same timescale as the flux variations. However, a perplexing aspect of the spectral index flux correlation observed in the 2-10 keV bandpass is that the effect is not mirrored in the hard X-ray/soft γ -ray regime (Johnson *et al.* 1997; Piro *et al.* 2002).

An underlying assumption of the template spectral model adopted in this chapter is that the spectral index of the hard power-law continuum in NGC 4151 remains constant (at a value $\Gamma \approx 1.65$), as the continuum flux changes, in apparent contradiction to the correlation noted above. Testing this assumption against the *ASCA* observation demonstrates that the *ASCA* data are broadly consistent with the assumed value of $\Gamma = 1.65$. However the parameter values are poorly constrained due to the very limited effective bandpass, and the fact that the values of Γ derived are very dependent on the exact details of the applied spectral

model.

The possibility exists that the spectral index versus relation may actually be a misinterpretation of the softening of the NGC 4151 spectrum as the source flux increases, bearing in mind that the reported correlation was established using both proportional counter data with limited spectral resolution and a simplistic spectral model (a power-law continuum model, modified by a heavy cold absorbing column). To test this possibility the template spectral model and an appropriate *Ginga* response were used to simulate a set of five *Ginga* spectra using XSPEC. In this simulation, the normalization of the hard power-law continuum was increased in steps from 1 to 10×10^{-2} photons $\text{cm}^{-2} \text{s}^{-1}$, but with all the other parameter values, (including the ionization parameter and the *flux* in the Compton reflection component) frozen at the values obtained from the *BeppoSAX* spectral fitting. The simulated 3.5-20 keV *Ginga* spectra were then each fitted with the simple absorbed power-law model used to fit the previous *Ginga* and *EXOSAT* data (Yaqoob & Warwick 1991; Yaqoob *et al.* 1993). The best-fit photon spectral index, from this simple model, was measured. The result was a spectral index versus 2-10 keV flux correlation closely matching the reported correlation (Figure 3.9). Since the simulation did not include any of the complications associated with the varying ionization parameter of the warm absorber, it follows that the observed softness vs flux correlation can be induced solely as a result of the presence of a non-varying, spectrally-hard, Compton reflection component. Clearly, in this scenario, as the direct continuum brightens, the *relative* contribution from Compton reflection declines and the overall spectrum softens until eventually the measured spectral index saturates at the value pertaining to the underlying continuum.

3.6 Conclusions from *BeppoSAX* and *ASCA*

There has been much debate as to whether NGC 4151 is simply a very bright, nearby representative of the broad class of galaxies harbouring luminous Seyfert nuclei or a unique object (Ulrich 2000). In the X-ray band this uncertainty is due, in large measure, to the heavy, complex and variable absorption which characterizes the 2-6 keV spectrum of NGC 4151 but which is not observed in the great majority of well-studied Seyfert galaxies (Mrk 6 is arguably the best known example of a NGC 4151 analogue, Feldmeier *et al.* 1999).

This work has so far presented a detailed analysis of two archival observations of NGC 4151, one from *BeppoSAX* the other from *ASCA*, which test the hypothesis that the complex absorption is due to a combination of warm and cold gas distributed along the line-of-sight to the active Seyfert nucleus in this source. In this model, the complex spectral variability exhibited by NGC 4151 over timescales longer than a few days is the product of changes in the source, driven predominantly by the level of the underlying continuum. This relatively simple model provides a good description of the two datasets in question and, in fact, gives a reasonable fit to all of the *ASCA* and *BeppoSAX* observations from the past seven years. The key finding is that the warm absorber corresponds to a relatively low density ($\sim 10^{4-5}$

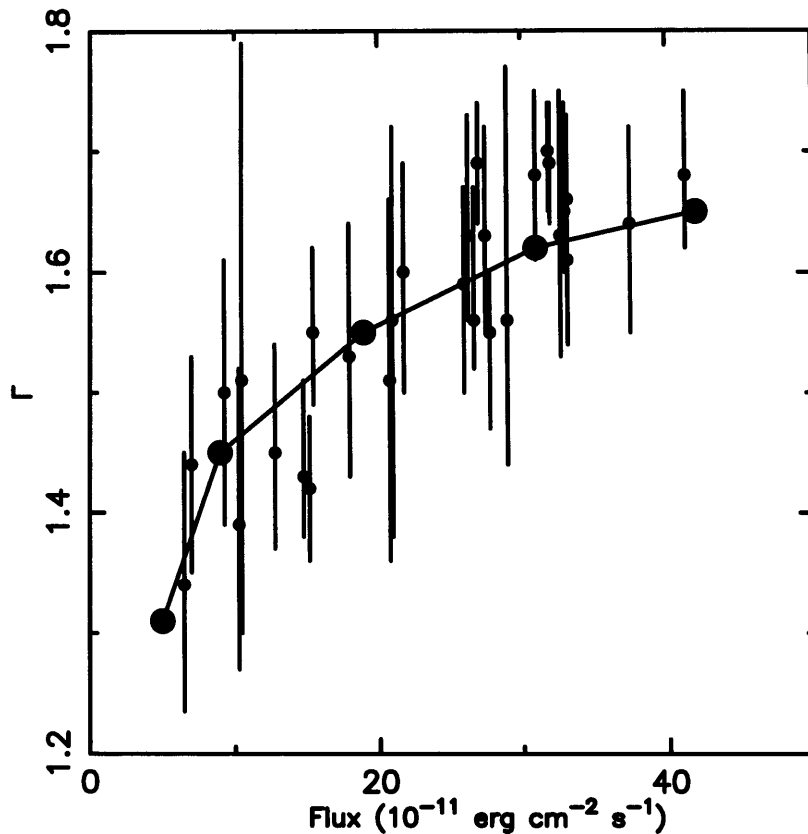


Figure 3.9: Measurements of the spectral photon index versus the absorption-corrected 2-10 keV flux from *EXOSAT* and *Ginga* observations, taken from Figure 2 of Yaqoob *et al.* (1993). The solid curve represents the results of a set of simulations in which complex absorption and a constant Compton reflection component was included along with a power-law continuum with a variable normalization but fixed slope (*i.e.* $\Gamma=1.65$). See Section 3.5.4 for further details.

cm^{-3}) gas, with a column density of $\sim 2 \times 10^{23} \text{ cm}^{-2}$ and with ionization parameter in the range $\log(\xi) \approx 2.4-2.7$. Since the equilibration timescale for the dominant ions in the gas is of the same order or longer than the timescale of the continuum variability, the warm component is invariably observed in a non-equilibrium ionization state. Non-equilibrium conditions help explain why past studies based on relatively short observations spaced by weeks, months or years have failed to identify the consistent signature of a warm absorber in this source.

In a recent paper, Krolik & Kriss (2001) discuss how evaporation from the inner edge of the obscuring torus in an AGN can give rise to an inhomogeneous photoionized wind in which a broad range of temperatures coexist in equilibrium. Krolik & Kriss go on to suggest that this wind is the origin of the highly ionized, warm absorbers seen in over half of type 1 Seyfert galaxies. For most Seyfert 1 galaxies the properties of the warm absorber are inferred from the O VII and O VIII absorption edges, whereas in NGC 4151 the combination of warm and cold absorbers gives rise to a sharp spectral cut-off below ~ 2 keV, thus eliminating these features. Nevertheless, as noted earlier, the inferred properties of the warm component in NGC 4151 are not too far removed from one of the standard cases detailed in Krolik &

Kriss (2001). It is therefore reasonable to hypothesise that the warm absorber in NGC 4151 originates in such a multi-temperature wind, but that the unusually complex character of the absorption is due to a line-of-sight which grazes the top edge of the obscuring torus so as to intercept a substantial column of *both* the warm (wind) and cold (torus) components. In essence, in terms of its X-ray absorption properties, NGC 4151 appears to be intermediate between the Seyfert galaxies in which the absorption, if present, is predominantly due to the Krolik & Kriss's multi-temperature wind (type 1 objects) and those where the cooler material of the obscuring torus dominates (type 2 objects). Recent observations of NGC 3516, another well-known Seyfert 1.5 galaxy, have also revealed that the variability of the X-ray absorption in this source is the result of an ionized absorber that responds in a complex fashion to changes in the underlying ionizing continuum (Kraemer *et al.* 2002). This work also suggests that (i) the reported hardening of the spectrum of NGC 4151 as the continuum level falls may be simply due to the presence of an underlying (hard and relatively constant) Compton reflection component and (ii) there is no compelling evidence for a relativistically broadened iron $K\alpha$ line in NGC 4151, again, due to the presence of the underlying Compton reflection.

The focus of this chapter now shifts to the analysis of *XMM-Newton* observations of NGC 4151. With greatly increased collecting area and spectral resolution over the 2-10 keV range, the *XMM-Newton* data is expected to provide a much more stringent test of the validity of the model for NGC 4151 developed from the *ASCA* and *BeppoSAX* analysis. The *XMM-Newton* data is also likely to reveal subtleties in the spectral details that were not evident from the previous data.

3.7 The *XMM-Newton* observations

NGC 4151 was observed by *XMM-Newton* three times during the period December 21-23, 2000 (orbit 190). In all three observations the EPIC MOS and PN CCD cameras (Turner *et al.* 2001a; Strüder *et al.* 2001) were operated with the medium filter in place. A brief summary of the *XMM-Newton* mission and instrumentation is given in Chapter 2 (for a more detailed discussion see Jansen *et al.* (2001) and references therein). The first observation (~ 33 ks) was carried out with both CCD systems in Small Window Mode (SWM), whereas the remaining two observations (~ 23 ks and ~ 63 ks respectively) employed Full Window Mode (FWM). The events recorded in FWM were screened with the *XMM-Newton* Science Analysis Software (SAS) version 5.2 to remove known hot pixels and other data flagged as bad (the latest SAS release, now SAS v5.3, was not available at this time). The SWM observations were processed with a local developers version of the SAS, which included a patch with up-to-date corrections for the PN charge transfer inefficiency (CTI), prior to the public release of these corrections in SAS v5.3. The data were processed using the latest CCD gain values and only X-ray events corresponding to patterns 0-12 in the MOS cameras and 0-4 in the PN camera were accepted. An examination of the temporal variation in count rate from the full available field (but excluding the bulk of the NGC 4151 contribution) in all three observations revealed a single background flaring event during the first observation, which

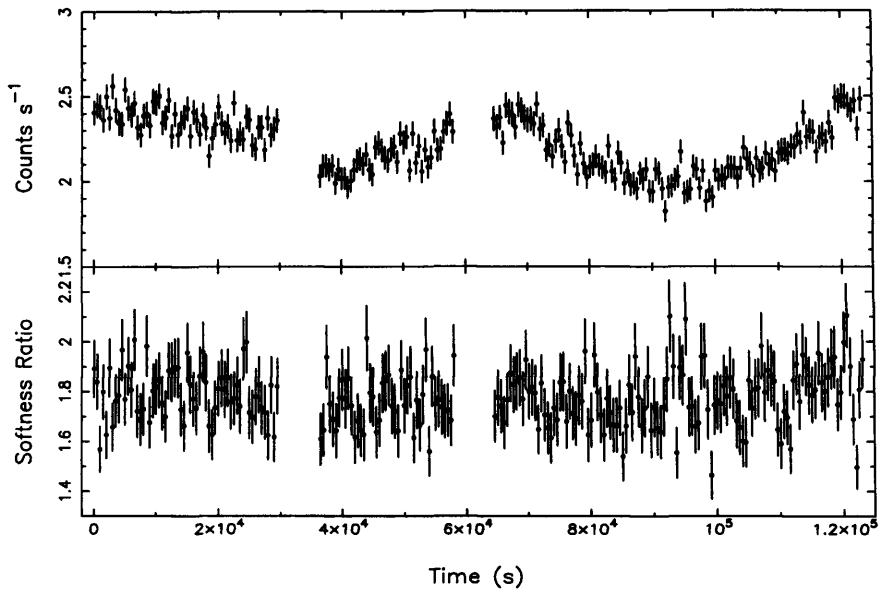


Figure 3.10: *Upper Panel:* The 2-10 keV light-curve from the co-added *XMM-Newton* EPIC MOS detectors. The light-curve is binned to a resolution of 500 seconds and covers the three separate observations (indicated by the data gaps). *Lower Panel:* The variation of the 2-5 keV/5-10 keV softness ratio during the observation.

was screened from subsequent analysis. The resulting total effective exposure times were 110 ks and 91 ks for the MOS and PN instruments respectively.

An investigation into the impact of pile-up on the observations showed that the effect was negligible in almost all cases, largely due to the low flux level of NGC 4151 during the observation period. The exception to this is the FWM MOS observation, which shows marginal pile-up above 8 keV. The best-fit spectral parameters and χ^2 values quoted in this paper are for spectral fits in which the MOS FWM data above 8 keV have been excluded.

3.7.1 The light-curve

A source light-curve was extracted for the MOS cameras from each individual, screened observation. The source counts were taken from within a $100'' \times 100''$ box for the SWM case and a $2'$ radius circle for the FWM observations. Background subtraction was not applied since the background contributes no more than a few percent to the total signal.

The light-curve (Figure 3.10, *Upper Panel*) shows slow drifts in the X-ray flux of NGC 4151 on timescales longer than $\sim 10^4$ s, behaviour which is very characteristic of this source (Yaqoob & Warwick 1991; Yaqoob *et al.* 1993). The largest flux variation seen was an increase of $\sim 25\%$ over the last $\sim 2 \times 10^4$ s of the observation. The previous analysis of *BeppoSAX* and *ASCA* observations of NGC 4151 revealed

complex spectral changes associated with long-timescale flux variations (Section 3.4) . However, the 2-5 keV/5-10 keV softness ratio measured during the *XMM-Newton* observations (Figure 3.10, *Lower Panel*) remains fairly constant with just a hint of spectral softening towards the end of the observation, correlated with the overall flux increase.

3.7.2 The spectral analysis

The lack of significant spectral variability over the course of the three observations (Figure 3.10 *Lower Panel*) allows the following spectral analysis to utilise the spectrum averaged over all the observations without needing to consider the complex spectral variability highlighted by the analysis of the *ASCA* long-look observations. The background-subtracted spectrum of NGC 4151 from all the EPIC instruments, averaged over the three *XMM-Newton* observations, is used for this analysis. For the MOS spectra, source counts were extracted from the same source regions that were employed for the light-curves. In the FWM observations, the background was taken from a region offset from the source but on the same chip (MOS 1 and 2 cameras). This same background was also used to correct the SWM observation. For all the MOS observations the total background amounted to less than 3% of the source plus background count rate. For the PN camera a 2' radius source cell was used for the FWM observations with an offset background region located on the same chip as the source. For the SWM observation the source spectrum was derived from a 4'×2' box and the background from a similar size region offset from the source but on the same chip. In this latter case the contamination of the background by the wings of the source response resulted in a background subtraction amounting to ~8% of the source plus background count rate. The loss of source flux in the various cases is accounted for both in the spectral fitting and in the quoted fluxes. For convenience the spectra from the two FWM observations were co-added to produce a single source spectrum and a single background spectrum for each of the three instruments. In keeping with the previous analysis, the resulting spectra were binned to a minimum of 20 counts per spectral channel in order to apply χ^2 minimisation techniques. Here the focus is on the hard X-ray spectrum of NGC 4151 and hence the following analysis is restricted to the 2.5-12 keV range. This avoids any contamination from the soft X-ray emission line spectrum in NGC 4151. The preliminary analysis of the complex soft X-ray spectrum of NGC 4151, based on the *XMM-Newton* RGS data (along with a brief comparison of the RGS spectrum with the EPIC data), is presented in Chapter 6.

The spectral template model, developed to model the previous *BeppoSAX* and *ASCA* observations, is adopted for the analysis of the hard X-ray *XMM-Newton* EPIC spectra. The model details are described in Section 3.3. However a single modification has been made for the analysis of the *XMM-Newton* spectra, namely the normalisation of the Compton reflection component has been fixed at the same value as the normalisation of the directly observed power-law continuum (the reflection scaling parameter, R, is left as a free parameter in the model fits).

To recap, the spectral model requires a total of just six free parameters relating to the continuum and

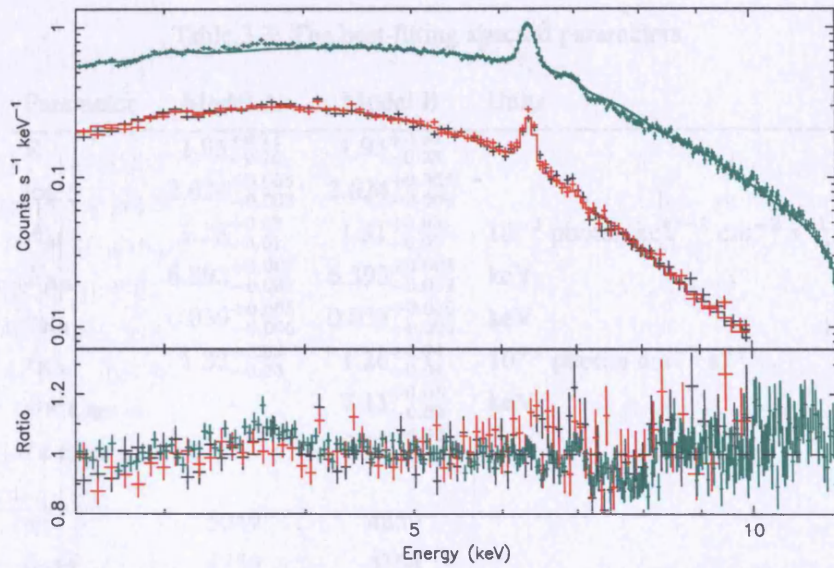


Figure 3.11: *Upper Panel:* The 2.5-12 keV X-ray spectra measured by the EPIC instruments on *XMM-Newton*. The MOS data, shown here in black (MOS 1) and red (MOS 2), are from the SWM observation. The PN data, shown here in green, are from the FWM observation. In each case, the solid lines show the best-fit of the spectral template model (Table 3.3; Model A). *Lower Panel:* The ratio of the data to the model prediction.

reflection normalisations, the iron $K\alpha$ line properties and the ionization state of the warm absorbing column. In the simultaneous fitting of the SWM and the co-added, FWM EPIC spectra for each detector (MOS 1, MOS 2, PN), I also employ five scaling factors to allow for the relative instrument calibrations. The two MOS instruments agree to better than 3% and the PN is within 5% of both the MOS instruments.

Although the resulting best-fit was formally unacceptable, with $\chi^2=5193$ for 4756 degrees of freedom, the remaining residuals were largely at the few percent level, which is close to the limit of the current calibration uncertainty. In fact including a 1.5% systematic error to allow for the calibration uncertainties (S. Sembay, private communication) reduces the χ^2 to 5049. By way of illustration, Figure 3.11 shows three of the six available EPIC spectra (for simplicity) along with the overall model and the fitting residuals. The corresponding best-fit parameter values are listed in Table 3.3 as Model A. Again, the quoted errors are at the 90% confidence level as defined by a $\Delta\chi^2=2.71$ criterion (*i.e.*, assuming one interesting parameter).

Remarkably, the spectral template model provides an excellent description of the *XMM-Newton* spectra with only minor adjustments to a limited number of free parameters. Given the very high quality of the EPIC spectra (the PN and the combined MOS 1/2 spectra contain in excess of 340,000 and 240,000 counts in the hard X-ray band, respectively!), it would be surprising if further subtle spectral features had not to emerge. For example, inspection of the data/model residuals (see Figure 3.11, *Lower Panel*) suggests a systematic deficit of counts between 7 and 8 keV. This is interpreted as a need for extra

Table 3.3: The best-fitting spectral parameters

Parameter	Model A	Model B	Units
R	$1.95^{+0.11}_{-0.25}$	$1.93^{+0.14}_{-0.23}$	
$\log \xi$	$2.634^{+0.003}_{-0.008}$	$2.624^{+0.004}_{-0.006}$	
A_{pl}	$1.28^{+0.03}_{-0.01}$	$1.31^{+0.03}_{-0.02}$	10^{-2} photon keV $^{-1}$ cm $^{-2}$ s $^{-1}$
$E_{\text{K}\alpha}$	$6.393^{+0.003}_{-0.002}$	$6.393^{+0.003}_{-0.002}$	keV
$\sigma_{\text{K}\alpha}$	$0.039^{+0.005}_{-0.006}$	$0.033^{+0.006}_{-0.005}$	keV
$I_{\text{K}\alpha}$	$1.32^{+0.03}_{-0.03}$	$1.26^{+0.04}_{-0.04}$	10^{-4} photon cm $^{-2}$ s $^{-1}$
$E_{\text{K,Edge}}$	-	$7.11^{+0.01}_{-0.00}$	keV
$\tau_{\text{K,Edge}}$	-	$0.12^{+0.02}_{-0.02}$	
χ^2	5049	4859	
d-o-f	4756	4754	

absorption over and above the current model prediction, which in terms of the spectral modelling requires the addition of an extra absorption edge, with the edge energy and optical depth as free parameters. Also at this stage a contribution from iron $\text{K}\beta$ emission is included; for this purpose a Gaussian line was added at a rest frame energy of 7.058 keV, with the same intrinsic width as the iron $\text{K}\alpha$ line and at 10% of the $\text{K}\alpha$ intensity (*i.e.* the appropriate branching ratio).

These modifications to the model result in a significantly improved fit ($\chi^2=4859$ for 4754 d.o.f). The model fit to the data is shown in Figure 3.12 and the best-fitting parameter values for this revised model are listed as Model B in Table 3.3. The null-hypothesis probability of this latter model (0.14) indicates that this is a reasonable representation of the spectral data to within the limits of the instrument calibration.

3.8 Details of the *XMM-Newton* spectrum

On the basis of the models in Table 3.3, the absorption corrected flux of NGC 4151 measured by *XMM-Newton* in December 21-23, 2000 was 5.8×10^{-11} erg s $^{-1}$ (2-10 keV). This is a very faint flux level for NGC 4151 as judged against previous extensive X-ray monitoring by missions such as *EXOSAT*, *Ginga*, *BeppoSAX* and *ASCA* (Yaqoob *et al.* 1993; Piro *et al.* 2002; Schurch & Warwick 2002). A number of points follow from a detailed comparison of the parameter values in Table 3.3 (Model B) with those quoted in Tables 3.1 & 3.2. For example, the ionization parameter pertaining to the warm absorbing medium remains high ($\log \xi=2.62$) despite the decline in the level of the hard power-law continuum by almost a factor 4 compared with the January 1999 *BeppoSAX* observation (Table 3.1). This may be further evidence for long recombination timescales in the warm absorber. The value of the ioniza-

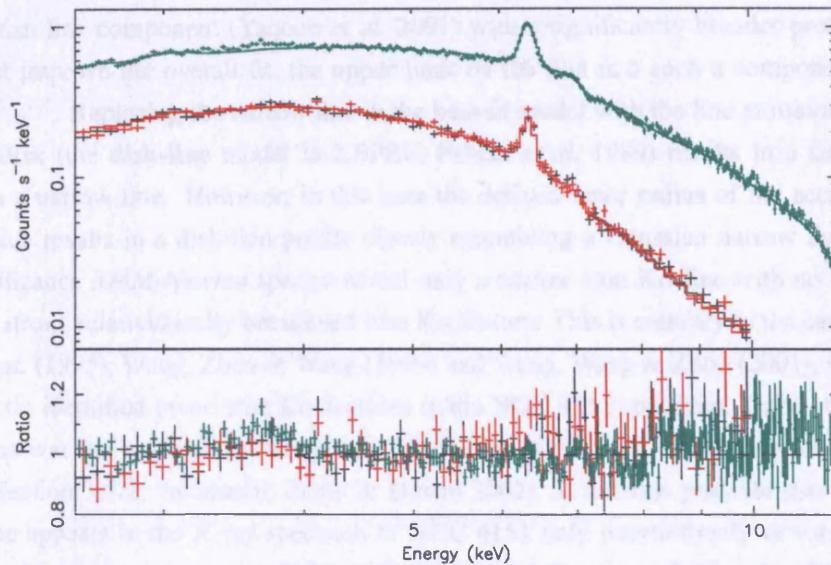


Figure 3.12: *Upper Panel:* The 2.5-12 keV X-ray spectra measured by the EPIC instruments on *XMM-Newton*. The MOS data, shown here in black (MOS 1) and red (MOS 2), are from the SWM observation. The PN data, shown here in green, are from the FWM observation. In each case, the solid line shows the best-fitting spectral model (Table 3.3; Model B). *Lower Panel:* The ratio of the data to the model prediction.

tion parameter derived from the *XMM-Newton* observation falls at the high end of the range recorded in the *ASCA* long-look observation ($\xi=2.48-2.65$; Table 3.2), although in the latter case the underlying continuum was a factor of 1.5-4 brighter. The rather high value of the reflection parameter ($R \approx 2$) derived from the *XMM-Newton* spectra, in comparison to that derived from the previous *BeppoSAX* or *ASCA* data, might be explained by the continuum source having recently and/or temporarily entered a low-flux period. The Compton reflection component however remains high due to the time lag inherent for a component originating in material relatively distant from the central source of ionizing radiation. For example, the bulk of the Compton reflection may be produced from the far side of a putative molecular torus in NGC 4151, in which case the response time would be measured in years. The *measured flux* in the Compton reflection signal is a factor of $1.5^{+1.2}_{-0.6}$ times higher than observed in the January 1999 *BeppoSAX* observation; this range encompasses the possibility of little or no change in the Compton reflection signal over a 2-year interval. The remaining discussion focuses on the iron $K\alpha$ features in the NGC 4151 spectrum.

3.8.1 The iron $K\alpha$ line profile

The iron $K\alpha$ emission observed in the EPIC spectra was modelled as a single, “narrow” (see Section 3.8.2) Gaussian component. The line energy is consistent with the fluorescence of neutral or near-neutral iron (taking into account up to 5 eV systematic error in the energy calibration). Including a

second Gaussian line component (Yaqoob *et al.* 2001) with a significantly broader profile (e.g. $\sigma \approx 0.2$ keV) does not improve the overall fit; the upper limit on the flux in a such a component is 1.0×10^{-5} photons $\text{cm}^{-2} \text{s}^{-1}$. Replacing the narrow line in the best-fit model with the line emission expected from an accretion disk (the **disk-line** model in XSPEC, Fabian *et al.* 1989) results in a similar χ^2 to that obtained with a narrow line. However, in this case the derived inner radius of the accretion disk is r_i , $\sim 1000 r_g$, which results in a disk-line profile closely resembling a Gaussian narrow line. In summary, the high significance *XMM-Newton* spectra reveal only a narrow iron $K\alpha$ line with no evidence for the presence of a strong relativistically broadened iron $K\alpha$ feature. This is contrary to the earlier conclusions of Yaqoob *et al.* (1995), Wang, Zhou & Wang (1999) and Wang, Wang & Zhou (2001), who on the basis of *ASCA* spectra identified broad iron $K\alpha$ features in the NGC 4151 spectrum. Recall that the presence of a broad line was not required in the spectral modelling of the final *ASCA* long-look observation of NGC 4151 (Section 3.5.2; Takahashi, Inoue & Dotani 2002). It remains possible that a relativistically broadened line appears in the X-ray spectrum of NGC 4151 only intermittently or for particular states of the source. Further monitoring of NGC 4151 with *XMM-Newton* and *Chandra* should help clarify whether this is the case.

3.8.2 The iron $K\alpha$ line flux

The measured flux in the narrow iron $K\alpha$ line is $\sim 1.3 \times 10^{-4}$ photons $\text{cm}^{-2} \text{s}^{-1}$, significantly lower than the line fluxes measured in earlier *ASCA*, *BeppoSAX* and *Ginga* observations, where the line flux was more typically $\sim 2.2 \times 10^{-4}$ photons $\text{cm}^{-2} \text{s}^{-1}$; (Section 3.5.2; Yaqoob & Warwick 1991; Yaqoob *et al.* 1993). The present measurement is also somewhat lower than that reported in recent *Chandra* observations ($1.8_{-0.2}^{+0.2} \times 10^{-4}$ photons $\text{cm}^{-2} \text{s}^{-1}$; Ogle *et al.* 2000). Ogle *et al.* (2000) state that *Chandra* spatially resolves $65 \pm 9\%$ of the iron line emission, placing its origin in the ENLR at a distances of up to ~ 500 pc from the continuum source. Thus an iron $K\alpha$ line flux of up to 1.2×10^{-4} photons $\text{cm}^{-2} \text{s}^{-1}$ could be attributable to the ENLR, a value very comparable to that measured in the current *XMM-Newton* observations. The implication is that a component of the iron $K\alpha$ line produced close to the central engine in NGC 4151 almost completely disappeared over the ~ 10 month time interval between the *Chandra* and *XMM-Newton* observations.

However, the spatial line properties are not well determined by the *Chandra* HETG observation analysed by Ogle *et al.* (2000) and the above scenario may not remain valid if it turns out that Ogle *et al.* (2000) have not determined the line properties correctly (a recent re-analysis of the *Chandra* HETG data tentatively suggests that Ogle *et al.* 2000 may have overestimated the spatially resolved fraction of the iron $K\alpha$ line emission; T. Yaqoob. private communication). If all the iron $K\alpha$ line flux does originate close to the central engine, the line flux from this vicinity would only need to decrease by $\sim 35\%$ between the *XMM-Newton* and *Chandra* observations. The decrease in line flux observed between the *BeppoSAX* and *XMM-Newton* observations is in marked contrast with the behaviour of the Compton reflection component, which remains at a similar flux-level or, if anything, is slightly stronger in the

XMM-Newton observation than it was in the *BeppoSAX* observation. This decoupling of the iron $K\alpha$ and the reflection continuum suggests that at least part of the iron $K\alpha$ line is formed in optically-thin, cool clouds located within about a light year of the central source. In this setting the decline of the iron $K\alpha$ line flux presumably coincides with the central source entering a fairly prolonged low flux period, sampled only latterly by the *XMM-Newton* observations.

The variability constraints suggest that a significant component of the iron $K\alpha$ line may be associated with the complex absorbing medium, including the warm absorber. In Section 3.5.2 I note that the predicted range of iron ionization states in the warm medium, determined from a long-look *ASCA* observation, is FeXVI-FeXXI (for which the associated $K\alpha$ line energy is 6.4-6.6 keV). The line energy measured by *ASCA* ($E_{K\alpha}=6.395^{+0.012}_{-0.012}$ keV), excludes much of this range and it was concluded that the bulk of the line flux derives from less strongly photoionized material located further from the nucleus than the warm medium. Comparison of the *ASCA* results with the present *XMM-Newton* observations suggests that the narrow iron $K\alpha$ line may typically be composed of a relatively constant component amounting to $\sim 1.2 \times 10^{-4}$ photons $\text{cm}^{-2} \text{ s}^{-1}$ plus a more variable component of comparable magnitude. Clearly the *XMM-Newton* measurements relate predominantly to the former. The line equivalent width (~ 175 eV referenced to the observed power-law but ~ 60 eV for a more typical continuum level) and energy derived from the *XMM-Newton* observations are consistent with an origin for the constant line component in a neutral or lightly photoionized medium located outside the immediate proximity of the nucleus *i.e.* $r > 1$ pc (although I note that the line energy does not *require* the material in which the line originated to be ionized). On the other hand the variable line emission component may still be associated with the warm absorbing medium provided the dominant ionization state is closer to FeXVI than FeXXI (which could apply if the line-of-sight samples the low end of the ionization distribution in the warm medium). The typical equivalent width of ~ 50 eV for the variable component coupled with the estimate, $N_{H,warm} \approx 2 \times 10^{23} \text{ cm}^{-2}$, then implies that the warm medium subtends an angle of $\sim \pi/A_{Fe}$ steradians as viewed from the central source, where A_{Fe} is the iron abundance relative to solar abundance.

3.8.3 The intrinsic width of the narrow iron $K\alpha$ line

The global best-fit to the *XMM-Newton* data is obtained for an intrinsic line width for the “narrow” iron $K\alpha$ line of $\sigma_{K\alpha} = 33^{+6}_{-5}$ eV. However, continuing uncertainties in the CTI corrections for the current EPIC response matrices will impact on this measurement. An analysis restricted to the to the EPIC MOS spectra provides a good check on the value of the line width, despite the marginally worse spectral resolution at 6.4 keV, since the calibration is relatively better known for the MOS cameras compared with the PN camera. This analysis used epoch-specific response matrices, incorporating a time dependent CTI corrections (S. Sembay, private communication) and yielded an intrinsic line width of $\sigma_{K\alpha} = 51^{+7}_{-7}$ eV (Note: instrument response matrices with a non-standard 1 eV energy scale were used for this analysis). By way of comparison the effective MOS instrument resolution at the observation epoch was $\sigma \sim 70$ eV (FWHM ~ 165 eV).

At face value the EPIC spectra suggest an intrinsic width of between 3000-6000 km s⁻¹ (FWHM) for the iron K α line. In contrast, Ogle *et al.* (2000) report, on the basis of the *Chandra* HETG observations, that “the narrow core of this line is unresolved, with FWHM=1800⁺²⁰⁰₋₂₀₀ km s⁻¹”. Clearly this cautions against over-interpreting the EPIC line widths, particularly since the measurements are close to the limit of the present calibration. However, as noted in the previous section, the line properties are not well constrained from the *Chandra* observation due to the low throughput of the *Chandra* HETG (Yaqoob private communication) and it is possible that improved *Chandra* observations may confirm the line width measured by *XMM-Newton*.

What might be the origin of such line broadening, if confirmed? One consideration is that the iron K α line is in fact a doublet with components at 6.404 (K α_1) and 6.391 (K α_2) keV. However, modelling the iron K α emission feature with two Gaussian components with a fixed 13 eV energy separation and flux ratio of 2:1 respectively (as per the branching ratio) has little impact on the observed line width. A further possibility is that the K α line appears broadened because it represents a blend of lines from a range of ionization states. However, the measured line energy is fully consistent with that of neutral iron at 6.400 keV (representing the centroid of the K α_1 and K α_2 components) and adding non-neutral line components fails to replicate the low-energy wing of the line. Finally the line broadening could be due to Doppler shifts, which would place the origin of the K α line observed by *XMM-Newton* squarely in the Broad Line Region of the galaxy. Unfortunately this description is then at odds with the previous suggestion that the relatively constant component of the line emission (observed by *XMM-Newton*) may originate in lightly photoionized matter beyond ~ 1 pc from the nucleus.

3.8.4 The deep iron edge - a clue to iron over abundance.

The best-fit spectral model includes iron edge features imprinted on the direct continuum by the neutral and warm absorbers and the Compton reflection component, with solar metal abundances are assumed in each case. However, as detailed earlier, the high signal-to-noise EPIC spectra require the inclusion of additional absorption above 7 keV suggestive of an overabundance of iron in the absorbing and/or reflecting media.

The derived energy of the additional absorption edge is consistent with absorption by neutral iron (with the upper limit of 7.13 eV, including a systematic uncertainty of 5 eV, formally excluding even Fe II). This rules out an association of the excess absorption with the warm absorber, for which the predicted range of edge energies is 7.8-8.3 keV (FeXVI-FeXXI). The observed optical depth in the edge ($\tau_{K,Edge} \approx 0.12$) can be interpreted as being due to an extra-solar abundance of iron in the cold absorber and if so this results in an iron overabundance of ~ 3.6 , whereas its association with the Compton-reflector would imply $A_{Fe} \sim 2.3$. Alternatively, allowing an overabundance in *both* the cold absorber and the reflector results in an iron overabundance of ~ 2 . Previous studies have also reported evidence for an overabundance of iron in NGC 4151, for example Yaqoob *et al.* (1993) quote a canonical value of $A_{Fe} \sim 2.5$ times solar, based

on the average of many *Ginga* measurements.

3.9 Conclusions from *XMM-Newton*

Recent observations with the EPIC cameras on *XMM-Newton* have provided a very high signal-to-noise measurement of the hard (2.5-12 keV) X-ray spectrum of the archetypal Seyfert galaxy NGC 4151. Remarkably, the spectral template model developed in Section 3.3 and fit to previous *BeppoSAX* and *ASCA* observations, also provides an excellent description of the *XMM-Newton* data, with only minor modifications.

This supports the view that the complex spectral variability exhibited by NGC 4151 over timescales longer than a few days is the product of changes in the source, driven predominantly by the level of the underlying continuum. The ingredients of the spectral model are surprisingly simple. An underlying power-law continuum is absorbed below ~ 5 keV by a combination of warm and cold gas along the line-of-sight but supplemented at higher energy by Compton reflection. The parameters specifying the continuum slope, the column densities and the Compton reflection flux remain essentially constant. There is no requirement for a relativistically broadened iron $K\alpha$ line feature, but the intensity of the narrow component definitely varies on long (years) timescales. There is also a strong hint for twice-solar iron abundance in either the cold absorbing and/or reflecting media.

Further development of this picture of the hard X-ray properties of NGC 4151 will be possible through future approved *XMM-Newton* observations aimed at monitoring spectral changes in the 2.5-12 keV band. With the addition of a simultaneous *INTEGRAL* observation it will be possible to test the assumption that it is the level of the broad-band hard X-ray continuum which governs such changes.

Chapter 4

The hard X-ray spectra of Markarian 3 and NGC 7582

4.1 Overview: Increasing the absorption.

This chapter focuses on the analysis of the hard (2.5-10 keV) X-ray spectra of NGC 7582 and Markarian 3 (hereafter Mrk 3).

The most recent *BeppoSAX* observation of NGC 7582 (Turner *et al.* 2000) revealed a hard X-ray spectrum that was similar to the hard X-ray spectrum of NGC 4151 discussed in the previous chapter. The recent *XMM-Newton* observation of NGC 7582, however, tells a somewhat different story. The *XMM-Newton* EPIC spectra require a flatter spectrum with considerably heavier ($\sim 8 \times 10^{23} \text{ cm}^{-2}$) absorption and strong iron features. The major spectral differences between these two observations (and other previous observations with *ASCA* and *ROSAT*) are interpreted as the result of a highly, albeit slowly, variable absorbing column density impinging on the central AGN continuum. When the column density is relatively low the source spectrum is similar to that of NGC 4151 (although there is no evidence for any ionized absorption in this source). However, as the column density increases the hard X-ray spectrum becomes increasingly dominated by Compton reflection. The iron edge feature observed in the X-ray spectrum of NGC 7582 provides evidence for mild ionization of the reflecting material, although the inferred ionization state of the iron in the Compton reflection component (Fe III) is not sufficiently high to cause the associated iron $K\alpha$ line emission to be distinguishable from that of cold, neutral iron. The absorbing column density in NGC 7582, even at its highest observed value, is significantly smaller than the absorbing column observed in Mrk 3. The *XMM-Newton* observation of Mrk 3 reveals an extremely flat hard X-ray spectrum, imprinted with prominent iron features. Previous X-ray spectral studies with *BeppoSAX* and *ASCA* revealed Mrk 3 to be a heavily absorbed source that, in the 2-10 keV range, may

be dominated by Compton reflection (Cappi *et al.* 1999). The analysis of the *XMM-Newton* data confirms both the dominance of Compton reflection and the very heavy absorption ($\sim 10^{24} \text{ cm}^{-2}$) of the underlying continuum. No evidence was found for the partial photoionization of either the absorption or Compton reflection components in Mrk 3, rather, both the absorption and the Compton reflection component arise in neutral material.

This chapter is organised as follows. Section 4.2 focuses on NGC 7582. Section 4.2.1 presents the details of the *XMM-Newton* EPIC and *Chandra* observations. Section 4.2.2 discusses the EPIC light-curve and the possible impact of a variable absorbing column on the hard X-ray spectrum. Detailed modelling of the *XMM-Newton* data is described in Section 4.2.3, focusing on the effect of the variable continuum and the ionization of the Compton reflection component. Section 4.3 deals with Mrk 3. Section 4.3.1 presents the details of the *XMM-Newton* EPIC observation of Mrk 3 and the spectral modelling of the EPIC data, focusing on the impact of the increased absorption on the X-ray spectrum, is described in Section 4.3.2. Finally, Section 4.4 discusses the implications of the results from Mrk 3 and NGC 7582 in the context of AGN unified models and the similarities between these sources and NGC 4151.

4.2 NGC 7582

NGC 7582 is a nearby ($z=0.0053$) Seyfert 2 galaxy observable from the southern hemisphere. It is one of four galaxies that form the Grus Quartet (Xue *et al.* 1999). Optically classified as Seyfert 2 galaxy, X-rays studies have shown NGC 7582 to be the brightest “Narrow-Line X-ray Galaxy” (hereafter NLXG) in the sky (Schachter *et al.* 1998). With optical line widths of less than 200 km s^{-1} and no discernible broad features (particularly an absence of broad $\text{H}\alpha$), it is the most likely of the NLXG’s to be starburst, rather than AGN, dominated (Moorwood & Oliva 1990; Wilson & Nath 1990). Previous X-ray studies of NGC 7582 have failed to unambiguously resolve whether NGC 7582 is starburst or AGN dominated (Turner *et al.* 1997a; Warwick *et al.* 1993), largely due to a high level of nearby source confusion (specifically the cluster Abell S1101, $53'$ away, the BL Lac object PKS 2316-423 $17'$ away, and an undefined source $2'$ to the NE). However, the analysis of an observation with *ASCA*, in conjunction with an observation from the *ROSAT* HRI, eliminated much of the source confusion and revealed a flat X-ray spectrum that displays considerable rapid variability in the 3-8 keV band, clearly demonstrating that NGC 7582 harbours an AGN (Schachter *et al.* 1998). The soft X-ray flux remained constant during the *ASCA* observation, prompting Schachter *et al.* (1998) to suggest the soft X-ray emission is either starburst in origin or, more likely, that it is the result of the reprocessing of its nuclear continuum (electron scattering, emission from photoionized material or emission associated with Compton reflection) in distant material. The soft X-ray light-curve from the *ASCA* observation analysed by Turner *et al.* (1997a) demonstrates considerable variability, however they note that the light-curve is difficult to interpret due to the number of bright, nearby, confusing sources in their *ASCA* observation. The subsequent observation of NGC 7582 by *BeppoSAX* in 1999 proved to be somewhat more successful in modelling the X-ray

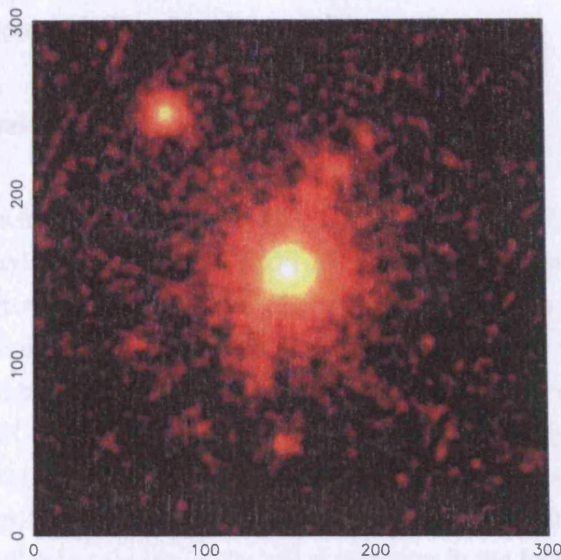


Figure 4.1: Logarithmically scaled, smoothed *XMM-Newton* 0.3-10.0 keV X-ray image. The image is 5' on a side centred on RA: 23 18 29.45, Dec: -42 23 0.0. The image is smoothed with a 2'' Gaussian kernel.

spectrum and provided even stronger evidence for the presence of an AGN, through its high energy PDS data (Turner *et al.* 2000). The 13-60 keV light-curve displayed considerable rapid variability (factor of 2 changes on ~ 15 ks timescales) that was correlated with the variability in the 5-10 keV band, clearly demonstrating the presence of the AGN in NGC 7582. In modelling the X-ray spectrum, Turner *et al.* (2000) conclude that a partial covering absorption model provided the best description of the hard X-ray spectrum of NGC 7582, despite a Compton reflection dominated model providing a marginally better fit to the data. A comparison of the level of absorption observed by *BeppoSAX* to that observed in the earlier *ASCA* observation revealed considerable column density variations (by $\sim 7 \times 10^{22} \text{ cm}^{-2}$) between the two observations.

Despite the success of the *ASCA* and *BeppoSAX* observations in confirming the presence of an AGN in NGC 7582, the detailed properties of the AGN are poorly constrained by the current observations. Specifically, the detailed nature of the X-ray continuum, the heavy absorption that impinges upon it and the possible presence of a Compton reflection component are not well constrained (Xue *et al.* 1999; Schachter *et al.* 1998; Turner *et al.* 2000). Iron reprocessing features (a neutral $K\alpha$ line and edge) were detected in both the *ASCA* and *BeppoSAX* spectra. Unfortunately, Xue *et al.* (1999) suggest that the detected properties of the iron features in NGC 7582 do not necessarily help constrain the properties of the absorption, continuum or the Compton reflection.

4.2.1 The *XMM-Newton* and *Chandra* observations

The *XMM-Newton* observation

NGC 7582 was observed with *XMM-Newton* on May 25th, 2001 (orbit 267), for a total of ~ 23 ks. The source was positioned on-axis in both the EPIC MOS and PN cameras (Turner *et al.* 2001b; Strüder *et al.* 2001) with the medium filter in place. The EPIC cameras were operated in Full Window Mode (FWM) for the full duration of the observation. The data were screened with the public release of the *XMM-Newton* SAS v5.3 standard processing chains, to remove known hot pixels and columns. The data were processed with the latest CCD gain values and only X-ray events flagged as good and corresponding to patterns 0-12 in the MOS cameras and pattern 0-4 events in the PN camera were used to create the source light-curves, images and spectra. Investigation of the full field count rate for the observation revealed no significant flaring events, allowing the use of the full observation in the following analysis and resulting in effective total exposure times of 22.5 and 18 ks for the MOS and PN instruments respectively. A full field *XMM-Newton* image (Figure 4.1) highlights the complex nature of this field, including several nearby discrete sources and prominent extension and structure associated with the central X-ray emission. Imaging analysis from a recent unpublished *Chandra* observation of NGC 7582 (brief details of the observation and imaging analysis are given below) was used to investigate the source confusion issues and to assess the nature and impact of the “extended” emission apparent in the *XMM-Newton* images.

The *Chandra* observation and imaging analysis

NGC 7582 was observed with *Chandra* twice, on October 14th and 15th, 2000 for a combined total duration of ~ 20 ks. NGC 7582 was positioned at the primary focus of the Advanced CCD Imaging Spectrometer ‘Spectroscopy array’ (ACIS-S) without the gratings in place. The data were pipeline processed by the The *Chandra* X-ray Center (CXC), and were obtained from the *Chandra* data archive via HEASARC[†]. Images were extracted from the pipeline processed events file in the bands 0.3-1, 1-2, 2-5 and 5-10 keV from the central on-axis region of the observation. The individual images were adaptively smoothed using the *csmooth* task within the *Chandra* Interactive Analysis of Observations (CIAO) v2.1 software system. The 0.3-1 keV image (Figure 4.2; Left Panel) highlights the complexity of the field, showing the dominant central AGN along with several nearby point sources. Along with considerable low surface brightness extended emission the image displays prominent, bright, extended emission to the W and SW of the source. This emission is unresolved but it is likely to be caused by point sources in the vicinity of the nucleus of NGC 7582. Fortunately, the source confusion evident in the *Chandra* soft X-ray image is not mirrored in the slightly harder 1-2 keV band image (Figure 4.2; Right Panel), effectively eliminating source confusion as a problem for the spectral analysis of the central source, provided that the analysis is restricted to energies above ~ 1 keV.

[†]<http://heasarc.gsfc.nasa.gov/>

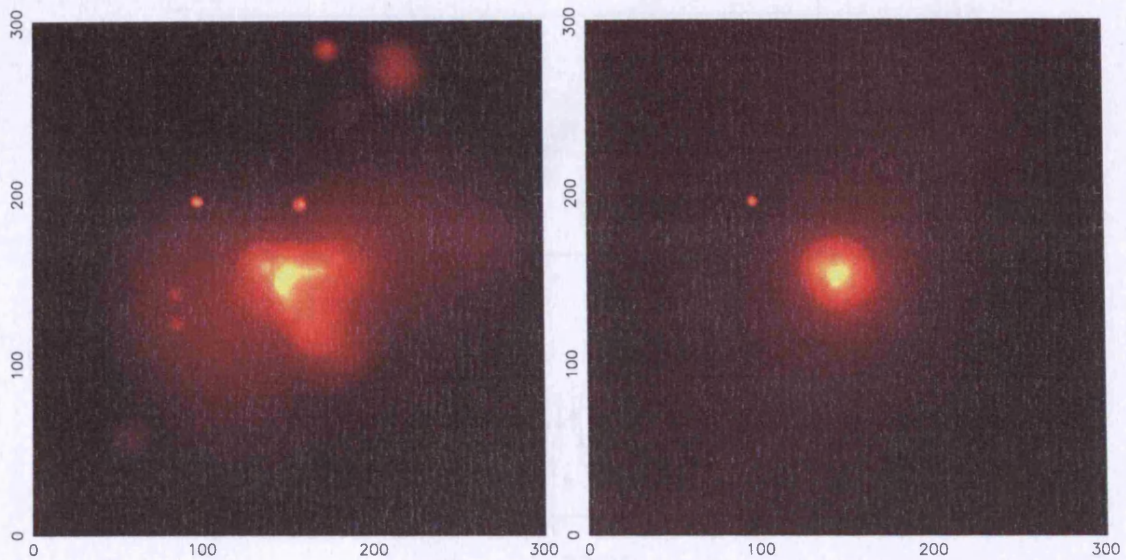


Figure 4.2: Logarithmically scaled, adaptively smoothed *Chandra* X-ray images. The images are $2.5'$ on a side centred on RA: 23 18 29.45, Dec: -42 23 0.0. The images are adaptively smoothed with a Gaussian kernel with a minimum signal-to-noise of 2σ and a maximum signal-to-noise of 5σ . *Left Panel*: 0.3-1 keV Image. The image clearly displays the central source along with several nearby point sources. The extension to the west and southwest of the source is unresolved and is likely to be caused by point sources near the nucleus of NGC 7582. *Right Panel*: 1-2 keV image. The image clearly displays the increasing dominance of the central source along with only two remaining nearby point sources to the NE of the central source.

4.2.2 The light-curve

Following the confirmation from the *Chandra* observation of the relatively uncontaminated nature of the central AGN source above ~ 1 keV, *XMM-Newton* EPIC source light-curves were extracted from a circular region of $40''$ radius [chosen to avoid including the bright off-nuclear source seen to the NE of the nucleus in the 1-2 keV *Chandra* image (Figure 4.2; Right Panel)]. The light-curves were not background corrected because an investigation of the background level during the observation revealed no significant flaring episodes and the total background contribution to the light-curves is less than 3% of the total source counts. The 2-10 keV light-curve (Figure 4.3; Upper Panel) shows extremely rapid large scale variability, the most rapid period of which sees the source flux increase by $\sim 70^{+80}_{-40}\%$ in a period of ~ 400 seconds! Similar scale rapid variability is seen across the entire 25 ks light-curve. As well as marked short timescale variability, the 2-10 keV light-curve also displays longer timescale variability with the mean flux falling by $\sim 20\%$ over the duration of the observation. An investigation into any associated spectral variability revealed that the 2-5 keV band is somewhat less variable than the 5-10 keV band (testing the 2-5 keV light-curve against a constant value yielded a $\chi^2_{red}=1.19$ whereas a $\chi^2_{red}=1.35$ was measured for 5-10 keV band). The 2-5 keV band shows significant short timescale variability, demonstrated by the 2-5 keV/5-10 keV softness ratio (Figure 4.3; Lower Panel), but remains relatively constant on long timescales (testing the softness ratio against an average constant value yielded

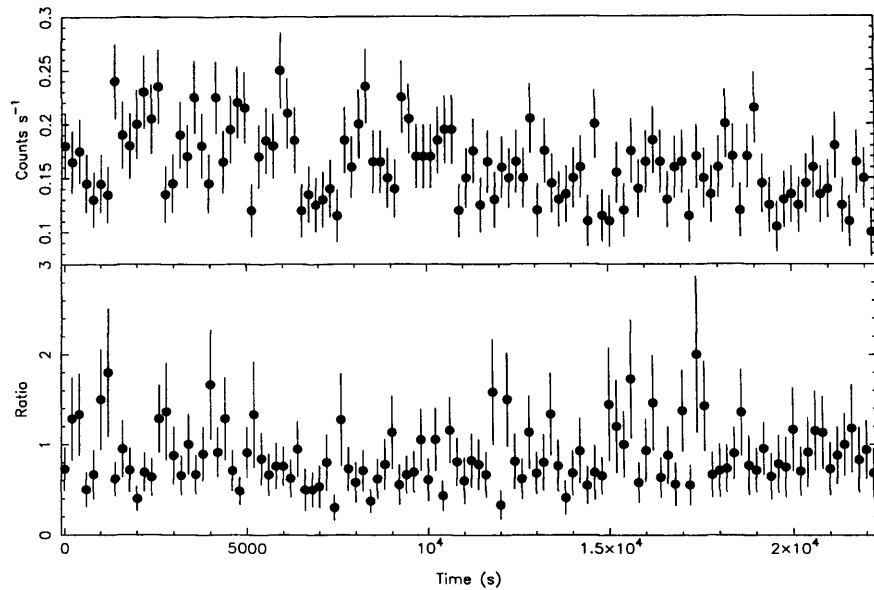


Figure 4.3: *Upper Panel* The 2-10 keV X-ray count rate light-curve from the co-added *XMM-Newton* EPIC MOS detectors (200s bins). *Lower Panel* The variability of the 2-5 keV/5-10 keV X-ray softness ratio during the observation (200s bins).

a $\chi^2_{red}=0.91$). The short timescale variability implies that a significant fraction of the underlying X-ray continuum is present below 5 keV.

4.2.3 The spectral analysis

Source spectra for NGC 7582 were extracted from the same region as the light-curves (a circular region of $40''$ radius, centred on the central source). Corresponding background information was extracted from a distant, source-free, region (with the same physical dimensions) located on the same chip. Appropriate spectral response matrices and ancillary response files were created with the SAS tasks *rmfgen* and *arfgen*. As elsewhere in this work, the source spectra were grouped to give a minimum of 20 counts per bin to allow the use of χ^2 minimisation techniques. Figure 4.4 shows the full-band *XMM-Newton* EPIC spectra of NGC 7582. The details of the soft (0.3-2.5 keV) spectrum of NGC 7582 are not discussed in this work, due to the considerable contamination of the soft X-ray emission by the numerous nearby soft X-ray point sources identified by *Chandra*. The remainder of this chapter is restricted to the analysis of the hard X-ray spectrum of NGC 7582.

The 2.5-10 keV spectrum shows only a small degree of curvature between 2.5 and 6 keV, and above 6 keV it is dominated by reprocessed continuum emission features; namely a strong iron $K\alpha$ fluorescence line and a correspondingly strong iron K absorption edge. NGC 7582 was initially modelled in a very similar fashion to the spectral modelling of NGC 4151 described in chapter 3. The model consists of a heavily absorbed power-law continuum, a neutral Compton reflection component and a Gaussian emission line

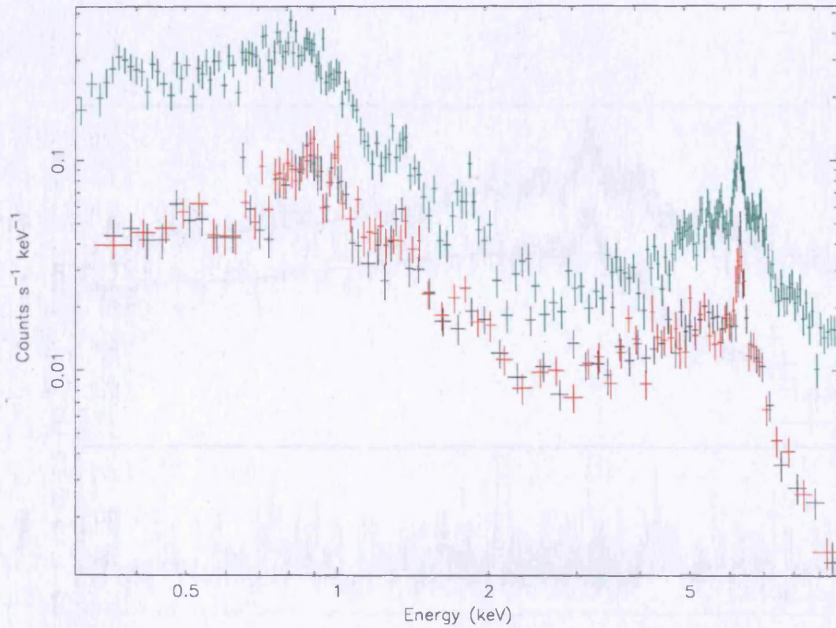


Figure 4.4: The *XMM-Newton* EPIC co-added MOS (black and red) and single PN (green) spectra of NGC 7582.

to represent the strong iron $K\alpha$ line in the spectrum. In contrast to the modelling of NGC 4151, the absorption employed here is not a mixture of ionized and cold gas, but instead originates entirely in cold (*i.e.* neutral) material. The column density for the absorption is a free parameter in the model and was initially set at the value previously reported for NGC 7582 ($1.24 \times 10^{23} \text{ cm}^{-2}$; Bassani *et al.* 1999), which suggests that significant continuum emission is present in the spectrum down to below 5 keV (in keeping with the conclusions drawn from the 2-5 keV light-curve variability). The photon index of the power-law continuum is a free parameter in the model fits, despite the available *BeppoSAX* data, because the previous analysis of the *BeppoSAX* data does not account for a Compton reflection component (Turner *et al.* 2000). The cut-off energy of the hard power-law was fixed at 100 keV and the properties of the neutral Compton reflection component were tied to those of the observed hard power-law continuum. Similar to the analysis of NGC 4151, $\cos i$ was fixed at 0.5 and the metal abundance in the reflector was fixed at the solar value. This model provides an excellent fit to the *XMM-Newton* EPIC spectra ($\chi^2=369$ for 357 d.o.f); the model parameters are given in Table 4.1 (Model A) and the fit is shown in Figure 4.5.

Despite the excellent overall fit that this model provides to the *XMM-Newton* EPIC spectra, the data/model ratios around 7 keV suggest that the spectrum around this energy is not particularly well modelled. The most prominent spectral feature in this region is the iron K absorption edge and the systematic under-prediction of the data by the model suggests that the iron edges currently included in the model (from the neutral Compton reflection and the cold absorption) are at a lower energy than the edge present in the data. There are several possible explanations for this discrepancy, the most plausible of which is that the reflecting material is mildly ionized. This hypothesis was tested by replacing the neutral Compton reflection component in the model with ionized Compton reflection (using the **pexriv** model in XSPEC). The

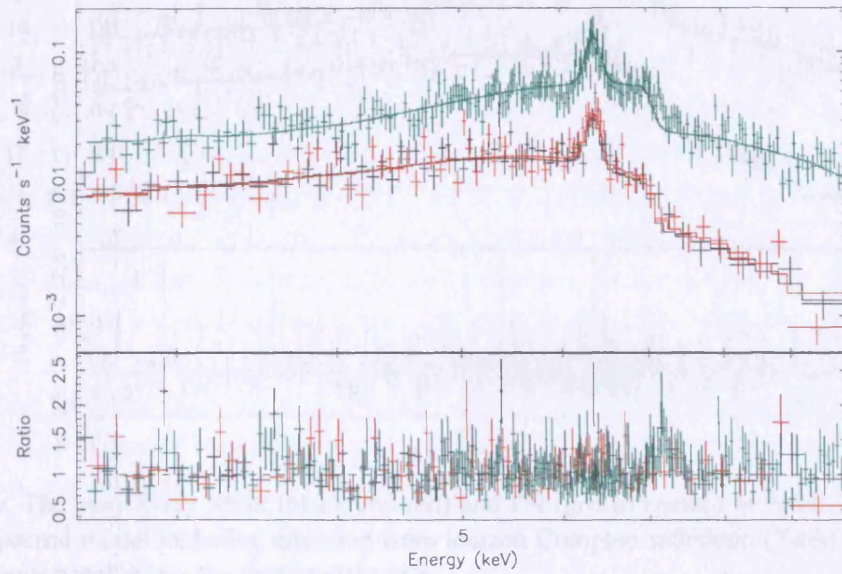


Figure 4.5: The hard X-ray MOS (black and red) and PN (green) spectra of NGC 7582 fit with the initial spectral model (Table 4.1 - Model A) . The lower panel shows the data/model ratios.

Table 4.1: NGC 7582 Best-fit model parameters

Parameter	Model A	Model B	
N_H	$7.70^{+0.73}_{-0.65}$	$8.09^{+0.81}_{-0.70}$	$\times 10^{23} \text{ cm}^{-2}$
Γ	$2.22^{+0.04}_{-0.12}$	$2.21^{+0.23}_{-0.08}$	
A_{PL}	$1.28^{+0.43}_{-0.21}$	$1.31^{+1.20}_{-0.15}$	$\times 10^{-2} \text{ photons s}^{-1} \text{ cm}^{-2} \text{ keV}^{-1}$
R	$1.79^{+0.46}_{-0.39}$	$1.63^{+0.26}_{-0.53}$	
$\log(\xi)$	-	$0.26^{+0.67}_{-0.78}$	
$E_{K\alpha}$	$6.455^{+0.012}_{-0.012}$	$6.455^{+0.013}_{-0.012}$	keV
$\sigma_{K\alpha}$	0.053^a	0.053^a	keV
$I_{K\alpha}$	$2.05^{+0.26}_{-0.32}$	$1.97^{+0.29}_{-0.27}$	$\times 10^{-5} \text{ photons s}^{-1} \text{ cm}^{-2}$
χ^2	369	354	
d-o-f	357	356	

^a Upper Limit

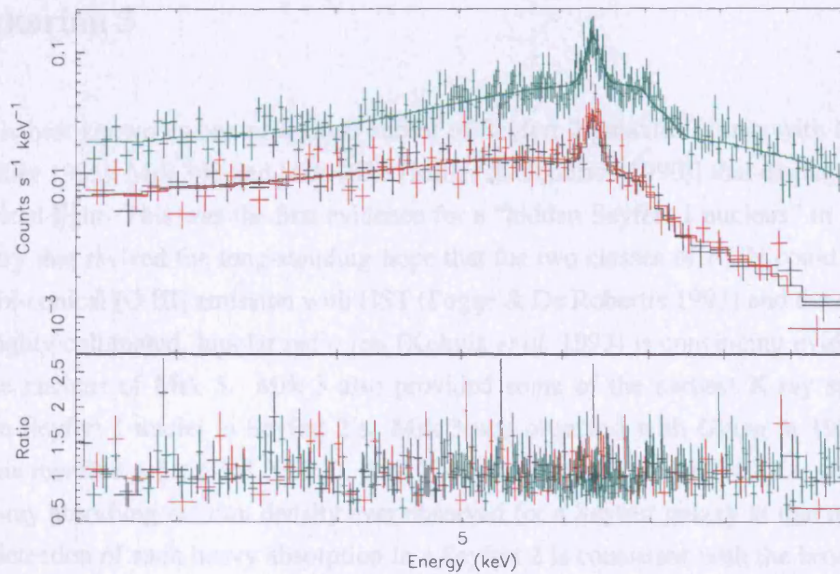


Figure 4.6: The hard X-ray MOS (black and red) and PN (green) spectra of NGC 7582 best-fit with the spectral model including emission from ionized Compton reflection (Table 4.1 - Model B). The lower panel shows the data/model ratios.

ionized Compton reflection model has two extra parameters that were not present in the neutral Compton reflection model, the “disk” temperature and the ionization parameter. The ionization parameter is defined in the same fashion as the ionization parameter of the warm absorber detailed in Equation 3.1 (Section 3.3). The temperature of the emitting material (i.e. “disk” temperature parameter) was fixed at a value of 3×10^4 K, while the ionization parameter was a free component in the fit. The remaining model parameters for the ionized Compton reflection model were tied to the hard continuum power-law in the same fashion as the neutral Compton reflection component described above. Fitting this model yielded an improvement in the fit at almost the 4σ level ($\Delta\chi^2=15$ for 1 degree of freedom, which results in a significance for the improvement of 99.98% according to the FTEST). The model parameters for the ionized reflection model are given in Table 4.1 (Model B) and the fit is shown in Figure 4.6. It is also plausible that a contribution to the residuals around this energy is due to the presence of iron $K\beta$ line emission. The impact of iron $K\beta$ on the fit was assessed by the addition of a Gaussian emission line to the model, in the correct ratio for the $K\beta$ line relative to the $K\alpha$ line emission (10%) and with the correct rest-frame line energy and the line width fixed at the line width of the iron $K\alpha$ line. The addition of the iron $K\beta$ emission line did not improve the fit significantly and is not *required* by the data, however the model including the iron $K\beta$ emission line is consistent with the data.

4.3 Markarian 3

Markarian 3 is best known as one of a small subset of Seyfert 2 galaxies [along with NGC 1068 (Antonucci & Miller 1985), Mrk 348 and Mrk 463E (Miller & Goodrich 1990)] that display broad emission lines in polarised light. This was the first evidence for a “hidden Seyfert 1 nucleus” in Seyfert 2 galaxies, a discovery that revived the long-standing hope that the two classes of AGN could be unified. The discovery of bi-conical [O III] emission with HST (Pogge & De Robertis 1993) and the existence of perpendicular, highly collimated, bipolar radio jets (Kukula *et al.* 1993) is convincing evidence for Seyfert activity in the nucleus of Mrk 3. Mrk 3 also provided some of the earliest X-ray spectral evidence for the hidden Seyfert 1 nuclei in Seyfert 2’s. Mrk 3 was observed with *Ginga* in 1989 (Awaki *et al.* 1990), and this revealed a flat ($\Gamma=1.3\pm0.3$), hard X-ray spectrum, a strong iron $K\alpha$ emission line, and the largest X-ray absorbing column density ever observed for a Seyfert galaxy at that time ($6_{-2}^{+3} \times 10^{23} \text{ cm}^{-2}$). The detection of such heavy absorption in a Seyfert 2 is consistent with the broad lines found in polarisation studies and can explain the weak detections (or often only upper limits) on the soft X-ray fluxes of Seyfert 2s in *EINSTEIN* observations. Following these analyses Mrk 3 has been the subject of extensive study with all the major X-ray satellites (*ROSAT* - Griffiths *et al.* 1998; *ASCA* - Iwasawa *et al.* 1994; *BeppoSAX* - Cappi *et al.* 1999; *RXTE* - Georgantopoulos *et al.* 1999; *Chandra* - Sako *et al.* 2000) which has revealed a broad-band X-ray spectrum that is a complex mixture of heavy absorption, Compton reflection, strong iron features, and a multitude of soft X-ray emission lines.

One of the most puzzling aspects of the X-ray study of Mrk 3 is the anomalously flat nature of its 3-10 keV spectrum. Modelling of the 3-10 keV spectrum alone highlights the strong impact that the input spectral slope of the X-ray continuum has on the measured absorbing column density. The very hard (>10 keV) intrinsic X-ray to γ -ray continuum of Mrk 3, similar to the continuum described in NGC 4151 (Sections 2.4.3 & 3.2) has been tightly constrained by previous modelling of the *BeppoSAX* PDS data (Cappi *et al.* 1999). The underlying hard X-ray continuum has a best-fit photon index of $\Gamma=1.8$, in contrast with the flat slope measured from the *Ginga* observation, but consistent with the “average” continuum spectrum observed in Seyfert 1 galaxies (Nandra & Pounds 1994). To reconcile the 13-60 keV continuum slope with the flat spectrum observed in the 3-10 keV band, the continuum must be extremely heavily absorbed ($\sim 10^{24} \text{ cm}^{-2}$) and have little impact on the spectrum below ~ 7 keV (Cappi *et al.* 1999). Instead the flat continuum slope observed by *ASCA* and *BeppoSAX* in the 2.5-10 keV range is interpreted as the result of either a partial coverer (several different levels of absorption each partially covering the source) or strong Compton reflection (Turner *et al.* 1997b). Neither the *BeppoSAX*, or the *ASCA* data are of sufficient quality to strongly distinguish between these two models (Cappi *et al.* 1999, Griffiths *et al.* 1998), although the data are marginally better fit by a Compton reflection dominated model than a partial covering model. A recent observation of Mrk 3 with the *Chandra* HETG provided the highest resolution observation of Mrk 3 yet and showed a flat hard X-ray spectrum that, above ~ 6 keV, is dominated by a strong, near neutral, iron $K\alpha$ line and a prominent iron K edge (Sako *et al.* 2000). This broad spectrum is interpreted as a reflection dominated continuum however, the limited statistical

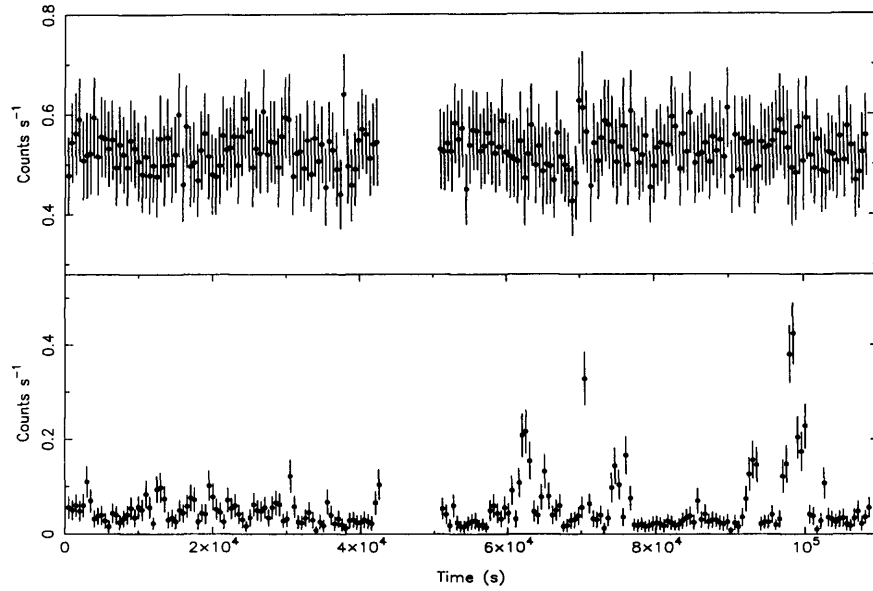


Figure 4.7: *Upper Panel* The background subtracted *XMM-Newton* EPIC MOS light-curve of Mrk 3. *Lower Panel* The *XMM-Newton* EPIC MOS light-curve from a source free (*i.e.* background) region with the same dimensions and on the same chip as the source extraction cell. In both light-curves, the individual MOS detectors have been co-added for simplicity.

quality of the data prevents the properties of both the Compton reflection component and the absorbed power-law from being well constrained.

4.3.1 The *XMM-Newton* observations

Markarian 3 was observed with *XMM-Newton* twice on October 10th, 2000 (orbit 158), for a total of ~ 100 ks. Mrk 3 was positioned on-axis in both the EPIC MOS and PN cameras (Turner *et al.* 2001b; Strüder *et al.* 2001) with the medium filter in place. Both the observations were performed in FWM for all the instruments. The events were screened with the public release of the *XMM-Newton* SAS v5.3 standard processing chains, to remove known hot pixels and columns. The data were processed with the latest CCD gain values and only X-ray events flagged as good and corresponding to patterns 0-12 in the MOS cameras and pattern 0-4 events in the PN camera were used to create the light-curves, images and spectra. The PN camera encountered problems during the first of the two observations, preventing the PN data from this period being processed. Investigation of the full field count rate in the MOS cameras for the observations revealed some relatively low significance flaring events during both of the observations.

Source light-curves and spectra were extracted from a circular region of 1.3' radius centred on the source (chosen to avoid including a nearby X-ray source) and corresponding background information was extracted from a source free region of the same dimensions located on the same chip. The MOS instruments were co-added to simplify the analysis of the source and background light-curves. None of the

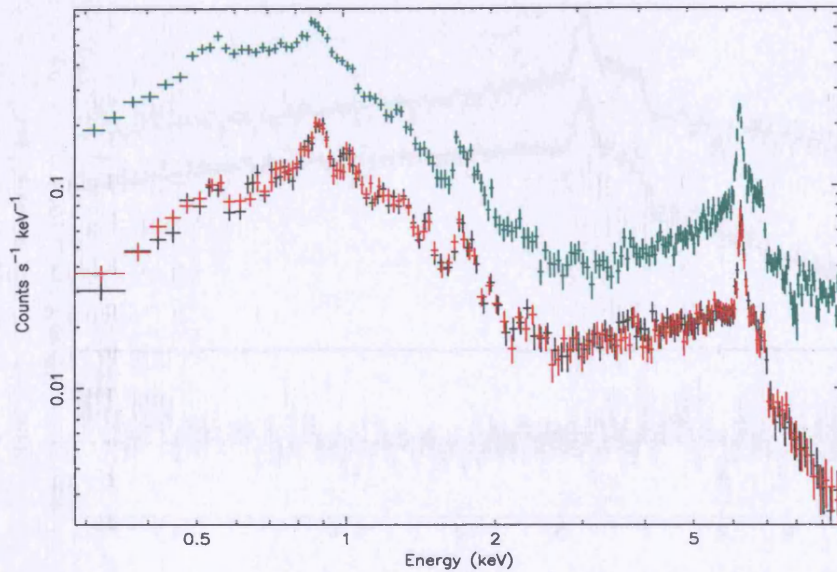


Figure 4.8: The *XMM-Newton* EPIC MOS (black and red) and single PN (green) spectra of Mrk 3. The spectra here are co-added from both observations of Mrk 3.

background flaring events contribute more than an additional 0.4 c/s to the total co-added MOS count rate within the source extraction region ($\sim 2/3$ of the source count rate; Figure 4.7 Lower Panel). Fortunately, the background flaring events are well represented in the background extraction region and the subtraction of the background light-curve from the source light-curve is extremely effective at removing the effects of the flaring events from the source data. The background subtracted, co-added MOS, light-curve is shown in Figure 4.7 (Upper Panel) and clearly displays the remarkable constancy of the X-ray flux during this long observation. The successful background subtraction allows the entirety of both observations to be used for the spectral analysis, resulting in effective total exposure times of 101 ks and 53 ks for the MOS and PN instruments respectively. Appropriate spectral response matrices and ancillary response files were created with the SAS tasks *rmfgen* and *arfgen*. The spectral background subtraction removes between 8-10% of the total counts from the source spectra in the MOS instruments, and $\sim 13\%$ from the PN. Again, the source spectra were grouped to give a minimum of 20 counts per bin to allow the use of χ^2 minimisation techniques.

4.3.2 The spectral analysis

Figure 4.8 shows the full-band *XMM-Newton* EPIC spectra of Mrk 3. The soft (0.3-2.5 keV) spectrum of Mrk 3 is known to be composed of a multitude of X-ray emission lines (Sako *et al.* 2000), and the details of the *Chandra* grating spectrum are compared with the RGS spectrum of NGC 4151 in chapter 6. The *XMM-Newton* RGS and soft X-ray EPIC spectra are not discussed in this thesis and the remainder of this chapter is restricted to the analysis of the hard X-ray spectrum of Mrk 3.

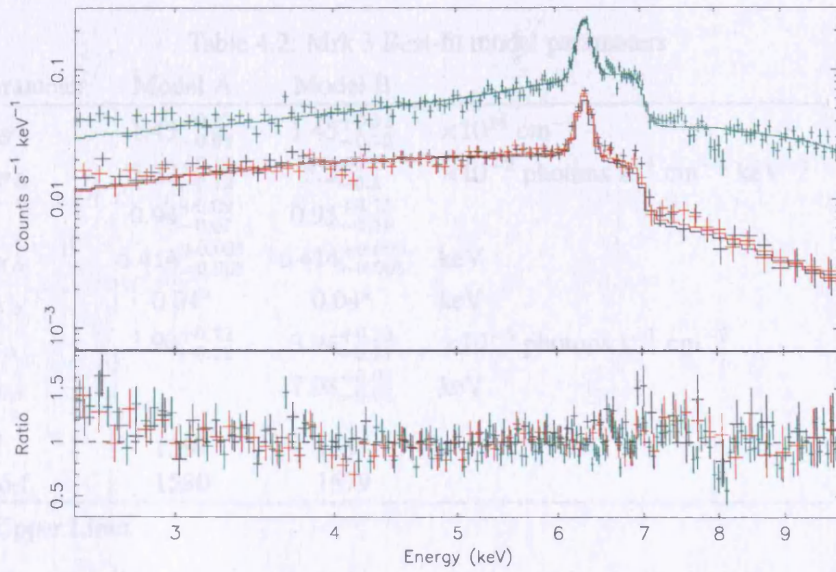


Figure 4.9: The hard X-ray MOS (black and red) and PN (green) spectra of Mrk 3 best-fit with the initial spectral model. The lower panel shows the data/model ratios.

The 2.5-10 keV X-ray spectrum of Mrk 3 shows a qualitatively similar spectral form to that of NGC 7582 during the latter's recent *XMM-Newton* observation. The spectrum is extremely flat with similar strong neutral iron emission line and absorption edge features. The large iron line coupled with the flat spectrum between 2.5 and 6 keV is indicative of a Compton reflection dominated spectrum. This interpretation for the hard X-ray spectrum of Mrk 3 was previously suggested on the basis of *ASCA* and *BeppoSAX* data (Cappi *et al.* 1999; Griffiths *et al.* 1998; Turner *et al.* 1997b) and the *XMM-Newton* EPIC spectra presented here are modelled after the same fashion. The initial spectral model is the same as that used to model NGC 7582 and, to recap, consists of a heavily absorbed power-law continuum, unabsorbed neutral Compton reflection and a Gaussian emission line to represent the strong iron $K\alpha$ line. In this analysis the photon index of the power-law continuum was fixed at $\Gamma=1.79$ and the cut-off energy of the hard power-law was fixed at 200 keV based on the analysis of the *BeppoSAX* observation of Mrk 3 by Cappi *et al.* (1999) (which included a Compton reflection component). In similar fashion to the analysis of NGC 4151 and NGC 7582, the properties of the neutral Compton reflection component were tied to those of the hard, absorbed, power-law, $\cos i$ was fixed at 0.5 and the metal abundance in the reflecting material was fixed at the solar value. The absorption of the hard X-ray continuum is modelled as absorption from cold material, similar to that used in NGC 7582 and the previous studies of this source. Fitting this model to the *XMM-Newton* EPIC spectra results in an excellent fit to the data ($\chi^2=1397$ for 1580 d.o.f), providing further confirmation of the success of the model proposed by Turner *et al.* (1997b). The best-fit model parameters are given in Table 4.2 (Model A) and the fit is shown in Figure 4.9.

Despite the excellent overall fit of this simple model, it is clear from the spectral ratios that there are several specific regions of the spectrum that are not well modelled. The slow rise below 3 keV may be the result of the soft X-ray emission line spectrum impacting upon the nuclear spectrum of Mrk 3. The

Table 4.2: Mrk 3 Best-fit model parameters

Parameter	Model A	Model B	
N_H	$1.43^{+0.17}_{-0.08}$	$1.45^{+0.12}_{-0.12}$	$\times 10^{24} \text{ cm}^{-2}$
A_{PL}	$2.22^{+0.12}_{-0.12}$	$2.2^{+0.2}_{-0.3}$	$\times 10^{-2} \text{ photons s}^{-1} \text{ cm}^{-2} \text{ keV}^{-1}$
R	$0.94^{+0.09}_{-0.07}$	$0.95^{+0.15}_{-0.18}$	
$E_{K\alpha}$	$6.414^{+0.005}_{-0.005}$	$6.414^{+0.005}_{-0.005}$	keV
$\sigma_{K\alpha}$	0.04^a	0.04^a	keV
$I_{K\alpha}$	$3.90^{+0.22}_{-0.22}$	$3.94^{+0.23}_{-0.21}$	$\times 10^{-5} \text{ photons s}^{-1} \text{ cm}^{-2}$
$E_{K\beta}$	-	$7.08^{+0.03}_{-0.03}$	keV
χ^2	1397	1387	
d-o-f	1580	1579	

^a Upper Limit

recent *Chandra* HETG observation of Mrk 3 revealed prominent soft X-ray emission lines from silicon, sulphur and iron (see Section 6.5.2) that will effect the spectrum between 2-3 keV. These residuals are not modelled any further here. A small feature is also clear in the ratios around 7 keV. Given the strength of the iron $K\alpha$ line it is likely that this feature corresponds to an iron $K\beta$ fluorescent emission line. Including iron $K\beta$ in the model improves the fit and is significant at the $\sim 3\sigma$ level ($\Delta\chi^2=10$ for 1 d.o.f). The intrinsic width of the line is fixed at the intrinsic width of the iron $K\alpha$ line, and the line flux is fixed at the correct ratio with respect to the iron $K\alpha$ emission line (10%). The best-fit parameters for the spectral fit that includes the iron $K\beta$ line are given in Table 4.2 (Model B). The apparent feature in the PN spectrum around 8 keV in Figure 4.9 is not mirrored in either of the MOS spectra, suggesting that this is unlikely to be a real feature.

4.4 Discussion

4.4.1 The impact of heavy absorption on NGC 7582 and Mrk 3

The modelling presented earlier in this chapter reveals the strong inherent similarities between the hard X-ray spectra of NGC 7582 and Mrk 3. Both sources have qualitatively similar spectral forms over the 2.5-10 keV range and this manifests itself in the close resemblance between the spectral models that provide a good description of the hard X-ray spectra in each case. Both sources exhibit heavy line-of-sight X-ray absorption ($0.5\text{-}1.5 \times 10^{24} \text{ cm}^{-2}$), which strongly limits the energy range over which the underlying X-ray continuum is observed and enhances the prominence of the observed continuum reprocessing features. The observed spectral shape is sensitive to comparatively small changes in the level of the absorption. This effect is highlighted by Figure 4.10; the $\sim 80\%$ greater absorbing column observed in Mrk 3 results in a significantly different spectral shape between 4-6 keV, and above ~ 7 keV,

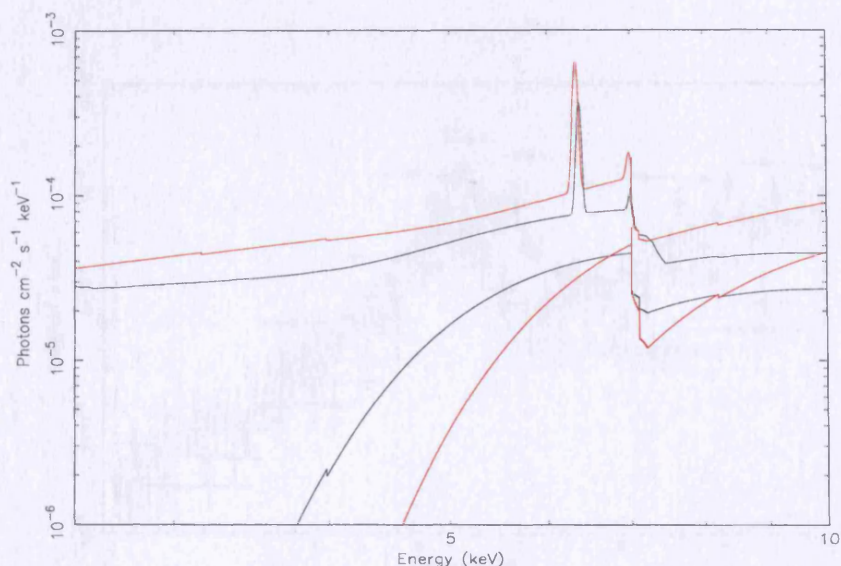


Figure 4.10: A comparison of the absorption in NGC 7582 (Black) and Mrk 3 (Red). *Upper lines:* The total model (including the absorbed continuum, Compton reflection continuum and iron $K\alpha$ and $K\beta$ emission line). *Lower lines:* The associated absorbed continuum component.

in comparison with the spectrum of NGC 7582.

In general, the contribution of Compton reflection to the X-ray spectra of AGN increases as one examines more heavily obscured sources, until the Compton reflection continuum dominates the hard X-ray spectrum. However, the column density of the absorption is not the only determining factor for the observed X-ray spectral form, as chapter 3 highlights. The ionization state of the absorbing material can have a significant impact on the observed continuum shape. In both NGC 7582 and Mrk 3 the dominant absorption arises in neutral gas, in contrast to the principal absorption observed in NGC 4151, which arises in primarily in strongly photoionized material. The presence of a warm absorber in NGC 7582 and Mrk 3, with similar properties to that observed in NGC 4151, is not ruled out by the analysis presented here. The heavy warm absorber in NGC 4151 only impacts on the continuum below ~ 5 keV and it is possible that, if such absorption is present in NGC 7582 and Mrk 3, then its effects will not be observed due to the overwhelming cut-off imposed on the X-ray spectrum by the heavy cold absorption.

The heavy neutral absorption in these, and similar, objects also has a significant impact on the observed X-ray variability. In general, the greater the X-ray absorption the more diluted the intrinsic underlying continuum variability will become, since the Compton reflection component is only expected to vary slowly (*i.e.* on timescales of a year or more). Both NGC 7582 and Mrk 3 show significant variability however, the properties of this variability are markedly different in the two sources. A comparison of the variability properties of NGC 7582 and Mrk 3, in terms of the effect of the heavy absorption, is complicated by the fact that the two sources have extremely different underlying continuum variability properties.

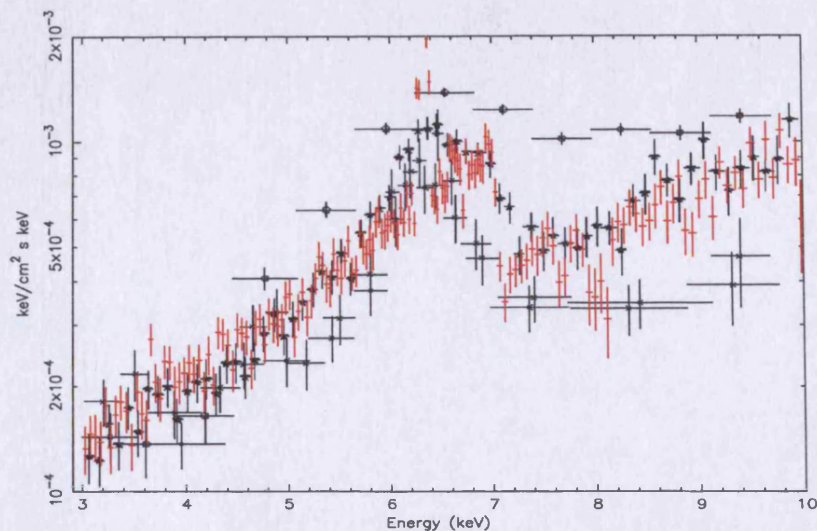


Figure 4.11: Unfolded spectra of Mrk 3 from *Ginga* (open circles), *ASCA* (crosses), *BeppoSAX* (filled stars) and *XMM-Newton* (red data). The unfolded spectra span more than a decade of observations and highlight the spectral variability observed in Mrk 3

Spectral variability

Mrk 3 shows significant variability only on long timescales (a factor of 2 change in ~ 100 days is the swiftest observed variability in Mrk 3; Georgantopoulos *et al.* 1999), as illustrated by the remarkably constant flux recorded over the 10^5 s of the *XMM-Newton* observation (Figure 4.7). Previous observations with *Ginga*, *ASCA* and *BeppoSAX* have revealed that the flux variability of Mrk 3 is coupled with considerable spectral variability. Figure 4.11 shows unfolded spectra from observations of Mrk 3 from *Ginga*, *ASCA* and *BeppoSAX* over a period of eight years (Cappi *et al.* 1999). By way of a comparison with the previous data, the unfolded spectrum obtained from the best-fit (Table 4.2, Model B) to the *XMM-Newton* EPIC spectra is overlaid on this plot. The unfolded spectra of Mrk 3, which span more than a decade, highlight the spectral variability in this source. Little variability is evident below ~ 5 keV (Cappi *et al.* 1999; Griffiths *et al.* 1998), which is the point at which the hard X-ray continuum becomes too cut-off to have any effect on the X-ray spectrum (Figure 4.10). Above ~ 5 keV the scale of the observed variability increases with energy, as the impact of the X-ray absorption on the underlying hard X-ray continuum decreases. By ~ 7 keV the heavy X-ray absorption has negligible impact on the underlying continuum and the amplitude of the observed variability saturates at the level of the variability of the continuum. Above ~ 7 keV the amplitude of the variability remains approximately constant with energy.

As an aside from the more general discussion, Figure 4.11 highlights the similarity between the unfolded spectra from the observations of Mrk 3 by *BeppoSAX* and *XMM-Newton*. This is due in part to Mrk 3 having a similar flux level in each of the observations however, the unfolded spectrum is a model-

dependent tool, and a large portion of the similarity undoubtedly arises because much of the modelling of the *XMM-Newton* spectrum (Section 4.3.2), particularly regarding the details of the very hard (>10 keV) underlying power-law continuum, was based on the *BeppoSAX* analysis (Cappi *et al.* 1999). One of the major differences between the two spectra is caused by the significantly better spectral resolution of *XMM-Newton*. This clearly manifests itself in the considerably narrower appearance of the iron $K\alpha$ line, and the sharper appearance of the iron K edge, in the unfolded spectrum from *XMM-Newton*, relative to the *BeppoSAX* spectrum.

In stark contrast to Mrk 3, the variability observed in NGC 7582 is both extremely rapid and large-scale (Figure 4.3 *Upper Panel*). This rapid variability is not accompanied by a correlated rapid change in the 2-5/5-10 keV softness ratio, demonstrating that NGC 7582 shows little spectral variability on short timescales. The lack of any clear spectral variability between the 2-5 keV and 5-10 keV bands suggests that the hard X-ray continuum has considerable influence on the 2-5 keV spectrum. The absorption used to model the *XMM-Newton* EPIC spectra of NGC 7582 is somewhat greater than the column densities found from previous observations ($8 \times 10^{23} \text{ cm}^{-2}$ cf. $8 \times 10^{22} \text{ cm}^{-2}$, Schmidt *et al.* 1998; $1.24 \times 10^{23} \text{ cm}^{-2}$, Xue *et al.* 1999), however the absorbed hard X-ray continuum does have a considerable impact on the spectrum below ~ 5 keV (Figure 4.10), consistent with the softness ratio variability properties.

Column density variations

In addition to the intrinsic continuum variability, significant changes in absorption will imprint an extra variability component on both the source flux and on the properties of the X-ray spectrum. There is evidence, based on spectral fits to *Ginga*, *ASCA* and *BeppoSAX* data, for column density variations of about a factor of two in Mrk 3 on year-long timescales ($0.6\text{-}1.4 \times 10^{24} \text{ cm}^{-2}$; e.g. Awaki *et al.* 1990; Cappi *et al.* 1999). The spectral variability observed in Mrk 3, particularly over the $\sim 5\text{-}7$ keV range, may well be associated with slow variations in the absorbing column in addition to the intrinsic variability of the underlying continuum. However, the evidence for column density variations in Mrk 3 is far from conclusive, particularly with regard to the low column density measurements resulting from the *Ginga* and *ASCA* spectra, due to a combination of poor signal-to-noise data and poor continuum modelling. NGC 7582, in addition to the short timescale variability discussed in the previous section, is also known to exhibit longer timescale variability. A factor of 2 decrease in flux was observed with *ASCA* over a period of $\sim 10^5$ s (Xue *et al.* 1999) and longer timescale variations have been observed between *RXTE* and *ASCA* observations (Turner *et al.* 2000). This variability may be related to absorption changes however, too few high quality observations currently exist to support any conclusions regarding column density changes in NGC 7582.

4.4.2 The implications of Compton reflection

Seyfert 2 galaxies with flat hard X-ray spectra, such as NGC 7582 and Mrk 3, provide strong evidence for a neutral (or near neutral) Compton reflection continuum in obscured AGN as a whole. In such sources, the putative molecular torus may serve as a reprocessing site for the hard X-ray continuum. Furthermore, for an inclined configuration, it is plausible that the geometry reveals a clear view of the far-side inner wall of the torus, while obscuring the direct continuum and it follows from this geometry that the observed neutral Compton reflection, at least in the sources presented here, may originate from this “far-wall” location.

As discussed in the previous section, the relative dominance of the Compton reflection continuum in NGC 7582 and Mrk 3 is entirely due to the heavy line-of-sight X-ray absorption that impinges on the underlying continuum. A comparison of the 2-10 keV luminosity contained in the Compton reflection component reveals that both NGC 7592 and Mrk 3 have similar strength Compton reflection components, relative to their intrinsic unabsorbed 2-10 keV X-ray continuum luminosity ($\sim 8\%$ and $\sim 5\%$ respectively). Furthermore, the relative strength of the Compton reflection in both these sources is extremely comparable to the relative strength of the Compton reflection observed in NGC 4151 [which ranges between $\sim 2\%$ (*BeppoSAX* 1999) and $\sim 11\%$ (*XMM-Newton* 2000) of the 2-10 keV luminosity of the underlying hard X-ray continuum]. This is highly suggestive of a similar physical origin for the Compton reflection in each of these three sources and hints that all heavily obscured AGN may exhibit a Compton reflection component with a luminosity of between a few and ten percent of the time-averaged, unabsorbed, hard X-ray continuum luminosity. Interestingly, X-ray spectra from recent observations on NGC 5548 with *XMM-Newton* and *BeppoSAX* require a neutral Compton reflection component whose intrinsic 2-10 keV luminosity amounts to 9% of the unabsorbed 2-10 keV hard X-ray continuum luminosity (Pounds, priv comm, 2002). This may indicate that a cold Compton reflection component of around this relative strength is a ubiquitous component in the X-ray spectra of all types of AGN, even in sources with little direct absorption.

Ionized Compton reflection

Of the three sources discussed so far, NGC 7582 is the only one to show any evidence for ionization of the material responsible for the Compton reflection. The energy of the iron K edge is a considerably more sensitive probe of the ionization state of the material, particularly for low ionization states, than the associated iron $K\alpha$ line emission and the detection of a deep iron K edge at an energy of 7.2 keV in NGC 7582 is a strong indication of the presence of ionized material, when compared to the energy of an iron K edge originating in neutral material (7.08 keV). The edge energy observed in NGC 7582 corresponds to a range of rest frame iron ionization states of Fe III-Fe V. Under the assumption that NGC 7582 and NGC 4151 are intrinsically similar, and hence that NGC 7582 possesses a warm absorber

similar to that seen in NGC 4151 (albeit one whose effects are unobservable in the X-ray spectrum due to the effects of the extremely heavy cold absorption), a comparison between the ionization states of iron found for the warm absorber (typically Fe XVI-Fe XXI) and those found in the ionized reflector suggests that the material responsible for the Compton reflection component is either considerably more distant than the warm absorber (by a factor of ~ 30), or that the reflecting material is considerably denser than the warm absorber (by ~ 1000 times). Interpreting the warm absorber as a wind off the inner edge of the obscuring torus (Krolik & Kriss 2001) and associating the torus with the material responsible for the Compton reflection (Antonucci 1993; Antonucci & Miller 1985), suggests that an decrease in density is responsible for the increase in ionization state as you move from the torus to the warm absorber. Given a density of $\sim 4 \times 10^4 \text{ cm}^{-3}$ in the warm absorber (Section 3.5.1), this interpretation implies a density of $\sim 4 \times 10^7 \text{ cm}^{-3}$ for the region of the torus responsible for the ionized Compton reflection in NGC 7582.

4.4.3 Details of the iron $K\alpha$ line

The apparent strength of the iron $K\alpha$ line in the X-ray spectrum of heavily obscured AGN can be significantly enhanced if the X-ray absorption is sufficiently heavy. The intrinsic line properties (*i.e.* the line centroid energy, line profile and line flux) are not affected however, significant suppression of the intrinsic hard X-ray power-law continuum around the region of the line energy will boost the measured equivalent width of the line relative to the observed total continuum. Relative to the total underlying continuum emission, the equivalent widths of the iron $K\alpha$ lines in NGC 7582 and Mrk 3 are 255 eV and 360 eV, respectively; ~ 1.5 -2 times greater than the equivalent width of the iron line observed with *XMM-Newton* in NGC 4151. However, both of these sources have X-ray absorption which strongly impacts on the X-ray spectrum around 6.4 keV and as a result these EQWs can be misleading relative to less absorbed sources. A better measure of the iron $K\alpha$ line strength is the EQW with respect to the Compton reflection component. This measure is particularly useful in determining whether the observed iron $K\alpha$ line can be produced in the same material responsible for the Compton reflection. Matt, Brandt & Fabian (1996) predicted that neutral Compton reflection from a solar abundance, Compton-thick, molecular torus should have an associated iron $K\alpha$ line with an EQW, relative to the Compton reflection continuum, of ~ 1 keV (Figure 1.4). The iron line EQW from a neutral torus can be considerably reduced either by reducing the opening angle of the torus and/or reducing the iron abundance in the torus material.

The equivalent widths of the iron $K\alpha$ lines in NGC 7582 and Mrk 3, relative to the Compton reflection continuum, are both ~ 520 eV; somewhat smaller than the predicted, ~ 1 keV. By comparison, the equivalent width of the iron $K\alpha$ line observed in the *XMM-Newton* observation of NGC 4151 is ~ 1 keV, however there is strong evidence for an iron abundance of about twice solar in NGC 4151 (Section 3.8.4). These EQWs are well within the levels predicted by Compton reflection from a cold, Compton-thick torus suggesting that the same material may well be responsible for producing both the iron line and the Compton reflection continuum, and may even imply a somewhat smaller opening angle for the tori in AGN than the current predictions assume. The line profiles for both NGC 7582 and Mrk 3 are well mod-

elled by a Gaussian line profile that is consistent with being intrinsically narrow, supporting an origin for the line emission in material distant from the central source.

4.5 Conclusions from NGC 7582 and Mrk 3

This chapter presents the detailed spectroscopic analysis of recent *XMM-Newton* observations of two heavily obscured Seyfert 2 galaxies, NGC 7582 and Mrk 3, with the focus of the chapter resting on the impact of Compton reflection and heavy absorption. The main results are:

- The 2.5-10 keV X-ray spectra from NGC 7582 and Mrk 3 are both well modelled by a simple model incorporating a heavily absorbed power-law continuum, strong Compton reflection and strong iron reprocessing features. In both sources the X-ray spectrum is dominated by the Compton reflection component, resulting in an extremely flat 2-10 keV spectral form.
- The X-ray spectra of NGC 7582 and Mrk 3 do not rule out the presence of a similar warm absorber to that seen in NGC 4151, because the heavy cold absorption impacts on the X-ray spectrum at considerably higher energies than the warm absorber is expected to (*i.e.* >5 keV).
- The 2-10 keV luminosity of the Compton reflection in NGC 7582 and Mrk3 corresponds, respectively, to $\sim 8\%$ and $\sim 5\%$ of the unabsorbed continuum luminosity in this range. The similarity of these values to the range of values found for NGC 4151 (2%-11%) and NGC 5548 ($\sim 9\%$) implies that a cold Compton reflection component of around this strength may be a ubiquitous component in the X-ray spectra of all types of AGN, even in sources with little direct absorption.
- The observed iron edge in the X-ray spectrum of NGC 7582 occurs at an energy of 7.2 keV, providing strong evidence for Compton reflection from mildly ionised material in this object. The corresponding iron ionization states for this material are in the range of Fe III-Fe V. From this detection, it is clear that the iron edge is considerably more sensitive to the ionization state of reprocessing material, particularly to low ionization states, than the associated iron $K\alpha$ line energy. Making the assumption that NGC 7582 and NGC 4151 are intrinsically similar (*i.e.* that NGC 7582 possesses a warm absorber similar to that seen in NGC 4151) a comparison of the ionization states of iron found in the warm absorber (typically Fe XVI-FeXXI) and those found in the ionized reflector suggests that the ionized reflecting material in NGC 7582 is either a factor of ~ 30 times more distant or, more likely, that the reflecting material in NGC 7582 is $\sim 10^3$ times denser than the material that constitutes the heavy warm absorber observed directly in NGC 4151.
- NGC 7582 shows extremely rapid, large amplitude, variability ($\sim 70_{-40}^{+80}\%$ in a period of ~ 400 seconds!) as well as considerable long-term variability (which can also be seen in Mrk 3). The extremely rapid variability makes NGC 7582 a prime target for considerably more intensive X-ray spectral and timing studies in the future.

Chapter 5

The hard X-ray spectrum of NGC 4945

5.1 Overview: Increasing the absorption and confusing the spectrum!

This chapter focuses on the interpretation of the X-ray spectrum of the nearby Seyfert 2 galaxy NGC 4945, focusing on its active nucleus and the immediate surroundings (within ~ 1 kpc of the AGN). Utilizing the complementary capabilities of *XMM-Newton* and *Chandra*, a detailed imaging and spectral study reveals a complex nuclear region with many distinct components including a predominantly hard, but partially resolved, nuclear source and a spectrally soft, conically shaped X-ray “plume” that extends $30''$ (500 pc) to the northwest of the nucleus. The direct view of the AGN is blocked below ~ 10 keV by extremely heavy line-of-sight absorption and, as a consequence of this, the X-ray spectrum from the AGN is dominated by neutral Compton reflection and a 6.4 keV fluorescent iron $K\alpha$ line. The AGN spectrum is strongly confused however, by multi-temperature thermal emission associated with a nuclear starburst, considerably complicating the analysis of the AGN spectrum. The excellent spatial resolution of *Chandra* is used to extract individual spectra corresponding to the AGN core and the surrounding nuclear starburst/X-ray plume. Despite the fact that these relatively poor signal-to-noise spectra are not able to constrain the models particularly well, they are used to define a gross spectral model for each region. These are then combined into a single spectral model and jointly fit to both the *XMM-Newton* and *Chandra* data. The superior throughput of *XMM-Newton* results in spectra of sufficient quality to tightly constrain the properties of the individual spectral components identified by *Chandra*.

The chapter is organised as follows. Section 5.2 describes some of the detailed background work regarding the X-ray study of NGC 4945. Section 5.3 presents the details of the *Chandra* and *XMM-Newton* observations and data reduction. Section 5.4 discusses the imaging analysis of both datasets. The spectral analysis is dealt with in Section 5.5. Section 5.6 discusses the implications of the analysis, particularly in the context of the unified AGN paradigm.

5.2 NGC 4945

NGC 4945 is a nearby edge-on ($i \sim 78^\circ$; Ott 1995) spiral galaxy (type SBcd or SABcd), believed to be a member of the Centaurus group (Hesser *et al.* 1984), at a distance of between 3.7 Mpc and 8.1 Mpc. Near infra-red observations have revealed the nuclear region of NGC 4945 to contain a powerful, yet visually obscured starburst region with a ~ 200 pc ($\sim 10''$) ring morphology (Moorwood *et al.* 1996) and a total infrared luminosity (8-1000 μm) of $2.2 \times 10^{10} L_\odot$ (Spoon *et al.* 2000).

Although much of the central activity can be explained in terms of a nuclear starburst, the presence of an AGN in NGC 4945 has been confirmed by the detection of a luminous and variable hard X-ray source coincident with the centre of the galaxy (Iwasawa *et al.* 1993; Guainazzi *et al.* 2000). In fact, NGC 4945 harbours the brightest known Seyfert 2 nucleus at 100 keV (Done, Madejski & Smith 1996), but extremely heavy obscuration cuts-off the direct AGN continuum at energies below ~ 10 keV (Guainazzi *et al.* 2000; Zycki *et al.* 2000). The measured X-ray column density ($\sim 4 \times 10^{24}$ atom cm^{-2}) places it on the threshold of being a Compton-thick Seyfert 2. After correctly accounting for the effects of Compton scattering in the absorbing material (Matt *et al.* 1999), the inferred intrinsic X-ray (0.1-200 keV) luminosity is $\sim 1.8 \times 10^{43}$ erg s^{-1} (Guainazzi *et al.* 2000). The 0.5-10 keV X-ray spectrum of the AGN is comprised of both thermal emission associated with a nuclear starburst and emission generated through the reprocessing of the AGN continuum emission (Guainazzi *et al.* 2000).

The dense clouds that envelope the nuclear region produce a rich variety of molecular lines (Curran *et al.* 2001) including H_2O megamaser emission, which requires an edge-on inner disk geometry (Greenhill, Moran & Herrnstein 1997). The megamaser emission provides a tight constraint on the mass of the central black hole, $M_{BH} \approx 1.4 \times 10^6 M_\odot$, implying that the AGN is radiating at up to 60% of its Eddington luminosity.

Infrared and optical observations of NGC 4945 have also revealed the presence of a conical cavity, attributed to a starburst-driven superwind, protruding above the disk of the galaxy (Chen & Huang 1997; Moorwood *et al.* 1996). Extended line-emitting gas, co-spatial with the conical cavity, has been detected in outflow along the galaxy's minor-axis, despite the heavy obscuration at optical wavelengths, and this is attributed to the interaction between the superwind and the surrounding medium (Heckman, Armus & Miley 1990). The low spatial resolution of the currently published data has mitigated against the detection of the superwind in X-rays, although Guainazzi *et al.* (2000) suggest that at least part of the soft X-ray emission from NGC 4945 may originate in this component.

5.3 The observations

5.3.1 The *Chandra* observation

The archival *Chandra* data were obtained from the UK mirror of the *Chandra* X-ray Center data archive, maintained by the Leicester Data Archive Service. The *Chandra* observation itself was performed on January 27th and 28th, 2000, resulting in a total exposure of 50 ks with the ACIS-S at the prime focus. The data reduction and analysis of this dataset was performed using version 2.1 of the *Chandra* Interactive Analysis of Observations (CIAO) software, and incorporated many of the standard analysis procedures available online from cxc.harvard.edu/ciao. The data were initially filtered to remove all events outside the 0.3-10 keV energy range. The full field light-curve revealed heavy contamination of the observation by background flaring. The removal of all times for which the total detector count rate exceeded 8 counts s⁻¹ dramatically reduced the background in the S3 chip, leaving a corrected event-list containing 33.1 ks of “good” data.

5.3.2 The *XMM-Newton* observation

NGC 4945 was observed with *XMM-Newton* during orbit 205 (January 21st, 2001) for ~24 ks as part of the mission guaranteed time programme. The EPIC MOS and PN instruments were operated in Full Window Mode (FWM), with the medium filter in place for the full duration of the observation. The raw data were processed with the public release version of the *XMM-Newton* Science Analysis System (SAS) v5.2 standard processing chains. After filtering for data flagged as bad, X-ray events corresponding to pattern 0-12 for the MOS cameras and pattern 0-4 for the PN camera (single and double pixel events only) were accepted. Investigation of the full field count rate revealed no significant background flaring episodes during the observation. The effective exposure times for the MOS and PN cameras were 22.2 ks and 19.2 ks, respectively. Images, spectra and corresponding background information were extracted with the SAS task *xmmselect*.

5.4 Joint imaging with *Chandra* and *XMM-Newton*

XMM-Newton and *Chandra* images were extracted for a 2' square region centred on the nucleus of NGC 4945, revealing a wealth of detail in the nuclear region including a predominantly hard nuclear source and a soft X-ray “plume” extending to the northwest of the nuclear source. Figure 5.4 Panels (a)-(c), show high spatial resolution energy-coded X-ray images from the *Chandra* ACIS-S detector, while Panel (d) shows an ‘X-ray colour’ image from the co-added *XMM-Newton* EPIC cameras. Whereas the nuclear source appears point-like with *XMM-Newton*, the *Chandra* imaging partially resolves the

emission centred on the active nucleus (Figure 5.4 Panel (c)). The nuclear point source is revealed as an extremely hard source by both the *Chandra* hard band image and the *XMM-Newton* X-ray colour image. Similarly to NGC 7582 and Mrk 3, the spectral hardness of NGC 4945 is almost certainly due to heavy line-of-sight obscuration. Both *XMM-Newton* and *Chandra* clearly resolve the X-ray plume, establishing its orientation and extent along the minor axis of the galaxy ($30'' = 500$ pc, NW) and also its intrinsic spectral softness (Figure 5.4 Panels (a),(b),(d)). The medium band *Chandra* image reveals the X-ray plume to have a limb-brightened morphology, qualitatively similar to the morphology of the X-ray plume seen in NGC 253 (Strickland *et al.* 2000).

5.5 Joint spectroscopy with *Chandra* and *XMM-Newton*

The high spatial resolution afforded by *Chandra* resolves several of the major components that comprise the total X-ray emission from the nuclear region of NGC 4945. However, the relatively low count rate means the *Chandra* data cannot be used to place tight constraints on the spectral form of these components. Conversely, despite the greater count rate, the lower angular resolution of *XMM-Newton* gives rise to some spatial confusion, which complicates the identification and spectral modelling of the components that comprise the nuclear region. Fortunately, the *joint* analysis of the *Chandra* and *XMM-Newton* spectra removes many of these limitations.

Separate *Chandra* ACIS-S spectra were extracted for the AGN and the extended emission components and these spectra were modelled independently. The identified spectral models were then combined into a single composite spectral model. Finally, the *XMM-Newton* data were included with both the *Chandra* datasets and a combined fit to all the spectra was produced with the composite spectral model. The combined *Chandra* plus *XMM-Newton* fit provides the tightest constraints on the individual model parameters. All the source spectra presented in this chapter, as with the spectra elsewhere in this thesis, are grouped to a minimum of 20 counts per bin to allow the use of χ^2 minimisation techniques.

5.5.1 The *Chandra* AGN spectrum

The spectrum of the point-like nuclear source (which, initially, was assumed to be associated predominantly with the AGN in NGC 4945) was derived from the *Chandra* event list using a circular extraction region with a 6 pixel radius ($3''$) centred on the peak of the X-ray emission, at $13^{\text{h}}05^{\text{m}}27.5^{\text{s}}$, $-49^{\circ}28'05''$ (J2000). The corresponding background spectrum was taken from a local source-free region. The resulting spectrum contains ~ 750 counts (after background subtraction) with no significant signal below 1.5 keV.

In several well studied Seyfert 2 galaxies, with column densities in excess of a few $\times 10^{23}$ atoms cm^{-2} ,

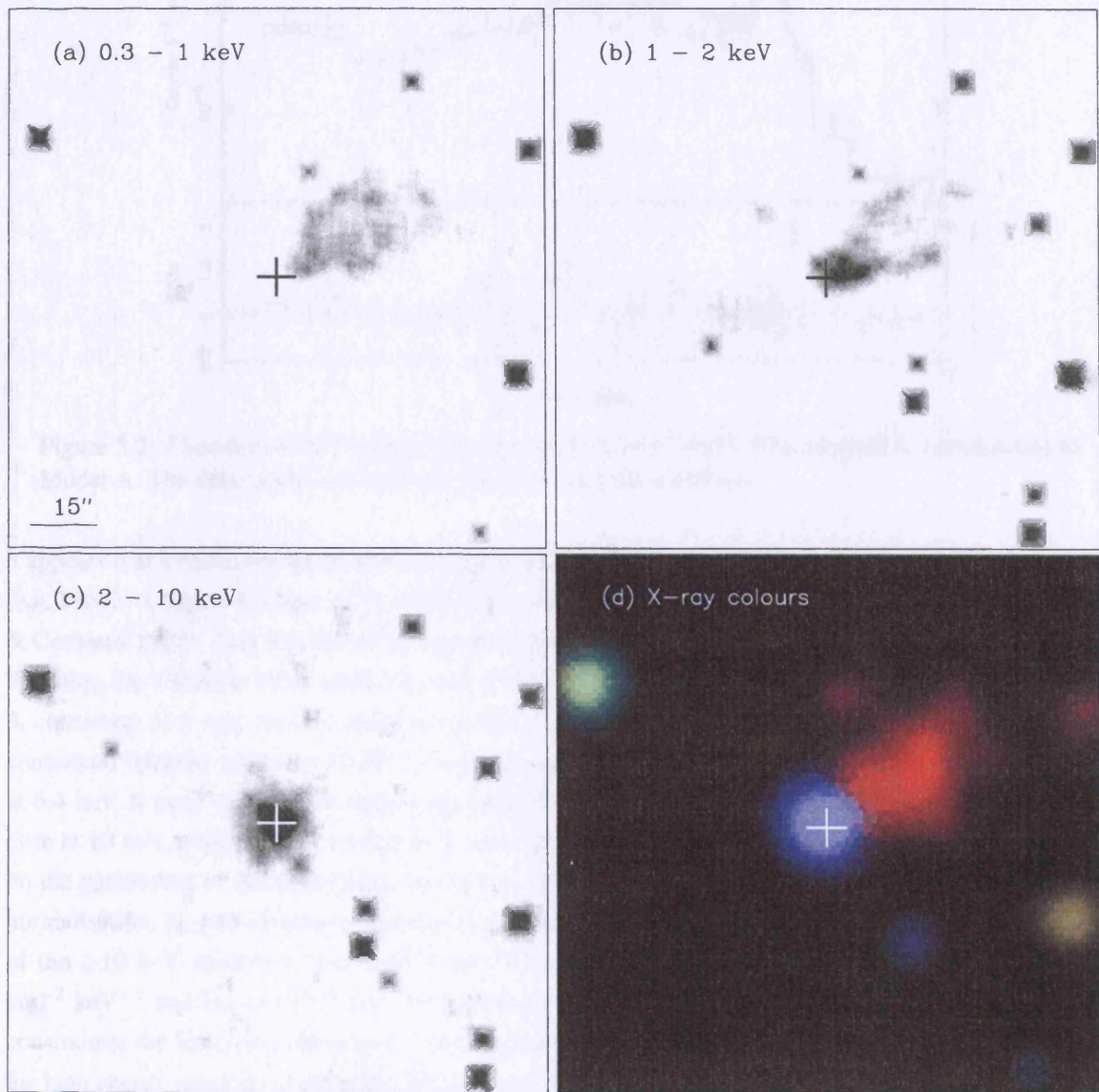


Figure 5.1: X-ray Images of the nuclear region of NGC 4945. *Panels a-c:* *Chandra* X-ray images corresponding to (a) the soft (0.3-1 keV) band; (b) the medium (1-2 keV) band and (c) the hard (2-10 keV) band. *Panel d:* *XMM-Newton* ‘X-ray colour’ image. Red, green and blue correspond to the soft, medium and hard X-ray bands defined above. All the images are $2'$ on a side. The *Chandra* images have been smoothed with an adaptive ‘boxcar’ filter set to encompass ≥ 10 counts per box, or to have a half-width of 5 pixels. Non-adaptive, Gaussian smoothing ($2''$ HWHM) was applied to the *XMM-Newton* image.

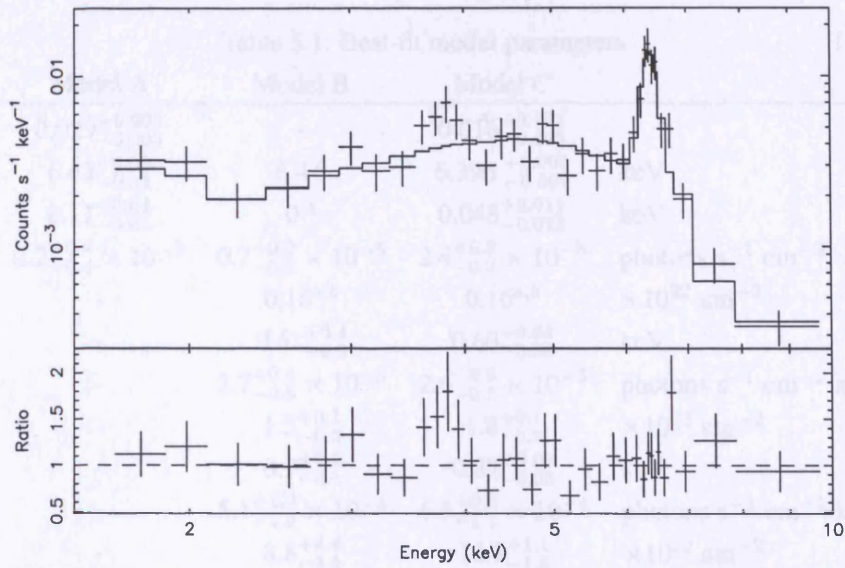


Figure 5.2: *Chandra* ACIS-S spectrum of the AGN in NGC 4945. The spectral fit corresponds to Model A. The data/model residuals are plotted below the spectrum.

it appears that a relatively unabsorbed Compton reflection component dominates the 2-10 keV spectrum (*e.g.* Mrk 3 - Chapter 4, Cappi *et al.* 1999, Sako *et al.* 2000; NGC 7582 - Chapter 4; NGC 3281 - Vignali & Comastri 2002). This was the initial hypothesis in the following analysis of NGC 4945 and was tested by fitting the *Chandra* AGN spectrum with a model very similar to that used for NGC 7582 and Mrk 3, consisting of a very heavily absorbed power-law continuum, unabsorbed Compton reflection of the continuum (**pexrav** model in XSPEC; Magdziarz & Zdziarski 1995) and an iron $K\alpha$ fluorescence line at 6.4 keV. It turns out that the underlying hard X-ray continuum in this model has little direct impact even at 10 keV, implying that neither the *Chandra* or *XMM-Newton* data can provide useful constraints on the parameters of the underlying continuum. Thus, the continuum characteristics (photon index, Γ , normalisation, A_1 and absorbing column, N_H) were fixed at the values consistent with previous analyses of the >10 keV spectrum from both *BeppoSAX* and *RXTE*, specifically, $\Gamma=1.55$, $A_1=0.1$ photon s^{-1} cm^{-2} keV^{-1} and $N_H=4\times 10^{24}$ cm^{-2} (Guainazzi *et al.* 2000; Zycki *et al.* 2000). In addition to these constraints, the following restrictions were imposed: The metal abundances were fixed at solar values, the high energy spectral cut-off set at 200 keV, $\cos(i)$ was fixed at 0.5 and the relative reflection parameter (R) was initially constrained to lie in the range 0-2.

This model, with both the R parameter and the energy, intrinsic width and normalisation of the iron $K\alpha$ line as free parameters, provides a good fit to the *Chandra* spectrum ($\chi^2=32$ for 29 d.o.f) as illustrated in Figure 5.2. The best-fit parameter values are given in Table 5.1 (Model A). Modelling the *Chandra* spectrum in terms of a heavily absorbed direct continuum component (but with N_H an order of magnitude smaller than assumed above) plus a relatively unabsorbed scattered power-law component (Guainazzi *et al.* 2000) yields a considerably worse fit ($\chi^2=51.1$ for 29 d.o.f). The positive fit residuals around 3.8 keV (Figure 5.2) are not strongly significant, preventing any clear interpretation of these residuals

Table 5.1: Best-fit model parameters

Parameter	Model A	Model B	Model C	
R	$0.029^{+0.003}_{-0.003}$	-	$0.016^{+0.002}_{-0.002}$	
$E_{FeK\alpha}$	$6.42^{+0.03}_{-0.03}$	6.4^a	$6.396^{+0.005}_{-0.007}$	keV
$\sigma_{FeK\alpha}$	$0.11^{+0.04}_{-0.03}$	0^a	$0.048^{+0.011}_{-0.013}$	keV
$K_{FeK\alpha}$	$2.2^{+0.4}_{-0.4} \times 10^{-5}$	$0.7^{+0.2}_{-0.3} \times 10^{-5}$	$2.4^{+0.2}_{-0.2} \times 10^{-5}$	photons $s^{-1} cm^{-2}$
$N_{H,1}$	-	$0.16^{a,b}$	$0.16^{a,b}$	$\times 10^{22} cm^{-2}$
kT_1	-	$0.61^{+0.4}_{-0.9}$	$0.60^{+0.03}_{-0.03}$	keV
K_1	-	$2.7^{+0.4}_{-0.5} \times 10^{-5}$	$2.6^{+0.3}_{-0.3} \times 10^{-5}$	photons $s^{-1} cm^{-2} keV^{-1}$
$N_{H,2}$	-	$1.5^{+0.1}_{-0.3}$	$1.8^{+0.1}_{-0.2}$	$\times 10^{22} cm^{-2}$
kT_2	-	$0.9^{+0.1}_{-0.1}$	$0.87^{+0.08}_{-0.08}$	keV
K_2	-	$5.1^{+1.0}_{-1.2} \times 10^{-4}$	$6.5^{+0.8}_{-1.1} \times 10^{-4}$	photons $s^{-1} cm^{-2} keV^{-1}$
$N_{H,3}$	-	$8.8^{+4.4}_{-3.5}$	$12.1^{+1.1}_{-1.6}$	$\times 10^{22} cm^{-2}$
kT_3	-	8.7^c	$6.0^{+1.1}_{-0.8}$	keV
K_3	-	$4.5^{+1.6}_{-1.2} \times 10^{-4}$	$6.4^{+1.1}_{-0.9} \times 10^{-4}$	photons $s^{-1} cm^{-2} keV^{-1}$
χ^2	32.3	81	290	
d-o-f	29	67	269	

^a Fixed parameter^b Galactic column density^c Unconstrained parameter

as a real feature, however they may hint at some contamination of the *Chandra* AGN spectrum by a nuclear starburst component. Our modelling of the composite *XMM-Newton* spectrum incorporates the possibility that these residuals constitute a real feature in a straightforward fashion (see Section 5.5.3).

5.5.2 The *Chandra* starburst/X-ray plume spectrum

The *Chandra* spectrum of the extended nuclear X-ray emission, encompassing the resolved nuclear starburst component and the X-ray plume structure, was constructed using an elliptical extraction region centred on $13^h05^m25.5^s$, $-49^\circ27'54''$ (J2000), with the major axis aligned along a position angle of 120° , a semi-major axis of $30.5''$ and a semi-minor axis of $13.4''$. The AGN component was suppressed by excluding the region within $3''$ of the nucleus. The resulting spectrum (after background subtraction using a local source-free region) contains ~ 1600 counts. *Chandra* is capable of resolving the starburst region from the X-ray plume, but here I have chosen to utilize the better signal-to-noise of the combined spectrum. Taking the published results for the starburst and X-ray plume in NGC 253 (Pietsch *et al.* 2001) as a starting point, the *Chandra* spectrum was modelled with three, solar abundance, thermal components (**mekal**; Liedahl, Osterheld & Goldstein 1995), each exhibiting different levels of absorption as well as different temperatures and normalisations.

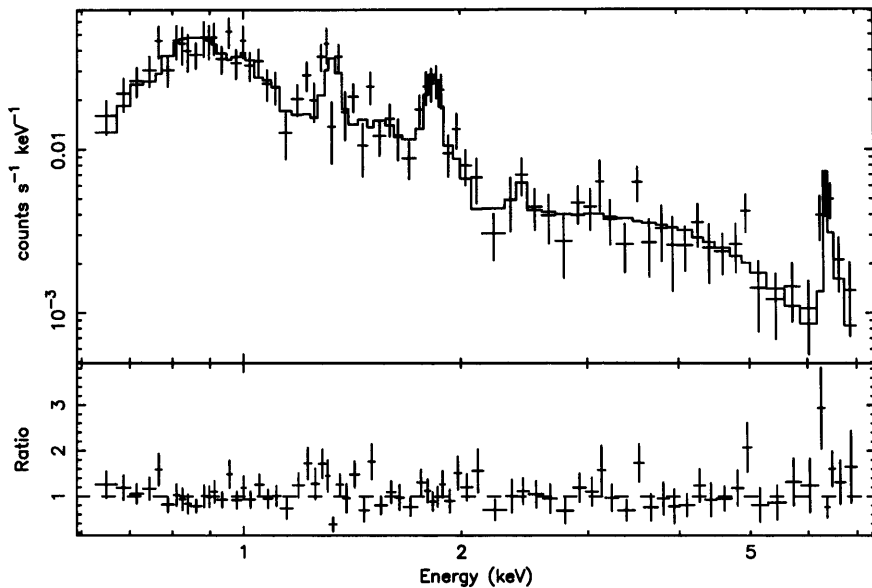


Figure 5.3: *Chandra* ACIS-S spectrum of the starburst/X-ray plume. The spectral fit corresponds to Model B. The data/model residuals are plotted below the spectrum.

This model yields a good fit to most of the observed spectral features, including the significant $K\alpha$ emission from helium-like iron at 6.7 keV. However it does not account for $K\alpha$ emission from neutral iron observed at 6.4 keV. Analysis of the separate starburst and X-ray plume spectra from *Chandra* confirms that both $K\alpha$ emission lines originate entirely from the starburst region. The neutral iron $K\alpha$ emission is modelled by the addition of an intrinsically narrow Gaussian line. This model, now comprising of three thermal components plus an iron $K\alpha$ line, provides a reasonable fit to the data ($\chi^2=89$ for 67 d.o.f, Figure 5.3). The corresponding best-fit model parameters are listed in Table 5.1 (Model B).

5.5.3 Joint fitting of the composite *XMM-Newton* and *Chandra* spectra

The *XMM-Newton* spectra for the combined AGN, starburst and X-ray plume components were extracted using a $30''$ radius circle centred on $13^h05^m28^s$, $-49^\circ28'01''$ (J2000). For both the MOS and PN cameras, a corresponding background spectrum was extracted from a source free region on the same CCD from a $90''$ radius circle. After background subtraction, the MOS spectra contained ~ 1350 counts each, compared to ~ 3500 counts in the PN spectrum. The most up-to-date response matrices available were used (MOS 1 and 2 response matrices from July 2001, PN response matrices from November 2001).

The *XMM-Newton* spectrum was analysed by combining the two models used in the description of the *Chandra* spectra (Models A & B; described in Section 5.5.1 & Section 5.5.2). This composite model yields an excellent fit to the broad-band *XMM-Newton* spectra ($\chi^2=273.5$ for 268 d.o.f). However, an unphysical trade-off between the hottest thermal component and the Compton reflection results in a value of R which is inconsistent with the value found from the *Chandra* AGN spectrum alone (assuming that

this component has not varied significantly over the one-year interval between the two observations - see Section 5.6.1). This problem was addressed by performing *joint spectral fitting* of all the spectral datasets, namely the composite *XMM-Newton* EPIC spectra, the *Chandra* AGN spectrum and the *Chandra* starburst/X-ray plume spectrum. Only the Compton reflection component, the iron line and the hottest thermal component were utilized in fitting the *Chandra* AGN spectrum, whilst only the three thermal components and the iron line were employed in relation to the *Chandra* starburst/X-ray plume spectrum. The spectral model was adapted somewhat by fixing the absorption applied to the softest thermal component at the Galactic value. In addition, the absorption on the Compton reflection component was set to be the same as that applied to the intermediate-temperature thermal component (*i.e.* $N_{H,2}$), since these components propagate along similar lines of sight.

Simultaneous fitting of the composite spectral model described above gives a good fit to all the spectral datasets. The resulting best-fit is shown in Figure 5.4 (only the *XMM-Newton* data are plotted here for simplicity) and the corresponding model parameters are given in Table 5.1 (Model C). The high signal-to-noise of the *XMM-Newton* spectra, relative to the *Chandra* spectra, leads to tighter constraints on all the parameters. The best fit composite model (Figure 5.5) highlights the important contribution of the highest temperature thermal (starburst) component to the 0.5-10 keV spectrum of NGC 4945. In this respect the joint spectral fitting method employed here is particularly valuable since the *Chandra* starburst/outflow spectrum alone has insufficient counts to put any useful limits on the properties of this component.

When data relating solely to the spatially-resolved X-ray plume are extracted (from both the *Chandra* and *XMM-Newton* datasets), the spectrum is found to be extremely soft with few counts above 2 keV. Spectral

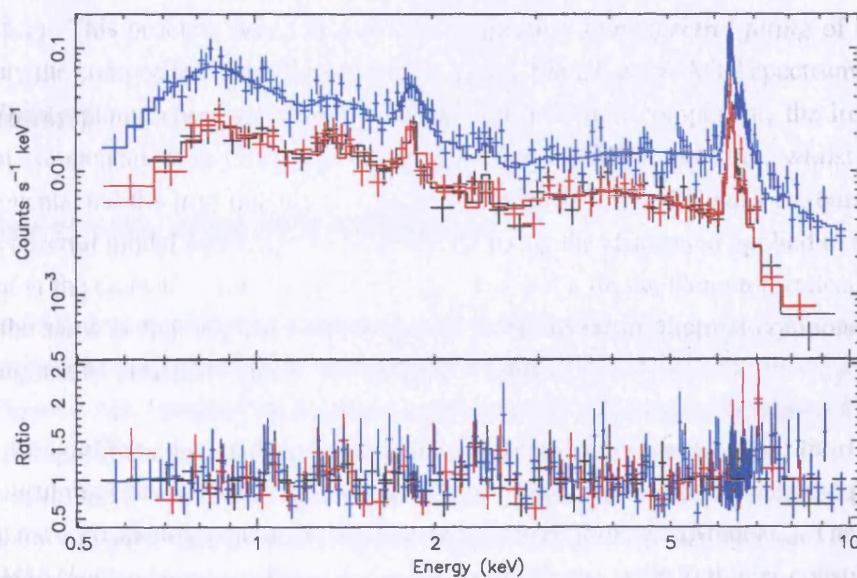


Figure 5.4: *Upper Panel:* *XMM-Newton* EPIC MOS (black and red) and PN (blue) spectra of the extended nuclear region of NGC 4945. The spectra are fit with the composite model (Model C). *Lower Panel* The data/model residuals.

C

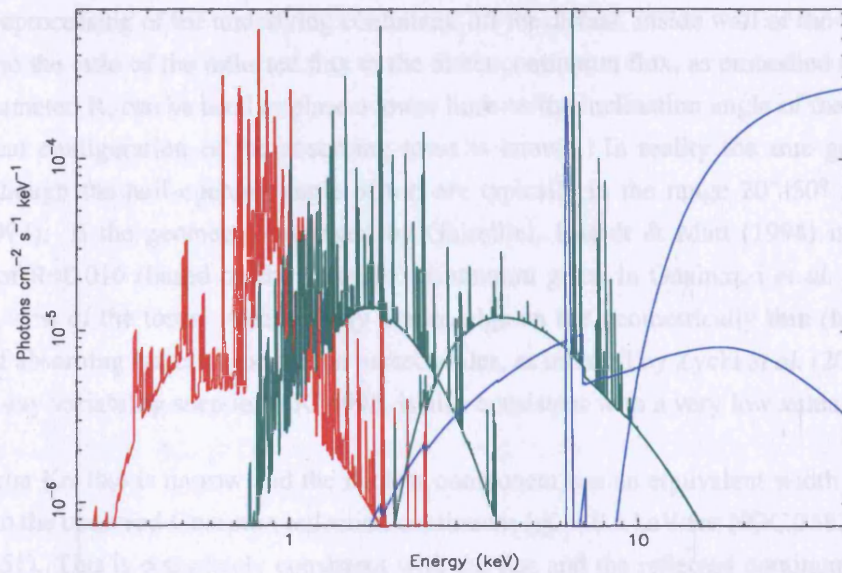


Figure 5.5: The broad-band spectral model for the nuclear region of NGC 4945. The component associated with the X-ray plume is shown in red, the starburst components in green and the AGN components in blue.

fitting using a single temperature *mekal* model, modified by Galactic absorption, gives a temperature and normalisation completely consistent with those of the softest thermal component employed in the composite spectral model (Figure 5.5; Red component), identifying this component with the X-ray plume emission. The two remaining thermal components are attributed to the nuclear starburst (Figure 5.5; Green components).

5.6 Discussion

5.6.1 The reprocessing of the AGN continuum

In the unified model, first proposed by Antonucci (1993), the line-of-sight to an active nucleus viewed at relative high inclination may intercept the surrounding molecular torus and hence be subject to significant obscuration (Figure 1.10). Previous observations testify to a near edge-on configuration for the inner disk in NGC 4945 (Greenhill, Moran & Herrnstein 1997) and a very high line-of-sight column density to its active nucleus (Guainazzi *et al.* 2000; Zycki *et al.* 2000). Consistent with this picture, the analysis of the *XMM-Newton* and *Chandra* spectra of the nuclear region of NGC 4945 demonstrates that in the 0.5-10 keV range, there is only indirect evidence for the presence of the AGN (since the direct continuum is strongly cut-off below ~ 10 keV).

A clear signature of the underlying AGN in NGC 4945 is the Compton reflection continuum that is

attributed to reprocessing of the underlying continuum off the distant, inside wall of the molecular torus. In this scenario the ratio of the reflected flux to the direct continuum flux, as embodied by the Compton reflection parameter, R , can be used to place a lower limit on the inclination angle of the torus, provided the geometrical configuration of the absorbing torus is known. In reality the true geometry is very uncertain, although the half-opening angle of tori are typically in the range 20° - 50° (e.g. Wilson & Tsvetanov 1994). If the geometry envisaged by Ghisellini, Haardt & Matt (1994) is assumed, then the estimate of $R=0.016$ (based on the ‘average’ continuum given in Guainazzi *et al.* 2000) implies a near edge-on view of the torus. Alternatively a near edge-on but geometrically thin (half-angle $<10^\circ$) distribution of absorbing material located on parsec scales, as inferred by Zycki *et al.* (2000) on the basis of the hard X-ray variability seen in NGC 4945, is also consistent with a very low value for R .

The neutral iron $K\alpha$ line is narrow and the nuclear component has an equivalent width of 1.6 ± 0.1 keV with respect to the observed Compton reflection continuum (cf. ~ 0.5 keV for NGC 7582 and Mrk 3; ~ 1 keV NGC 4151). This is completely consistent with the line and the reflected continuum originating at the same location, namely the visible part of the torus wall (Matt, Brandt & Fabian 1996). There is also a 30% contribution to the neutral iron $K\alpha$ emission from the extended nuclear starburst region, implying that cool material in the environment of the starburst is also exposed to the AGN continuum flux.

Although the hard continuum emanating from the Seyfert 2 nucleus of NGC 4945 is known to be variable on timescales as short as $\sim 10^4$ s (Guainazzi *et al.* 2000), no significant variability is detected in either the *Chandra* or *XMM-Newton* observations, nor is it evident from the joint spectral fits (the time interval between the two sets of observations is 12 months). This tallies with the location of the continuum reprocessing, namely the torus wall, lying at a distance in excess of a light year from the nuclear continuum source. (The apparent discrepancy between the *Chandra*-only and the joint-fit estimates of R is due to the initial modelling of the *Chandra* AGN spectrum incorrectly accounting for the level of starburst contamination present in the *Chandra* AGN spectrum).

5.6.2 The nuclear starburst

The spectral modelling discussed above characterizes the nuclear starburst in terms of two thermal components with temperatures of ~ 0.9 and ~ 6.0 keV. Very similar temperatures were observed for the starburst in the nearby galaxy NGC 253 by Pietsch *et al.* (2001), suggesting that the presence of the AGN in NGC 4945 has little impact on the properties of the surrounding nuclear starburst (there is no evidence for an AGN in NGC 253). Gross spectral features, associated with the cooler of the two starburst components, include the emission lines of Mg X/XI (1.34 keV), Si XII/XIII (1.83 keV) and S XIV/XV (2.45 keV). At higher energies, strong $K\alpha$ line emission from helium-like iron is attributable to the hottest of the starburst components. The high temperature plasma and the associated line emission is characteristic of X-ray emission from a population of type Ib and type IIa SNR’s (Behar *et al.* 2001). No corresponding iron edge is detected in either of the *Chandra* or *XMM-Newton* observations. The unabsorbed luminosity

of the starburst region measured from *XMM-Newton* (0.5-10 keV) is $\sim 8 \times 10^{39}$ erg s⁻¹. Analysis of the separate starburst and X-ray plume spectra shows that the nuclear starburst emission declines rapidly below ~ 1.5 keV, probably as a result of absorbing material in the plane of the galaxy. This absorption may originate in material forming a low scale height disk and/or in material associated with the optical dust lanes of the galaxy.

5.6.3 The X-ray plume

Recent *Chandra* (Strickland *et al.* 2000) and *XMM-Newton* (Pietsch *et al.* 2001) observations have established that the outflow driven by the nuclear starburst in NGC 253 has a limb-brightened conical X-ray morphology. NGC 4945 provides a second example of such a structure. In both galaxies the limb-brightened X-ray structure correlates well with the observed the H α emission. A similar X-ray temperature is derived in each case. (In NGC 253 a single temperature thermal plasma with $kT \sim 0.6$ keV fits the *Chandra* spectrum reasonably well, although the situation is more complicated in the better quality *XMM-Newton* data.) However, there are significant differences between the plumes observed in NGC 4945 and NGC 253. For example, the NGC 4945 X-ray plume displays a somewhat wider opening angle ($\theta \sim 40^\circ$), and the limb brightening is most evident in the 1-2 keV, band whereas in NGC 253 both the *Chandra* and *XMM-Newton* data show that the limb brightened structure is apparent down to 0.5 keV. A similar physical model to that postulated by Pietsch *et al.* (2001) can be inferred for NGC 4945. The limb-brightened structure can be attributed to highly excited gas with a low volume-filling factor, which is produced by an interaction between the starburst-driven wind and the dense ISM surrounding the outflow. In the case of NGC 4945, the comparative uniformity of the emission below 1 keV may be a direct observation of a mass-loaded superwind emanating from the nuclear starburst (as described by Suchkov *et al.* 1996). The question of why the limb-brightened component is hotter in NGC 4945 than in NGC 253 is an interesting point for future detailed studies of this system. An intrinsic luminosity of $\sim 1.1 \times 10^{38}$ erg s⁻¹ (0.5-2 keV) is derived for the superwind component from the *XMM-Newton* data.

5.7 Conclusions

This chapter presents a detailed imaging and spectroscopic analysis of the nuclear region of NGC 4945 using data from both *Chandra* and *XMM-Newton*. The main results of this analysis are:

- The nuclear regions display a complex X-ray morphology, including a predominantly hard source at the nuclear position (which is partially resolved in the *Chandra* data) and a soft X-ray “plume” extending to the northwest of the nucleus.
- The 0.5-10 keV emission from the nuclear source is dominated by a combination of reprocessed

direct AGN continuum (in the form of neutral Compton reflection and iron $K\alpha$ line emission) and thermal emission from a nuclear starburst. The underlying AGN continuum is not observed directly in either the *Chandra* or *XMM-Newton* data, due to heavy ($\sim 4 \times 10^{24} \text{ cm}^{-2}$) absorption in the line-of-sight to the continuum source, that cuts off the continuum below ~ 10 keV.

- The neutral iron $K\alpha$ line is well fit with a narrow Gaussian profile (with an equivalent width of 1.6 ± 0.1 keV), consistent with the line and the reflected continuum originating from the visible part of the torus wall. Furthermore, the best-fit value of the relative reflection parameter, $R=0.016$, implies a near edge-on geometry for the torus.
- Neutral iron $K\alpha$ emission from the extended nuclear starburst region, identified with *Chandra*, implies that cool material in the environment of the starburst is directly exposed to the AGN continuum flux. The thermal emission from the nuclear starburst is fit with a two temperature model, with $kT \sim 0.9$ and ~ 6.9 keV. The spectrum shows clear features associated with the two starburst components, including emission lines of Mg X/XI, Si XII/XIII and S XIV/XV from the cooler component and strong $K\alpha$ line emission from helium-like iron originating in the hotter component.
- A *Chandra* image reveals the X-ray plume to have a limb-brightened morphology in the 1-2 keV band. The plume is associated with the softest thermal emission component observed by *XMM-Newton* and is well modelled by a single temperature thermal model, with $kT \sim 0.6$ keV. When combined, these properties suggest a physical interpretation of the plume as a mass-loaded superwind emanating from the nuclear starburst.

Finally, I would like to emphasize that combining the *Chandra* and *XMM-Newton* datasets has helped to mitigate the limitations of the individual observations and allowed a much more detailed imaging and spectral study than would have been possible with each dataset alone. This work clearly demonstrates the potential of joint *Chandra* and *XMM-Newton* analysis in characterising spatially and spectrally complex X-ray sources, such as those associated with the extended nuclear regions of nearby galaxies.

Chapter 6

The soft X-ray spectrum of NGC 4151

6.1 Overview

This chapter considers the nature and origin of the soft X-ray emission from NGC 4151. The *XMM-Newton* EPIC data recorded during the recent observations of NGC 4151 reveal a soft X-ray (0.5-2 keV) spectrum with prominent features at ~ 0.56 , ~ 0.88 , ~ 1.20 , ~ 1.32 , ~ 1.75 , ~ 2.17 keV. Analysis of the complementary *XMM-Newton* RGS spectra demonstrates that the soft X-ray emission is extremely rich in X-ray emission lines and radiative recombination continua (RRC), with no clear evidence for any underlying continuum emission. Similar photoionized emission lines and RRC are also seen in both Mrk 3 (unsurprisingly given the similarity of the soft X-ray emission in the EPIC spectra) and NGC 1068, strongly suggesting that the soft X-ray ‘excesses’ seen in many Seyfert 2 galaxies are composed of emission lines. The clear association of the soft X-ray extended NLR with the optical ionization cones in NGC 4151 (Ogle *et al.* 2000) prompted the modelling of the RGS spectra in terms of photoionized and photoexcited gas, in a similar fashion to the recent analysis of X-ray grating spectra of NGC 1068 (Kinkhabwala *et al.* 2002). The work presented in this chapter is not a complete analysis of the *XMM-Newton* RGS spectrum of NGC 4151 (which in itself would warrant an entire thesis), but does at least represent a passable preliminary investigation.

The chapter is organised as follows. Section 6.2 summarizes the results of earlier studies of the soft X-ray spectrum of NGC 4151. Section 6.3 details the *XMM-Newton* observations of NGC 4151. Section 6.4 presents the *XMM-Newton* RGS spectra and discusses the spectral modelling in terms of emission from an ionization cone. Section 6.5 compares the NGC 4151 spectra with the soft X-ray spectra of NGC 1068 and Mrk 3 and Section 6.6 compares the RGS spectra for NGC 4151 with the *XMM-Newton* EPIC spectra.

6.2 The soft X-ray spectrum of NGC 4151

6.2.1 NGC 4151

Prior to the advent of *XMM-Newton* and *Chandra*, the origin of the soft X-ray emission from heavily obscured AGN remained very uncertain. Observations of NGC 4151 with *EXOSAT* and *ROSAT* found marginally extended soft X-ray emission that did not exhibit similar variability to the hard X-ray emission (Perola *et al.* 1986 Morse *et al.* 1995). The implication was that the soft X-ray flux is not the result of either leakage of the hard X-ray continuum through a patchy absorber (Holt *et al.* 1980), or a manifestation of the high energy tail of the UV continuum, but a separate spectral component. The X-ray spectra observed by *ROSAT*, *ASCA* and *BeppoSAX* were modelled as a combination of electron scattering of the hard X-ray continuum plus an “ultra-soft” component represented by either a hot thermal plasma or a scattered blackbody (*e.g.* Warwick *et al.* 1996; Weaver *et al.* 1994b). Unfortunately these analyses (particularly those including *BeppoSAX* LECS and *ASCA* GIS data) were complicated by the presence of a soft-spectrum BL Lac (MS 1207.9+3945) located $\sim 5'$ to the north of NGC 4151. Despite the relatively poor quality of the spectra, the *ASCA* spectrum did tentatively reveal several unresolved soft X-ray features, suggesting that the soft X-ray emission was somewhat more complex than previous observations had suggested. The most prominent feature found with *ASCA* was at ~ 0.88 keV and was tentatively associated with O VIII Ly α RRC (Weaver *et al.* 1994b; Griffiths 1999).

The detailed nature of the soft X-ray emission in NGC 4151 was only recently revealed by a *Chandra* HETG observation (Ogle *et al.* 2000). This observation demonstrated that the soft X-ray spectrum was composed almost entirely of emission lines and RRC, with little or no detected continuum emission of any form (and hence no absorption features). Utilizing the excellent spatial resolution of *Chandra*, Ogle *et al.* (2000) resolved $\sim 70\%$ of the soft X-ray emission as extended emission originating up to $11.5''$ from the AGN (Figure 1.8). An excellent correspondence was observed between the soft X-ray emission and the bi-conical [O III] ($\lambda 5007$) emission, previously imaged with the Hubble Space Telescope (HST) (Evans *et al.* 1993). The *Chandra* observation was even capable of resolving the spatial profiles of several of the brightest emission lines (including the iron K α emission line, as previously discussed in Section 3.8) showing that the individual line emission was genuinely extended along the direction of the optical ionization cones. However, it should once again be cautioned (see Section 3.8.2) that the interpretation of the spatial extent of the individual lines may not remain valid if it turns out that Ogle *et al.* (2000) have not determined the spatial profiles of the lines correctly (T. Yaqoob. private communication).

The *Chandra* observation dramatically confirmed that the X-ray spectrum is strongly cut-off below 2 keV and that the soft excess is not predominantly produced by electron scattering of the hard X-ray continuum. Rather, the soft X-ray emission appears to arise in ionization cones at distances of up to ~ 200 pc from the active nucleus (Ogle *et al.* 2000). The *Chandra* analysis finds evidence for both

photoionized and collisionally ionized (thermal) gas in the ENLR, however many of the details of the ionized medium remained elusive, due to the large number (33 in total) and low significance of the features detected.

6.3 The *XMM-Newton* RGS observations of NGC 4151

NGC 4151 was observed with *XMM-Newton* five times during December 21st-23rd, 2000. The RGS instruments were active for all five observations and the data were processed with the standard RGS pipeline processing chains incorporated in the *XMM-Newton* SAS v5.3. Dispersed source spectra and background spectra were extracted with the automated RGS extraction tasks in the SAS. The SAS filters the RGS events in dispersion-channel vs CCD-pulse-height space to separate the data from the separate spectral orders (Section 2.2.2). Investigation of the individual spectra indicate that the 2nd order RGS spectra of NGC 4151 contain a negligible amount of information (with a count rate of $\leq 10\%$ of that in the 1st order spectra) and as a result only the 1st order spectra are presented here. The resulting spectra have a total effective exposure time of ~ 126 ks in each RGS instrument. An investigation of the EPIC spectra confirms that the soft X-ray spectrum of NGC 4151 remained constant for the duration of the observation (as expected from Figure 3.4). The spectra from the five observations were co-added to produce a single high signal-to-noise source spectrum and a single background spectrum for each RGS instrument. The spectra were binned to a minimum of 20 counts per spectral channel, in order to apply χ^2 minimisation techniques (although I note these techniques are not particularly well-suited to fitting the sharp features observed in the soft X-ray spectra of NGC 4151, NGC 1068 or Mrk 3). Investigation of the spatial extent of the X-ray emission observed by *XMM-Newton* reveals that the soft X-ray emission is not significantly extended on scales greater than the mirror PSF, consistent with the details of the previously reported *Chandra* observation of NGC 4151 (Ogle *et al.* 2000).

6.4 Modelling the RGS spectrum of NGC 4151

Figure 6.1 shows the combined *XMM-Newton* RGS spectra of NGC 4151. The spectrum is completely dominated by line emission and radiative recombination continua. Line emission is clearly detected from hydrogen-like and helium-like ionization states of neon, oxygen, nitrogen and carbon and in many cases the line emission associated with these ions is not limited to the Ly α (2p-1s) transition but includes higher order resonance transitions (np-1s) labelled $X^H\beta-\epsilon$ and $X^{He}\beta-\epsilon$ for the different hydrogen-like and helium-like species (X) respectively. Much of the unidentified line emission below ~ 16 angströms can be associated with a multitude of unresolved iron L-shell emission lines, along with some contribution from hydrogen-like and helium-like silicon and magnesium. The spectra show no significant continuum emission and no fluorescent line emission (there may be a marginal detection of silicon K α

fluorescence at $\sim 7.1\text{\AA}$, however without a good knowledge of the iron L-shell emission in this region it is not possible to measure the line cleanly).

6.4.1 The emission lines

The spectrum is remarkably similar to the soft X-ray spectrum of the archetypal bright Seyfert 2, NGC 1068, reported by Kinkhabwala *et al.* (2002) (Figure 6.2). Both sources show strong line triplets from helium-like nitrogen and oxygen, with a similar pattern of resonance, intercombination and forbidden line strengths. Following the analysis of the *XMM-Newton* RGS observation of NGC 1068 (Kinkhabwala *et al.* 2002), line fluxes, centroid energies and line widths were determined for the bright, unambiguously identified, emission lines observed in Figure 6.1. The profiles of the observed emission lines are reasonably well represented by a Gaussian line profile and although this is unlikely to be the correct line profile (given the complexity of the RGS instrument), it is a good enough approximation to allow the determination of accurate line centroid energies, fluxes and, in some cases, line widths. The results of fitting a Gaussian line profile to the brightest emission lines are given in Table 6.1. The measured fluxes take account of the Galactic column density ($2.1 \times 10^{20} \text{ cm}^{-2}$; Warwick, Done & Smith 1995) using the **tbabs** model in XSPEC, and the line shifts are measured with respect to the source redshift of $z=0.00332$. The systematic uncertainty on measuring the centroid line energies of the lines is estimated to be $\sim 8 \times 10^{-3} \text{\AA}$ (which corresponds to about 150 km s^{-1} ; den Herder, Priv. Comm. 2002). The quoted errors are 90% confidence levels as defined by a $\Delta\chi^2=2.71$ criterion (*i.e.* assuming one interesting parameter) and include the systematic uncertainty added in quadrature. Most of the measured line centroid energies are consistent with a mild blueshift, of between $\sim 100\text{-}1000 \text{ km s}^{-1}$, with respect to the systemic velocity of the lines. This implies a line-of-sight outflow velocity for the ionized material of $\lesssim 1000 \text{ km s}^{-1}$, consistent with the line shifts of the absorption lines observed in the UV spectrum of NGC 4151 ($\sim 600 \text{ km s}^{-1}$; Kriss *et al.* 1995). Many of the observed line widths are largely unconstrained, with the spectral fitting only yielding upper limits (these are not quoted in Table 6.1); however the seven line widths that are constrained by the spectral fitting appear to show a bimodal distribution with the shorter wavelength lines having an average line width of $\sigma \sim 2.0 \text{ eV}$ ($\sim 1000 \text{ km s}^{-1}$ FWHM) and the longer wavelength lines having an average line width of $\sim 0.6 \text{ eV}$ ($\sim 200 \text{ km s}^{-1}$ FWHM). The observed line widths imply that the intrinsic velocity dispersion of the outflowing material is $\lesssim 1000 \text{ km s}^{-1}$ which is somewhat lower than the line widths of the absorption lines observed in the UV ($1000\text{-}2500 \text{ km s}^{-1}$; Kriss *et al.* 1995). The bimodal distribution of the line widths as a function of the wavelength of the line is suggestive of a scenario in which individual clouds of emitting material close to the source of the ionizing continuum are moving more rapidly than clouds further from the continuum source. Note that NGC 4151 is not extended on scales larger than the mirror PSF, hence source extent does not contribute to the measured line widths in the RGS spectrum.

Table 6.1: Line properties of individual emission lines observed in the RGS spectra of NGC 4151

Line ID	λ_{Obs} Å	λ_{Rest}^a Å	Line Shift km s ⁻¹	σ_{Obs} eV	Flux ×10 ⁻⁴ Photons s ⁻¹ cm ⁻²
Ne _α ^H	12.13 ^{+0.01} _{-0.01}	12.134	-124 ⁺²⁴⁸ ₋₂₄₇	2.1 ^{+0.8} _{-0.7}	0.417 ^{+0.05} _{-0.05}
Ne _r ^{He}	13.43 ^{+0.02} _{-0.01}	13.447	-431 ⁺⁴⁸⁶ ₋₂₆₄	1.9 ^{+1.5} _{-0.9}	0.468 ^{+0.05} _{-0.05}
Ne _i ^{He}	13.53 ^{+0.01} _{-0.02}	13.550	-467 ⁺²³⁶ ₋₃₃₇	1.6 ^{+1.3} _{-1.0}	0.463 ^{+0.15} _{-0.07}
Ne _f ^{He}	13.68 ^{+0.01} _{-0.02}	13.697	-311 ⁺²¹⁵ ₋₁₇₇		1.03 ^{+0.1} _{-0.09}
O _β ^H	16.00 ^{+0.02} _{-0.02}	16.006	-150 ⁺²²⁶ ₋₂₂₆	2.5 ^{+0.5} _{-0.5}	0.372 ^{+0.04} _{-0.04}
O _α ^H	18.96 ^{+0.01} _{-0.01}	18.969	-210 ⁺¹²⁸ ₋₁₃₄		1.55 ^{+0.1} _{-0.1}
O _r ^{He}	21.59 ^{+0.01} _{-0.01}	21.603	-231 ⁺¹⁴² ₋₁₄₂		1.19 ^{+0.09} _{-0.09}
O _i ^{He}	21.79 ^{+0.01} _{-0.01}	21.798	-227 ⁺¹¹⁵ ₋₁₂₆		0.754 ^{+0.07} _{-0.07}
O _f ^{He}	22.08 ^{+0.01} _{-0.01}	21.095	-326 ⁺¹¹² ₋₁₁₂	0.55 ^{+0.07} _{-0.07}	3.89 ^{+0.17} _{-0.19}
N _β ^H	20.89 ^{+0.01} _{-0.01}	20.910	-234 ⁺¹⁵⁶ ₋₁₅₀	0.6 ^{+0.4} _{-0.3}	0.22 ^{+0.04} _{-0.04}
N _α ^H	24.77 ^{+0.01} _{-0.01}	24.781	-194 ⁺¹⁰⁹ ₋₁₁₄		0.81 ^{+0.09} _{-0.08}
N _r ^{He}	28.75 ^{+0.01} _{-0.01}	28.792	-345 ⁺¹¹² ₋₁₁₂		0.45 ^{+0.07} _{-0.06}
N _i ^{He}	29.09 ^{+0.02} _{-0.02}	29.075	27 ⁺²⁴⁷ ₋₁₆₁		0.36 ^{+0.06} _{-0.06}
N _f ^{He}	29.51 ^{+0.01} _{-0.01}	29.531	-290 ⁺⁹⁹ ₋₁₀₅		1.15 ^{+0.12} _{-0.12}
C _β ^H	28.43 ^{+0.01} _{-0.01}	28.466	-390 ⁺¹²⁷ ₋₁₂₇	0.7 ^{+0.2} _{-0.2}	0.37 ^{+0.05} _{-0.05}
C _α ^H	33.69 ^{+0.01} _{-0.01}	33.736	-436 ⁺⁸⁹ ₋₈₉		1.79 ^{+0.16} _{-0.16}

^a (Vainshtein & Safronova 1978)

6.4.2 Temperature diagnostics with radiative recombination continua

Radiative recombination continua (RRC) are the result of a free electron recombining directly into the ground state ($1s^2 1S_0$) of an ion. The free electrons can have any energy above the recombination threshold and hence the feature produced is neither symmetrical or narrow. The energy of the electrons prior to the recombination process is dependent upon the electron temperature of the emitting plasma and hence the width of the RRC features provides a direct measurement of the recombining electron temperature, T_e (Liedahl & Paerels 1996; Liedahl 1999). RRC originating in hot plasmas are broad features however, RRC from cool plasmas are narrow, prominent, features. The velocity dispersion of the emitting material will affect the RRC in exactly the same manner as it affects the emission lines discussed previously, however this effect is negligible here due to the low velocities of the ions involved compared to that of the electrons. Radiative recombination continua from hydrogen-like and helium-like ionization states of Ne, O, N and C are clearly identifiable in Figure 6.1. Electron temperatures were determined for the bright, unambiguously identified, RRC and are given in Table 6.2 and imply electron temperatures of $\sim 2-4 \times 10^4$ K.

Table 6.2: Electron temperatures (in eV) from RRC

RRC	T_e
C V	$2.5^{+1.5}_{-0.5}$
C VI	$4.0^{+1.0}_{-1.0}$
N VI	$3.0^{+3.0}_{-1.0}$
N VII	$4.0^{+2.0}_{-1.5}$
O VII	$4.0^{+0.5}_{-0.5}$
O VIII	$6.0^{+1.0}_{-2.0}$

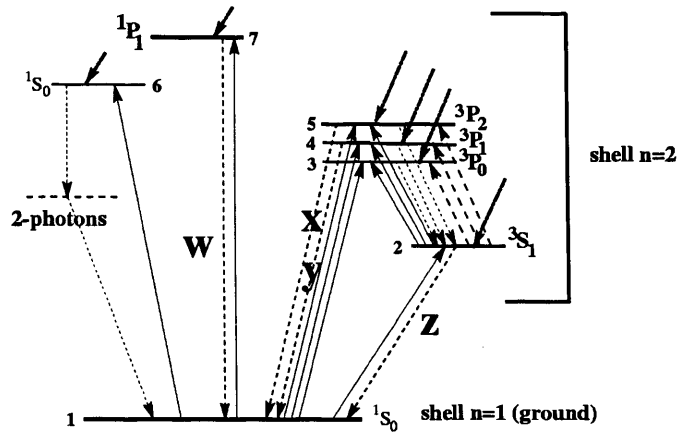


Figure 6.3: Simplified energy level diagram for the triplet emission from helium-like ions. The resonance, intercombination and forbidden line transitions are denoted by w, x+y and z respectively. The solid upward arrows represent excitation transitions (photoexcitation and collisional excitation), the dashed arrows represent radiative transitions and the dot-dashed arrows represent the recombination and cascade processes. (Porquet *et al.* 2002)

The association of high-ionization emission lines (*e.g.* O VIII, Ne X etc; identified in the previous section) with such a low temperature plasma is strongly indicative of a plasma whose ionization state is governed by photoionization as opposed to collisional ionization.

6.4.3 Plasma diagnostics with helium-like triplets

The three most prominent X-ray emission lines from helium-like ions correspond to transitions from the $n=2$ shell to the $n=1$ shell and are the resonance ($1s2p\ ^1P_1 \rightarrow 1s^2\ ^1S_0$), intercombination ($1s2p\ ^3P_{2,1} \rightarrow 1s^2\ ^1S_0$) and forbidden ($1s2s\ ^3S_1 \rightarrow 1s^2\ ^1S_0$) line transitions (Pradhan, Norcross & Hummer 1981). A simple energy level diagram for these transitions is shown in Figure 6.3. Ratios of the measured line fluxes for the recombination, intercombination and forbidden emission lines from helium-like ions provide a diagnostic of the electron density and temperature in hot plasmas. Gabriel & Jordan (1969) were the first to

Table 6.3: Helium-like triplet plasma diagnostic ratios

Triplet ID	R	G
Ne ^{He}	2.3 ^{+0.7} _{-0.7}	3.2 ^{+1.2} _{-0.9}
O ^{He}	3.4 ^{+0.4} _{-0.3}	3.9 ^{+0.5} _{-0.5}
N ^{He}	3.0 ^{+1.1} _{-0.8}	3.4 ^{+1.0} _{-0.8}

recognise the importance of the helium-like triplet lines and used line strength ratios to analyse the solar corona spectra in detail. The ratio of the intensity of the forbidden line to the intensity of the intercombination line [R, where $R=f/i$ or, with reference to Figure 6.3, $R=z/(x+y)$] is sensitive to the electron density of the plasma and the ratio of the sum of the intensities of the forbidden and intercombination lines to the intensity of the resonance line [G, where $G=(i+f)/r$ or, with reference to Figure 6.3, $G=(z+x+y)/w$] is sensitive to the electron temperature of the plasma. For a detailed discussion of the manner in which the ratios depend on the electron density and the plasma temperature see Pradhan, Norcross & Hummer (1981); Porquet & Dubau (2000); Dubau & Porquet (2002); Porquet *et al.* (2002) and references therein.

Only recently, with the advent of high quality, high resolution, X-ray grating spectra from observations by *Chandra* and *XMM-Newton*, has the use of these plasma diagnostic ratios become possible for AGN. The R and G ratios for the Ne, O and N triplets observed in the RGS spectrum of NGC 4151 are given in Table 6.3. The G-values imply an electron temperature of $\lesssim 10^5$ K, consistent with the electron temperatures implied from the properties of the observed RRC and consistent with photoionization being the dominant ionization mechanism in the plasma (Porquet & Dubau 2000). The R-values imply electron densities of $\sim 10^8$ - 10^9 cm⁻³ in nitrogen and oxygen and $\sim 10^{10}$ - 10^{11} cm⁻³ from neon (Porquet & Dubau 2000). In particular the ratios calculated from the oxygen triplet (which is both the strongest and the least confused of the helium-like triplets) strongly imply a photoionized plasma. However, extracting detailed values of density and temperature for the emitting material is complicated by the possibility that a strong radiation field (*i.e.* photoexcitation) can mimic the effect that a relatively high density has on the line strengths and thus cause the electron density, and to a lesser extent, the electron temperature to be overestimated (Porquet *et al.* 2002). I note that the expected contribution of blended dielectronic satellite lines to these ratios has not been taken into account in the values quoted here. For the N and O triplets this contribution is negligible; however the Ne triplet is significantly affected. For a high temperature, collisionally dominated, plasma the additional contribution can result in an error of $\sim 1\%$ and $\sim 9\%$ for the R and G ratios respectively, however for a photoionized plasma, where the temperatures are several orders of magnitude lower, this effect can be considerably greater (Porquet *et al.* 2002).

6.4.4 The ionization cone model

Given the similarity between the RGS spectra of NGC 1068 and NGC 4151, I utilize the ‘ionization cone’ model developed by Kinkhabwala *et al.* (2002) to describe the RGS spectrum of NGC 1068, to fit the RGS spectrum of NGC 4151. This model, which was incorporated into XSPEC for ease of spectral fitting, reproduces the hydrogen-like and helium-like line emission, and the associated RRC, from an irradiated cone of optically thin plasma (*c.f.* ionization cones observed in OIII by HST) shown schematically in Figure 6.4. The model includes the effects of both photoionization and, crucially, photoexcitation. Photoexcitation is the process by which the absorption of a photon with insufficient energy to ionize the atom, results in the transition of an inner-shell electron to a higher energy level within the atom. The excited electron will rapidly undergo one or more radiative transitions, decaying back to its original energy state. Photoexcitation is expected to enhance the intensity of the higher order resonance transition lines relative to the 1st order resonance lines and was observed to play a significant role in the spectrum of NGC 1068 where the Ly β , Ly γ and Ly δ lines were significantly stronger than predicted by models based on pure photoionization or collisional ionization.

The plasma is irradiated by an unabsorbed intrinsic power-law continuum, the slope of which in the case of NGC 4151 is fixed at $\Gamma=1.65$, based on the analysis of the EPIC spectra (Section 3.7). The luminosity of the central source, L_X , and the covering fraction of the cone, f , are fixed at $L_X=6\times 10^{43}$ erg s⁻¹ and $f=0.1$, respectively. The modelling includes both Galactic column density (2.1×10^{20} cm⁻²; Warwick, Done & Smith 1995 using the **wabs** model in XSPEC and a source redshift of $z=0.00332$. The electron temperatures for each atomic species were fixed at the temperatures found from the analysis of the RRC (Table 6.2), where possible, and the remaining RRC temperatures were fixed at the temperatures identified by Kinkhabwala *et al.* (2002) (based on the similarity between the observed bright RRC in NGC 4151 and the corresponding RRC in NGC 1068). The remaining free parameters of the model are the transverse velocity distribution of the lines, σ_v^{obs} , the radial velocity distribution of the lines, σ_v^{rad} , and the radial column density of each individual atomic species, N_{ion}^{rad} .

6.4.5 Fitting the ionization cone model to the RGS spectra

The ionization cone model was fitted to the RGS spectra in XSPEC for simplicity. As mentioned previously, the spectra were binned in order to apply χ^2 minimisation techniques. However, I note that χ^2 minimisation techniques are not particularly well-suited to fitting the sharp spectral features observed in this and similar X-ray grating spectra and that the complexity of this specific model makes the accurate determination of individual parameter errors problematic. Despite this caveat, the model provides a “good fit” to all the hydrogen-like and helium-like line emission and RRC observed in the RGS spectra; although, due to the nature of the spectrum and the model, the term “good fit” here refers to a set of parameters that can reproduce the features of the spectrum in detail (*i.e.* it is not a statistical measure of

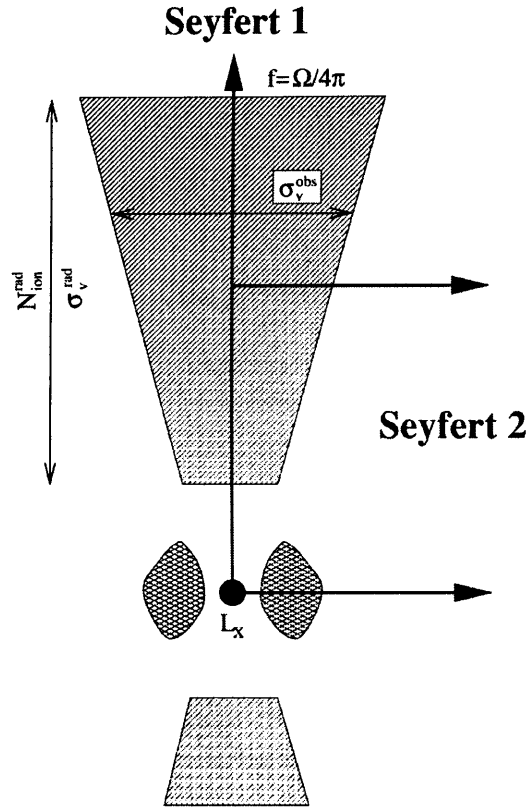


Figure 6.4: Schematic cartoon of the ‘ionization cone’ model (not to scale). The model is similar to the unified AGN schematic shown in Figure 1.10. The central nuclear components (black hole and accretion disk), denoted by the black spot, are surrounded by a dense absorbing torus of neutral dust and gas. The optically thin material perpendicular to the plane of the absorbing torus sees the direct continuum from the X-ray source and becomes strongly ionized forming ionization cones. The line emission from these cones is observable from Seyfert 2 galaxies due to the suppression of the direct continuum, whereas the ionization cones in Seyfert 1 galaxies are only seen through their absorption of the direct continuum.

the goodness of fit of the model). Figure 6.5 shows the best-fit of the ionization cone model to all the hydrogen-like and helium-like emission lines and RRC in the RGS spectrum of NGC 4151. The best-fit radial ionic column densities and the associated RRC electron temperatures are given in Table 6.4. σ_v^{obs} has a best-fit value of $\sigma_v^{obs} \sim 400 \text{ km s}^{-1}$ and σ_v^{rad} has a best-fit value of $\sim 330 \text{ km s}^{-1}$, both of which are in good agreement with the average line widths and line shifts measured from the individual line centroid energies. Kinkhabwala *et al.* (2002) quote an estimate for the uncertainties on the individual model parameters of approximately a few tens of percents for the ionic column densities and approximately a factor of 2 for the transverse and radial velocities. Using a fraction ionic abundance of 0.5 for O VIII, the column density of O VII quoted in Table 6.4 yields an equivalent hydrogen column density of $N_H \gtrsim 2 \times 10^{21} \text{ cm}^{-2}$.

Table 6.4: Best-fit parameters for the ‘ionization cone’ model fit to the RGS spectra of NGC 4151

ion	N_{ion}^{rad} (cm^{-2})	kT_e (eV)
C V	2.0×10^{17}	2.5
C VI	2.9×10^{17}	4.0
N VI	1.3×10^{17}	3.0
N VII	5.2×10^{16}	4.0
O VII	6.7×10^{17}	4.0
O VIII	5.8×10^{17}	6.0
Ne IX	3.8×10^{17}	4.0 ^a
Ne X	2.6×10^{17}	4.0 ^a
Mg XI	7.0×10^{16}	4.0 ^a
Mg XII	2.7×10^{17}	4.0 ^a
Si XIII	4.7×10^{17}	4.0 ^a
Si XIV	7.8×10^{17}	4.0 ^a

^a Unconstrained parameter. Value fixed at the value used in Kinkhabwala *et al.* (2002)

6.5 A comparison with NGC 1068 and Mrk 3

The archetypal Seyfert 2 galaxies, NGC 1068 and Mrk 3 have both been the targets of recent X-ray grating observations. The soft X-ray emission in both of these sources is extremely similar to the soft X-ray emission from NGC 4151; it is extended on scales of hundreds of parsecs, shows a strong correlation with the optical ionization cones identified in HST [O III] ($\lambda 5007$) images (see chapter 1; Young, Wilson & Shopbell 2001; Sako *et al.* 2000) and the soft X-ray spectra are all dominated by emission lines and RRC.

6.5.1 The comparison with the *XMM-Newton* RGS spectrum of NGC 1068

A recent long (110 ks) observation of NGC 1068 with *XMM-Newton* has resulted in a remarkably high-quality RGS spectrum of the soft X-ray emission from this source. This spectrum demonstrates unambiguously that the soft X-ray emission in NGC 1068 is composed entirely of emission lines and RRC (Figure 6.2) with an origin in a photoionized and photoexcited plasma (Kinkhabwala *et al.* 2002). The soft X-ray spectrum of NGC 4151 is remarkably similar to that of NGC 1068. Both sources show strong hydrogen-like and helium-like line emission and RRC from carbon, nitrogen, oxygen, neon, magnesium and silicon. The resemblance between the spectra is apparent in the details of the spectra as well as on a more general level. For example, both show similar patterns of resonance, intercombination and for-

bidden line strengths for the helium-like triplets of nitrogen and oxygen and both show significant (but unresolved) iron L-shell emission. The properties of the detected emission lines are remarkably alike in the two sources, both in terms of the lines present and the scale of their energy shifts. In both sources the prominent emission lines are blue-shifted by $<1000 \text{ km s}^{-1}$ with average line shifts of 305 km s^{-1} and 375 km s^{-1} for NGC 4151 and NGC 1068, respectively (Kinkhabwala *et al.* 2002). The line widths measured for NGC 1068 do not show the bimodal distribution observed in NGC 4151. However, since only 7 lines have constrained line widths in the NGC 4151 spectrum, compared to 23 lines with constrained widths in the NGC 1068 spectrum, caution should be emphasised in interpreting the validity of the distribution of line widths in NGC 4151. Interestingly the average line width found in the NGC 1068 data ($\sim 1100 \text{ km s}^{-1}$ FWHM) is comparable to the average line width of the group of broader lines in the NGC 4151 spectrum ($\sim 1000 \text{ km s}^{-1}$ FWHM). A comparison of the helium-like triplet plasma diagnostic ratios (R and G; Section 6.4.3) indicate that the ionization cones in NGC 4151 have a somewhat lower electron temperature and a somewhat higher electron density than NGC 1068 (Kinkhabwala *et al.* 2002).

The ionization cone model utilized in the previous section, was developed by Kinkhabwala *et al.* (2002) to model the hydrogen-like and helium-like emission features in the NGC 1068 spectrum. This model resulted in a remarkably good fit to all the observed hydrogen-like and helium-like emission lines, and the RRC in the soft X-ray spectrum of NGC 1068. The best-fit ionic column densities were similar to those observed in absorption for Seyfert 1 galaxies and imply either radially stratified ionization zones or, more likely, a broad distribution of densities at any given radius. An inspection of the radial column densities fit to the RGS spectrum reveals that NGC 4151 appears to have less ionized material in its ionization cones, by a factor of ~ 3.5 on average. The exceptions to this are the short wavelength lines (Si, Mg etc). These lines are poorly constrained and strongly contaminated by significant iron L-shell emission that can lead to an over-estimation of the ionic column densities of these elements. The best-fit ionic electron temperatures, based on the widths of the RRC features, are also extremely similar (although the comparatively large errors on these temperatures prevents any definite conclusions being drawn regarding this similarity). The lower ionic column densities could be the result of lower ionizing flux or less material in the ionization cones, however a more plausible explanation, in line with the smaller R-values from the helium-like line triplets, would be that the material in the ionization cones of NGC 4151 is rather more dense than the material in the ionization cones of NGC 1068. Since the recombination rate is dependent on the density of the material, this results in a smaller ionized fraction for a similar ionizing continuum.

6.5.2 The comparison with the *Chandra* HETG observation of Mrk 3

The recent *Chandra* HETG observation of Mrk 3 was the first published high resolution soft X-ray spectrum of a Seyfert 2 galaxy and, in a similar fashion to NGC 1068, showed unambiguously that the soft X-ray emission in Mrk 3 is composed almost entirely of emission lines and RRC, with little or no continuum emission. The soft X-ray spectrum is, again, remarkably analogous to the soft X-ray spectrum

of NGC 4151, though with somewhat less statistical significance due to the rapidly decreasing effective area of the HETG instrument at wavelengths above $\sim 9\text{\AA}$. In both sources there is strong evidence to suggest that the observed emission lines are produced in a photoionized and photoexcited plasma (Sako *et al.* 2000). The importance of photoexcitation in the spectrum of Mrk 3 is highlighted by the observed weak iron L-shell emission, rather than by the enhanced higher order resonance transitions, rejecting explanations from a recombination dominated or a collisionally dominated plasma. Despite this impressive spectrum, the *Chandra* observation of Mrk 3 only partially resolves two of the helium-like line triplets detected in the RGS spectrum of NGC 4151 (oxygen and neon), due to the limited statistical significance of the features, and as a result many of the properties of the plasma are not well constrained. In particular, the resonance and intercombination lines of these triplets cannot be separated, and as a result Sako *et al.* (2000) quote a different diagnostic line ratio [*i.e.* $(r+i)/f$] to the line ratios used here.

At wavelengths shorter than $\sim 9\text{\AA}$ the *Chandra* spectrum shows evidence for a reflection dominated continuum (similar to that fit in Section 4.3) along with clear detections of emission lines that are either extremely difficult or impossible to detect with the RGS (given its limited spectral bandpass), namely Fe XXVI, Fe XXV, Fe $K\alpha$, S XVI, S XV, S $K\alpha$, Si XIV, Si XIII, Si $K\alpha$, Mg XII and Mg XI (Sako *et al.* 2000). This plethora of lines highlights the complementary capabilities of *XMM-Newton* and *Chandra* and strongly supports future observations of bright, heavily obscured AGN with both *Chandra* (using the HETG) and *XMM-Newton*, to obtain the highest possible resolution X-ray spectra over the widest possible energy range. The line ratios calculated from the *Chandra* detections of the helium-like silicon and magnesium line triplets (*i.e.* Si XIII and Mg XI) are all inconsistent with the expected values for a collisionally ionized plasma and are marginally consistent with the predictions from a photoionized plasma, similar to the conclusions from the triplet ratios for both NGC 4151 and NGC 1068.

6.6 A brief comparison with the *XMM-Newton* EPIC spectra

One of the strengths of *XMM-Newton* is that all the science instruments operate simultaneously during each observation, allowing a direct comparison between the high resolution spectra from the RGS instruments and the lower resolution spectra from the EPIC CCD detectors. This comparison is particularly useful in exposing features in each spectrum that the other detectors struggle to detect. For example, broad features present in the 0.3-2.5 keV range are not easily identified in RGS spectra, but will be more clearly observed by the EPIC instruments. Conversely, features that appear to be broad in the EPIC spectrum may be resolved into a set of individual narrow lines by the RGS instruments. Conclusions from the process of comparing the EPIC and RGS spectra are complicated by the need for good calibration and cross-calibration for each instrument involved.

Figure 6.6 shows the full window mode EPIC MOS 1 and 2 spectra fit with a model that combines the best-fit of the hard X-ray model developed in chapter 3 and the best-fit of the ‘ionization cone’ soft X-ray

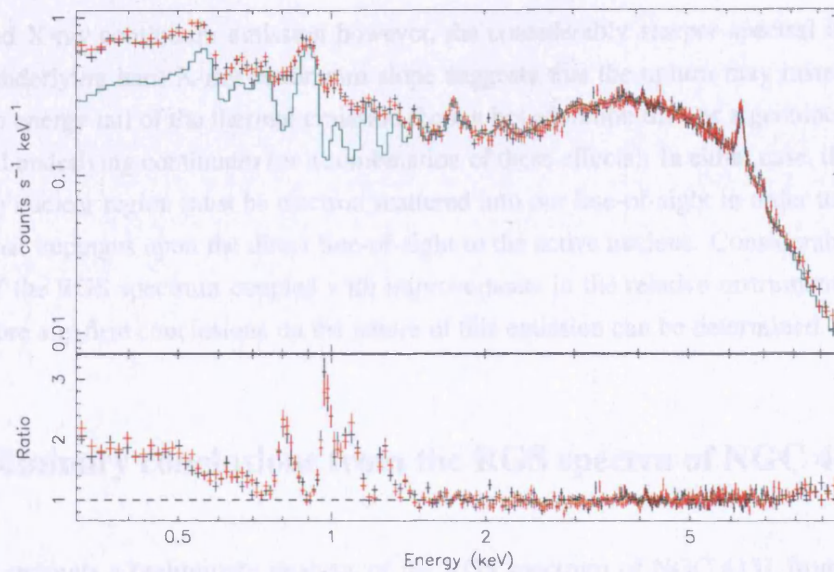


Figure 6.6: *Upper Panel:* The 0.3-10 keV EPIC MOS 1 (Black) and MOS 2 (Red) spectra of NGC 4151 modelled by a combination of the hard X-ray model developed in chapter 3 and the ‘ionization cone’ soft X-ray model developed earlier in this chapter (Green). *Lower Panel:* The ratio of the data to the model prediction.

model developed earlier in this chapter. Initially the ionization cone model parameters were fixed and a constant scaling parameter was included in the model to adjust the normalisation of the this model relative to the hard X-ray model. Knowing that the ionization cone model is not complete, particularly in the regions where iron L-shell emission contributes to the spectrum, the constant scaling parameter was adjusted such that the peaks of the line complexes that are well defined by the ionization cone model (*i.e.* O VII, Ne IX etc), did not exceed the counts observed in the EPIC spectra. The fit of the ionization cone model to the RGS spectrum strongly over-predicts the contribution of magnesium, aluminium and silicon to the spectrum (Section 6.5.1). The column densities of these elements are likely to be better constrained by the EPIC spectra and were allowed to be free parameters in the fitting. In addition to the hard X-ray model and the ionization cone model, a silicon $K\alpha$ line was included in the fitting. The energy of the line was fixed at 1.73 keV and the line width was fixed to be the same width as the iron $K\alpha$ line. The line flux was fixed to be 5% of the flux contained in the iron $K\alpha$ line, in keeping with the measured ratio of the iron $K\alpha$ to silicon $K\alpha$ line fluxes measured in Mrk 3.

The fit to the data in Figure 6.6 clearly highlights regions of the soft X-ray spectrum that are not well reproduced by the ionization cone model. Much of the emission between 0.75-1.4 keV (~ 9 - 16\AA) can be attributed to iron L-shell emission lines that are not currently included in the spectral model of the RGS data. The deficit between the model and the data below 0.8 keV appears to reveal a smooth systematic upturn in the soft X-ray spectrum, similar to the smooth soft excesses found in Seyfert 1 galaxies. Modelling the upturn below ~ 0.8 keV with a simple power-law model yields a flux of $\sim 1.5\%$ of the flux in the underlying hard X-ray continuum and a steep slope ($\Gamma \sim 3.5$). The smooth upturn may be associated

with scattered X-ray continuum emission however, the considerably steeper spectral index in comparison to the underlying hard X-ray continuum slope suggests that the upturn may instead be associated with the high energy tail of the thermal emission from a hot accretion disk or a genuine curvature in the Comptonized underlying continuum (or a combination of these effects). In either case, the emission originating in the nuclear region must be electron scattered into our line-of-sight in order to avoid the heavy absorption that impinges upon the direct line-of-sight to the active nucleus. Considerably more detailed modelling of the RGS spectrum coupled with improvements in the relative instrument calibrations are required before any firm conclusions on the nature of this emission can be determined.

6.7 Preliminary conclusions from the RGS spectra of NGC 4151

This chapter presents a preliminary analysis of the RGS spectrum of NGC 4151 from a total of ~ 125 ks of *XMM-Newton* observations. The EPIC spectra from these observations are presented in chapter 3 of this thesis. The analysis uses the high spectral resolution of the RGS instruments to characterise the nature and origin of the soft X-ray spectrum of NGC 4151. The main results of the preliminary analysis are:

- The soft X-ray spectrum of NGC 4151 (Figure 6.1) is completely dominated by line emission and radiative recombination continua. Line emission, including higher order (β - ϵ) resonance transitions, is clearly detected from hydrogen-like and helium-like ionization states of neon, oxygen, nitrogen and carbon. Much of the unidentified line emission below ~ 16 angströms can be associated with a combination of iron L-shell emission and lines from hydrogen-like and helium-like silicon and magnesium.
- The RGS spectra show no significant continuum emission and no fluorescent line emission associated with neutral material.
- The measured line centroid energies are consistent with a blueshift of between ~ 100 - 1000 km s^{-1} , with respect to the systemic velocity of NGC 4151. The seven observed line widths that are well constrained by the data show a bimodal distribution, with average line widths of ~ 1000 km s^{-1} and ~ 200 km s^{-1} (FWHM). The measured line blueshifts are generally consistent with the outflow velocities of the absorption lines observed in the UV spectrum of NGC 4151 (Kriss *et al.* 1995), implying that the UV and X-ray line features originate in the same material.
- Plasma diagnostics, based on the ratios of the resonance, intercombination and forbidden lines of the observed helium-like triplets, imply an electron temperatures of $\sim 1.5 \times 10^4$ K and electron densities of $\sim 10^8$ cm^{-3} in nitrogen and oxygen and $\sim 10^{10}$ cm^{-3} from neon (Porquet & Dubau 2000). The wide range of the measured electron densities is suggestive of either a ‘clumpy’ extended NLR or a region in which the material has grossly non-solar elemental abundances however, the

presence of a strong radiation field can mimic the effects of a high density medium on the line strengths and could be causing the electron densities (and temperatures) to be overestimated.

- The soft X-ray spectrum of NGC 4151 is remarkably similar to the soft X-ray spectrum of NGC 1068 (Figure 6.2). The correspondence between the two source spectra is evident on the general scale from the strong emission lines and RRC associated with the same ionic species, which dominate the spectra of both sources. The resemblance of the NGC 4151 and NGC 1068 soft X-ray spectra is also apparent in the details of the spectra (*i.e.* the similar helium-like triplet ratios and RRC temperatures).
- The ‘ionization cone’ model, developed by Kinkhabwala *et al.* (2002) to model the RGS spectra of NGC 1068, reproduces all of the hydrogen-like and helium-like emission features observed in the soft X-ray spectrum of NGC 4151 *in detail*. The best-fit radial and transverse velocities of the material in the ionization cones agree well with the blueshift and velocity dispersion measured from the individual line centroid energies, and are similar to the radial and transverse velocities measured from the soft X-ray spectrum of NGC 1068. The individual ionic column densities are somewhat smaller than those measured for NGC 1068, which, in combination with the plasma diagnostic ratios from the helium-like triplets, suggests that the material in the ionization cones of NGC 4151 may be somewhat denser than the material in the ionization cones of NGC 1068.

Chapter 7

Final words

7.1 Overview: Conclusions and issues for the future

This thesis presents an investigation of the X-ray properties of four nearby galaxies, NGC 4151, NGC 7582, Mrk 3 and NGC 4945, all of which harbour a bright, heavily obscured Seyfert nucleus. The work focuses largely on data from the *XMM-Newton* X-ray satellite, concentrating initially on hard X-ray spectra from the EPIC CCD cameras. The spectral analysis examines the role of continuum reprocessing in these sources, concentrating on the impact of heavy absorption, Compton reflection and reprocessing by iron.

The wide range of column densities exhibited across these four objects (10^{23} cm^{-2} to $>10^{24} \text{ cm}^{-2}$) demonstrates the influence of heavy absorption in both Compton-thin, continuum-dominated sources (such as NGC 4151) and Compton-thick, reflection-dominated sources (*e.g.* Mrk 3 and NGC 4945). The extent of the role that Compton reflection plays in the X-ray spectrum of each source is determined in each case by the level of the intrinsic absorption and, as a result, the impact of Compton reflection can be anything from being a subtle modification of the spectrum (as in NGC 4151) to being the dominant component observed in the 2-10 keV band (as in Mrk 3 and NGC 4945). All four objects presented here display neutral (or near-neutral) iron reprocessing features, namely a narrow (or near-narrow) iron $K\alpha$ line and a sharp iron K edge, adding to the growing body of evidence which suggests that iron reprocessing features are ubiquitous constituents of the hard X-ray spectra of AGN. The analysis of NGC 4945 demonstrates the enormous impact that a nuclear starburst can have on the X-ray properties of AGN, making the identification of the underlying AGN emission extremely problematic. Only by combining the capabilities of *Chandra* and *XMM-Newton* was it possible to individually characterize the starburst and AGN components, demonstrating the potential of joint *Chandra* and *XMM-Newton* analysis in studying spatially and spectrally complex X-ray sources.

The preliminary analysis of the *XMM-Newton* RGS spectrum of NGC 4151 completes the X-ray picture of this heavily obscured Seyfert. The soft X-ray spectrum of NGC 4151 is extremely similar to that of the archetypal Seyfert 2 galaxy NGC 1068, it being dominated by emission features with no significant continuum emission, highlighting the complex nature of the soft X-ray emission in heavily obscured AGN as a whole. Similarly to NGC 1068, the soft X-ray emission is observed to originate in photoionized and photoexcited gas located in X-ray/optical ionization cones.

Each of the previous chapters contains a detailed summary of the chapter and conclusions specific to the work presented therein however, Section 7.2 summarizes the most important of the specific conclusions from each chapter. Section 7.3 identifies five important questions currently facing researchers in the AGN field, and discusses how the work presented here relates to these issues and how future instrumentation might be able to provide some insight into the answers to these questions.

7.2 Specific conclusions from this thesis

- **Complex absorption in NGC 4151:** The analysis of long observations from *BeppoSAX* and *ASCA* has provided a strong indication that the complex absorption observed in NGC 4151 is the result of a combination of warm and cold gas distributed along the line-of-sight to the active Seyfert nucleus. This conclusion is confirmed by the relatively simple model's excellent description of a recent ~ 125 ks *XMM-Newton* observation of NGC 4151. The key finding is that the warm absorber corresponds to a relatively low density ($\sim 10^{4-5} \text{ cm}^{-3}$) gas, with a column density of $\sim 2 \times 10^{23} \text{ cm}^{-2}$ and an ionization parameter in the range $\log(\xi) \approx 2.4-2.7$. The warm absorber component is invariably observed in a non-equilibrium ionization state, which may explain why previous studies based on relatively short observations spaced by weeks, months or years have failed to identify the consistent signature of a warm absorber in this source. (chapter 3)
- **The iron $K\alpha$ line profile in NGC 4151:** None of the hard X-ray spectra of NGC 4151 presented in this thesis (including the extremely high statistical quality spectrum from the *XMM-Newton* observation) show any evidence for a relativistically broadened iron $K\alpha$ line, contrary to the earlier conclusions of Yaqoob *et al.* (1995), Wang, Zhou & Wang (1999) and Wang, Wang & Zhou (2001). The upper limit on the flux of a broad iron $K\alpha$ line in the *XMM-Newton* EPIC spectra is $1.0 \times 10^{-5} \text{ photons cm}^{-2} \text{ s}^{-1}$. (chapter 3)
- **Iron $K\alpha$ line variability in NGC 4151:** The iron $K\alpha$ line flux measured during the recent *XMM-Newton* observation of NGC 4151 is significantly lower than that measured by earlier observations, where the line flux was typically $\sim 70\%$ greater. The decrease in the iron $K\alpha$ line flux is in contrast with the behaviour of the Compton reflection component, which is consistent with remaining relatively constant. Associating the reflection component with reprocessing from the inner edge of the torus, this decoupling of the iron $K\alpha$ line and the reflection continuum suggests that at least part of

- the line is formed in optically-thin, cool, clouds located within the inner radius of the torus. In this scenario the decline of the iron $K\alpha$ line flux presumably coincides with the central source entering a fairly prolonged low flux period, sampled only recently by the *XMM-Newton* observations. (chapter 3)
- **Soft X-ray and UV lines in NGC 4151:** The soft X-ray spectrum of NGC 4151 is completely dominated by line emission and radiative recombination continua from hydrogen-like and helium-like ionization states of neon, oxygen, nitrogen and carbon. The line centroid energies, measured from the high resolution RGS spectra, are consistent with an origin in outflowing material with a velocity of between ~ 100 - 1000 km s^{-1} . This is in excellent agreement with the average outflow velocity implied from the absorption lines in the UV spectrum of NGC 4151 (~ 450 - 1250 km s^{-1} ; Kriss *et al.* 1995), implying that the UV and X-ray line features originate in the same material. (chapter 6)
 - **The ionization cones of NGC 4151:** Fitting the *XMM-Newton* RGS spectra with a model based on emission from photoionized and photoexcited gas in ionization cones reproduces all of the hydrogen-like and helium-like emission features observed in the spectrum *in detail*. Plasma diagnostics, based on the line ratios of the helium-like triplets and the widths of the RRC (Porquet & Dubau 2000), imply an electron temperature in the ionization cone material of ~ 1 - $5 \times 10^4 \text{ K}$ and electron densities of $\sim 10^8 \text{ cm}^{-3}$ from nitrogen and oxygen and $\sim 10^{10} \text{ cm}^{-3}$ from neon. (chapter 6)
 - **NGC 7582 and Mrk 3. Similar spectra, different variability:** The hard X-ray spectra of NGC 7582 and Mrk 3 are both well described by a simple model incorporating a heavily absorbed power-law continuum, strong Compton reflection (that dominates the spectrum in both sources) and strong iron reprocessing features. Despite this similarity, the characteristics of the variability are strikingly different in the two sources. Mrk 3 varies only on long timescales ($\sim 10^7 \text{ s}$) whereas NGC 7582 shows large scale variability on both extremely short (~ 400 seconds!) and longer timescales ($\sim 10^5 \text{ s}$). In both sources, the long timescale variability may be associated with slow variations in the absorbing column density, in addition to the intrinsic variability of the underlying continuum. (chapter 4)
 - **Ionized Compton reflection:** The observed iron K edge in the X-ray spectrum of NGC 7582 occurs at an energy of 7.2 keV providing strong evidence that the Compton reflection in this source originates from mildly ionized material. The corresponding iron ionization states for this material are in the range of Fe III-Fe V. Under the assumption that NGC 7582 and NGC 4151 are intrinsically similar (*i.e.* that NGC 7582 possesses a heavy warm absorber similar to that seen in NGC 4151) a comparison of the ionization states of iron found in the warm absorber (typically Fe XVI-Fe XXI) and those found in the ionized reflector suggests that the ionized reflecting material in NGC 7582 is either a factor of ~ 30 times more distant or is $\sim 10^3$ times denser than the material that constitutes the heavy warm absorber observed directly in NGC 4151. (chapter 4)

- **The nuclear starburst in NGC 4945:** The reprocessed X-ray emission from the AGN in NGC 4945 is overshadowed by the thermal emission from a nuclear starburst. The starburst emission dominates the X-ray spectrum out to ~ 6 keV and the direct underlying AGN continuum is not observed directly below ~ 10 keV due to heavy intrinsic absorption ($\sim 4 \times 10^{24}$ cm $^{-2}$), making the characterization of the 2-10 keV AGN emission extremely problematic. In addition to the thermal emission from the starburst, *Chandra* imaging of NGC 4945 reveals an X-ray plume with a limb-brightened morphology, whose properties suggest a physical interpretation as a mass-loaded superwind, driven by the nuclear starburst. (chapter 5)
- **The strength of Compton reflection:** The 2-10 keV luminosities of the Compton reflection components in NGC 7582 and Mrk 3 correspond, respectively, to $\sim 8\%$ and $\sim 5\%$ of their unabsorbed continuum luminosities in this range. The similarity of these values to the range of values found for NGC 4151 (2%-11% - chapter 3) and NGC 5548 ($\sim 9\%$ - K. Pounds, Priv. Comm.) implies that a cold Compton reflection component of around this strength may be a ubiquitous component of the X-ray spectra of all types of AGN, even in sources with little direct absorption. (chapter 4)
- **The unified AGN picture:** The analyses of the X-ray spectra from the four obscured Seyfert galaxies presented in this thesis are generally consistent with the unified AGN picture (chapter 1). The wealth of detail provided by these observations, particularly by the observations from *XMM-Newton*, has revealed details unique to each source [*e.g.* the iron overabundance in NGC 4151 (chapter 3) and the Compton reflection from mildly ionized material in NGC 7582 (chapter 4)] however, despite this, the general representation of the X-ray properties of these sources remains highly compatible with the unified AGN picture, in which the major differences between AGN are a result of their orientations to our line-of-sight.

7.3 Five questions for the future

- **Is there really a “torus”?**

The putative molecular torus, as depicted in the unified AGN model (Figure 1.10), is the assumed origin for any significant absorption intrinsic to an AGN, however this theoretical picture may not be a good representation of the real situation. Currently, the properties of the observed X-ray absorption, particularly its geometry and morphology, are extremely poorly defined however, significant progress in defining some of the more secondary properties of the absorbing material (*i.e.* the ionization state, elemental abundance, etc) is likely to be made in the near future.

In particular, the homogeneity of the absorbing material has been a topic of considerable debate for many years, with strong arguments for both a clumpy absorbing medium and a more homogeneous absorbing medium. Observations of sources with large absorbing column densities that do not vary (*e.g.* Mrk 3) are suggestive of a smooth distribution of material or the presence of a

large number of small clouds, such that the total absorption does not vary significantly as a single cloud passes across the line-of-sight. Conversely, observations of sources where the absorption varies on shorter ($\sim 10^5$ s) timescales can be interpreted either as a smooth ionized medium, responding to changes in ionizing flux, or as absorption by a few, larger, dense clouds. The analysis of NGC 4151, presented here in chapter 3, provides considerable evidence for a relatively smooth ionized absorber. However, recent *XMM-Newton* and *RXTE* observations of NGC 3227 provide strong evidence for absorption by individual clouds (Lamer, Uttley & McHardy 2002). This observation revealed an unusual spectral hardening, lasting a few months, that was not accompanied by any changes in the underlying continuum flux and the authors interpret this as the result of a single broad line region cloud transiting across the direct line-of-sight to the central X-ray source. The cloud is constrained to be within ~ 100 light-days of the central X-ray source and has a column density that is extremely comparable to the column densities observed in heavily obscured Seyferts ($N_H \sim 2.5 \times 10^{23} \text{ cm}^{-2}$). Forthcoming *XMM-Newton* and *Chandra* observations of heavily obscured AGN, in particular observations of those that show complex absorption, are planned and are expected to yield increasingly more definite conclusions regarding the nature of X-ray absorption in AGN. One of the key future developments that will impact on this particular issue is the proposed imaging all-sky X-Ray monitor, *LOBSTER*[†]. To be mounted on the International Space Station, *LOBSTER* will observe an extremely large area of the sky every 90 minutes providing a unique census of the variability properties of a wide range of astronomical X-ray sources. Such continuous monitoring is ideal for searching for transition events in AGN, similar to that observed in NGC 3227, and the commonality of these events will be an indicator of the role they play in the X-ray absorption of AGN.

In the future it may also be possible to begin to determine the most important property of the absorbing medium; namely its geometry. *INTEGRAL* observations will play a crucial role in this, especially in those AGN those with relatively small column densities. In these sources high energy X-ray data (> 10 keV) is essential for determining the properties of the Compton reflection originating in the cold absorbing material. Further in the future, direct imaging of the absorbing material in nearby AGN, with observations from near-IR/optical interferometers (*e.g.* the Keck and VLT optical interferometers and the IOTA infra-red interferometer, etc), will hopefully provide a direct determination the existence of the putative molecular torus and will be a stringent test of the specific geometry of the absorbing material that is intrinsic to the unified AGN picture. Such observations, if successful, would also reveal the details of the inner and outer boundaries of the absorbing material and place the first direct constraints on the scale height and inclination of the torus.

- **Is the heavy warm absorber seen in NGC 4151 intrinsic to the unified AGN picture, or is it unique to NGC 4151?**

Assuming NGC 4151 is not a unique source, the complex absorption revealed by the hard X-ray spectrum becomes intrinsic to the unified AGN picture. However, the presence of this component

[†]<http://www.src.le.ac.uk/lobster/>

remains uncertain in the majority of observed AGN and this rarity implies either that it is only sampled by a small range of viewing angles or that it is unique to a small number of sources.

In a recent paper, Krolik & Kriss (2001) discuss how evaporation from the inner edge of the obscuring torus could give rise to a photoionized wind in which a broad range of ionization states coexist in equilibrium. Krolik & Kriss go on to associate this wind with the highly ionized warm absorbers seen in type 1 Seyfert galaxies (and which, in chapter 6, I link with material in ionization cones). Tentatively relating the heavy warm absorber seen in NGC 4151 with such a multi-temperature wind close to the torus (*i.e.* something like a thick, outflowing, ionized skin on the inner edge of the molecular torus), and the ionized gas responsible for the warm absorption in Seyfert 1 galaxies with the same wind, but at a greater distance from the torus, results in a picture that is compatible with both the observational constraints of NGC 4151 and with the absorption observed in other Seyferts. In this picture, the unusually complex character of the absorption observed in NGC 4151 is due to a line-of-sight that grazes both the top edge of the obscuring torus (light column density of cold absorption) and the ionized, multi-temperature wind evaporating off the inner edge of the torus (the heavier column density warm absorber). In essence, the inclination of NGC 4151 presents us with an intermediate viewing angle between the inclinations responsible for classical Seyfert 1 galaxies (in which the absorption is predominantly due to the rarefied multi-temperature wind) and Seyfert 2 galaxies (where the cooler material of the obscuring torus dominates).

Currently this hypothesis remains unconfirmed and verifying this picture is somewhat problematic. The first step in determining the ubiquity of such a heavy warm absorber is to observe a larger sample of sources with similar X-ray spectra to NGC 4151. Markarian 6 is a promising example of a Seyfert galaxy with a qualitatively similar X-ray spectrum to NGC 4151, and hopefully the analysis of *XMM-Newton* observations of this source will yield a second example of a heavy warm absorber in an intermediate Seyfert galaxy.

- **Where are iron $K\alpha$ lines produced in AGN?**

There is a growing body of evidence that suggests that iron reprocessing features, in particular iron $K\alpha$ line emission, are ubiquitous characteristics of the X-ray spectra of AGN. There are several possible origins for this line emission, some of which are readily distinguishable from the properties of the iron $K\alpha$ line however, some of the locations in which the line emission can arise are considerably more difficult to differentiate between.

The iron $K\alpha$ line profiles in the majority of AGN, and in all of the objects presented here, are intrinsically narrow (or near-narrow), suggesting an origin some distance from the central X-ray source. Although much of the narrow line emission can be associated with reprocessing in the putative molecular torus, tentative evidence from the spectral and temporal analysis of NGC 4151 presented here suggests that a significant fraction of the narrow iron $K\alpha$ line emission originates from optically-thin, neutral, material closer to the central X-ray source than the inner region of the torus. Relativistically broadened iron $K\alpha$ line emission, similar to that found by Fabian *et al.* (2002) in a long *XMM-Newton* observation MGC-6-30-15, clearly originates from a region extremely close

to the central supermassive black hole however, in *XMM-Newton* and *Chandra* observations, such broad line features are turning out to be both rare and complex.

The future looks bright for the detailed study of iron $K\alpha$ emission lines. Further observations of AGN with *XMM-Newton* and *Chandra* will continue to reveal sources with distinct narrow line features, building up a large sample of objects with which to study the statistical properties of the narrow line component. Future observations with *XMM-Newton* and *Chandra* are also likely to reveal more sources with strong broad iron $K\alpha$ line features and increasingly more detailed modelling of both the narrow and broad line profiles, and the line variability, will be an increasingly more powerful diagnostic of the origins of the iron $K\alpha$ lines. Moreover, the study of iron $K\alpha$ lines, particularly relativistically broadened lines, is a priority for future X-ray astronomy missions such as *Constellation-X* and *Xeus*. These powerful observatories will provide excellent quality observations of AGN with extremely high spectral and temporal resolution that, hopefully, will allow the reverberation mapping of detected broad iron $K\alpha$ lines, resulting in detailed information on the mass and spin of the supermassive black hole.

- **Are the ionization cones of AGN homogeneous or clumpy?**

Recent X-ray grating observations of bright, nearby, heavily obscured AGN have revealed that the extended soft X-ray emission in these sources is spatially coincident with the observed optical ionization cones and is composed almost entirely of emission lines and RRC. Many of the properties of the emitting material are well defined by the details of the soft X-ray spectrum, including the ionization state, the temperature and the outflow velocity however, the homogeneity of the outflowing material is not clearly determined by current observations.

The details of the soft X-ray spectrum of NGC 4151, presented in chapter 6, imply electron densities in the ionization cones of this source of $\sim 10^8 \text{ cm}^{-3}$ (from the nitrogen and oxygen lines) and $\sim 10^{10} \text{ cm}^{-3}$ (from the neon lines). The discrepancy between these densities can be interpreted as the result of relative abundance differences however, it could be the first indications that the material in the ionization cones may have a clumpy, non-uniform, distribution. The real situation is likely to be somewhat complex, possibly being some combination of small dense clouds and a smoother, less dense, medium. The BLR and NLR clouds are obvious structures that can be associated with the small dense clouds in this picture and it has been suggested that the evaporation of these clouds, in a similar fashion to that suggested by Krolik & Kriss (1995) for the evaporation of the inner edge of the putative torus, may well be responsible for the less dense material in the ionization cones (Netzer 2002).

Future imaging observations of extended soft X-ray emission in heavily obscured AGN, particularly with the sub-microarcsecond X-ray imaging capabilities of future mission such as *MAXIM*, will provide an unprecedented view of the morphological complexity of the X-ray ionization cones in these sources. These observations, along with increasingly higher quality X-ray grating spectra, either from repeated observations with *Chandra* and *XMM-Newton* or from the grating instruments on future missions such as *Constellation-X* and *Astro-E2*, will be key diagnostics in determining

the detailed composition and morphology of the ionization cone material.

- **Can we reconcile X-ray observations of heavily obscured AGN with observations at other wavelengths?**

One of the major challenges for the future study of heavily obscured AGN is to reconcile the source properties inferred from X-ray observations with those inferred from other wavelength observations, particularly with observations in the UV and optical bands. In many sources the gross properties determined from the relatively low spatial and spectral resolution X-ray data are already in good agreement with the UV and optical observations (*e.g.* Mrk 3 - Kishimoto *et al.* 2002; Mrk 501 - Kondo *et al.* 1981) however, in some of the more complex sources (*i.e.* intermediate Seyferts like NGC 4151 - Chapter 3) the UV and optical properties are not well matched with the X-ray properties.

NGC 4151 is an excellent example of this problem. The UV absorbing column, measured from the UV absorption line spectrum (Kriss *et al.* 1995), is at least two orders of magnitude smaller than that implied from the hard X-ray spectra. In contrast, the properties of the soft X-ray emission lines detected by the *XMM-Newton* RGS instruments are in good agreement with the absorption lines in the UV spectrum (Kriss *et al.* 1995) and are also in good agreement with the properties of the extended [O III] emission (Ogle *et al.* 2000). The optical spectrum of the Seyfert nucleus in NGC 4151, on the other hand, shows considerable broad line emission (Sergeev, Pronik & Sergeeva 2001) that implies a direct view of the broad line region, located close to the central X-ray source. Such a direct line of sight is incompatible with the heavy obscuration that is *required* by the hard X-ray spectrum. Optical polarimetry observations of NGC 4151 serve to complicate the situation even further, revealing broad polarized emission lines with complex profiles that vary on short timescales (D. Axon, Priv. Comm.).

Clearly the real situation is complex but, with detailed X-ray observations from *XMM-Newton*, *Chandra* and improved UV observations from instruments such as the *HST* STIS, progress is beginning to be made (Kraemer *et al.* 2002). It remains a challenge for future research to combine the detailed information from improved observations at all wavelengths, to produce a consistent unified picture of AGN.

References

- Antonucci, R. R. J. & Miller, J., 1985. *Astrophys. J.*, **297**, 621.
- Antonucci, R. R. J., 1982. *Ph.D. Thesis*, .
- Antonucci, R. R. J., 1983. *Nature*, **303**, 158.
- Antonucci, R. R. J., 1984. *Astrophys. J.*, **278**, 499.
- Antonucci, R. R. J., 1993. *Ann. Rev. Astron. Astrophys.*, **31**, 473.
- Awaki, H., Koyama, K., Kunieda, H. & Tawara, Y., 1990. *Nature*, **346**, 544.
- Awaki, H., Koyama, K., Inoue, H. & Halpern, J. P., 1991a. *Pub. Astr. Soc. Japan.*, **43**, 195.
- Awaki, H., Kunieda, H., Tawara, Y. & Koyama, K., 1991b. *Pub. Astr. Soc. Japan.*, **43**, L37.
- Bassani, L., Dadina, M., Maiolino, R., Salvati, M., Risaliti, G., Ceca, R. D., Matt, G. & Zamorani, G., 1999. *Astrophys. J. Suppl.*, **121**, 473.
- Behar, E., Rasmussen, A. P., Griffiths, R. G., Dennerl, K., Audard, M., Aschenbach, B. & Brinkman, A. C., 2001. *Astr. Astrophys.*, **365**, L242.
- Boella, G., Chiappetti, L., Conti, G., Cusumano, G., del Sordo, S., Rosa, G. L., Maccarone, M. C., Mineo, T., Molendi, S., Re, S., Sacco, B. & Tripiciano, M., 1997. *Astr. Astrophys. Suppl.*, **122**, 327.
- Cappi, M., Bassani, L., Comastri, A., Guainazzi, M., Maccararo, T., Malaguti, G., Matt, G., Palumbo, G. G. C., Blanco, P., Dadina, M., dal Fiume, D., di Cocco, G., Fabian, A. C., Frontera, F., Maiolino, R., Piro, L., Trifoglio, M. & Zhang, N., 1999. *Astr. Astrophys.*, **344**, 857.
- Carroll, B. W. & Ostlie, D. A., 1996. *An introduction to modern astrophysics*, Reading, Mass. : Addison-Wesley Pub., c1996.
- Chen, Y. & Huang, J., 1997. *Astrophys. J. Letts.*, **479**, L23.
- Compton, A. H., 1923a. *Phys. Rev.*, **21**, 483.
- Compton, A. H., 1923b. *Phys. Rev.*, **22**, 409.
- Cooke, B. A., Elvis, M., Ward, M. J., Fosbury, R. A. E., Penston, M. V. & Maccararo, T., 1976. *Mon. Not. R. astr. Soc.*, **177**, 121P.
- Curran, S. J., Johansson, L. E. B., Bergman, P., Heikkilä, A. & Aalto, S., 2001. *Astr. Astrophys.*, **367**, 457.
- Chandra Proposers' Guide*. 2002.

- XMM-Newton Users' Handbook*. 2002.
- Done, C., Madejski, G. M. & Smith, D. A., 1996. *Astrophys. J. Letts.*, **463**, 63.
- Dubau, J. & Porquet, D., 2002. In: *The proceedings of the symposium 'New Visions of the X-ray Universe in the XMM-Newton and Chandra Era', November 2001*, p. 4049.
- Edelson, R., Turner, T., Pounds, K., Vaughan, S., Markowitz, A., Marshall, H., Dobbie, P. & Warwick, R. S., 2002. *Astro-ph*, **0108387**.
- Einstein, A., 1905. *Annalen der Physik*. "On a Heuristic Viewpoint Concerning the Production and Transformation of Light.", **17**, .
- Elvis, M. & Lawrence, A., 1988. *Astrophys. J.*, **331**, 161.
- Elvis, M., Briel, U. G. & Henry, J. P., 1983. *Astrophys. J.*, **268**, 105.
- Evans, I. N., Tsvetanov, Z., Kriss, G. A., Ford, H. C., Caganoff, S. & Koratkar, A. P., 1993. *Astrophys. J.*, **417**, 82.
- Fabian, A. C., Rees, M. J., Stella, L. & White, N. E., 1989. *Mon. Not. R. astr. Soc.*, **238**, 729.
- Fabian, A. C., Iwasawa, K., Reynolds, C. S. & Young, A. J., 2000. *Pub. Astr. Soc. Pacific.*, **112**, 1145.
- Fabian, A. C., Vaughan, S., Nandra, K., Iwasawa, K., Ballantyne, D. R., Lee, J. C., Rosa, A. D., Turner, A. & Young, A., 2002. *Mon. Not. R. astr. Soc.*, **335**, L1.
- Feldmeier, J., Brandt, W., Elvis, M., Fabian, A., Iwasawa, K. & Mathur, S., 1999. *Astrophys. J.*, **510**, 167.
- Fiore, F., Perola, G. C. & Romano, M., 1990. *Mon. Not. R. astr. Soc.*, **243**, 522.
- Foschini, L., Panessa, F., Longinotti, A. L., Ho, L. C., Cappi, L. B. M., Dadina, M., Malaguti, G., Cocco, G. D., Gianotti, F., Stephen, J. B. & Trifoglio, M., 2002. In: *astro-ph/0209098*, p. 0.
- Frontera, F., Costa, E., Fiume, D., Feroci, M., Nicastro, L., Orlandini, M., Palazzi, E. & Zavattini, G., 1997. *Proc. SPIE Vol. 3114*, p. 206-215, *EUV, X-Ray, and Gamma-Ray Instrumentation for Astronomy VIII, Oswald H. Siegmund; Mark A. Gummin; Eds.*, **3114**, 206.
- Gabriel, A. H. & Jordan, C., 1969. *Mon. Not. R. astr. Soc.*, **145**, 241.
- Georgantopoulos, I., Papadakis, I., Warwick, R. S., Smith, D. A., Stewart, G. C. & Griffiths, R. G., 1999. *Mon. Not. R. astr. Soc.*, submitted.
- George, I. M. & Fabian, A. C., 1991. *Mon. Not. R. astr. Soc.*, **249**, 352.
- Ghisellini, G., Haardt, F. & Matt, G., 1994. *Mon. Not. R. astr. Soc.*, **267**, 743.
- Greenhill, L., Moran, J. M. & Herrnstein, J. R., 1997. *Astrophys. J.*, **481**, L23.

- Griffiths, R. G., Warwick, R. S., Georgantopoulos, I., Done, C. & Smith, D. A., 1998. *Mon. Not. R. astr. Soc.*, **298**, 1159.
- Griffiths, R. G., 1999. *Ph.D. Thesis*, .
- Guainazzi, M., Matt, G., Brandt, W. N., Antonelli, L. A., Barr, P. & Bassani, L., 2000. *Astr. Astrophys.*, **356**, 463.
- Guainazzi, M., Matt, G., Fiore, F. & Perola, G. C., 2002. **388**, 787.
- Gursky, H., Kellogg, E. M., Leong, C., Tananbaum, H. & Giacconi, R., 1971. *Astrophys. J. Letts.*, **165**, 43.
- Haardt, F. & Maraschi, L., 1993. *Astrophys. J.*, **413**, 507.
- Hanson, C. G., Skinner, G. K., Eyles, C. J. & Wilmore, A. P., 1990. *Mon. Not. R. astr. Soc.*, **242**, 262.
- Heckman, T. M., Armus, L. & Miley, G. K., 1990. *Astrophys. J. Suppl.*, **74**, 833.
- Hesser, J. E., Harris, H. C., Bergh, S. V. D. & Harris, G. L. H., 1984. *Astrophys. J.*, **276**, 491.
- Holt, S. S., Mushotzky, R. F., Boldt, E. A., Serlemitsos, P. J., Becker, R. H., Szymkowiak, A. E. & White, N. E., 1980. *Astrophys. J. Letts.*, **241**, L13.
- Iwasawa, K., Koyama, K., Awaki, H., Kunieda, H., Makishima, K., Tsuru, T., Ohashi, T. & Nakai, N., 1993. *Astrophys. J.*, **409**, 155.
- Iwasawa, K., Yaqoob, T., Awaki, H. & Ogasaka, Y., 1994. *Pub. Astr. Soc. Japan.*, **46**, L167.
- Jansen, F., Lumb, D., Altieri, B., Clavel, J., Ehle, M., Erd, C., andM. Guainazzi, C. G., Gondoin, P., Much, R., Munoz, R., Santos, M., Schartel, N., Texier, D. & Vacanti, G., 2001. *Astr. Astrophys.*, **365**, L1.
- Johnson, W. N. *et al.*, 1997. *Astrophys. J.*, **482**, 173.
- Kallman, T. R. & Krolik, J. H. *XSTAR: A Spectral Analysis Tool. Version 1.40 of the User's Guide.* 1997.
- Kinkhabwala, A., Sako, M., Behar, E., F.Paerels, Kahn, S. M., Brinkman, A. C., Kaastra, J. S., van der Meer, R., Gu, M. F. & Liedahl, D. A., 2002. *Astrophys. J.*, **575**, 732.
- Kishimoto, M., Kay, L., Antonucci, R., Hurt, T. W., Cohen, R. D. & Krolik, J. H., 2002. *Astrophys. J.*, **565**, 155.
- Kondo, Y., Worrall, D. M., Mushotzky, R. F., Hackney, R. L., Hackney, K. R. H., Oke, J. B., Yee, H. K. C., Neugebauer, G., Matthews, K., Feldman, P. A. & Brown, R. L., 1981. *Astrophys. J.*, **243**, 690.

- Kraemer, S. B., Crenshaw, D. M., George, I. M., Netzer, H., Turner, T. J. & Gabel, J. B., 2002. *Astrophys. J.*, **577**, 98.
- Kriss, G. A., Canizares, C. R. & Ricker, G. R., 1980. *Astrophys. J.*, **242**, 492.
- Kriss, G. A., Davidsen, A. F., Zheng, W., Kruk, J. W. & Espey, B. R., 1995. *Astrophys. J. Letts.*, **454**, 7.
- Krolik, J. H. & Kallman, T. R., 1984. *Astrophys. J.*, **286**, 366.
- Krolik, J. H. & Kriss, G., 1995. *Astrophys. J.*, **447**, 512.
- Krolik, J. H. & Kriss, G., 2001. *Astrophys. J.*, **561**, 684.
- Krolik, J. H., Madau, P. & Życki, P. T., 1994. *Astrophys. J. Letts.*, **420**, 57.
- Kukula, M. J., Ghosh, T., Pedlar, A., Schilizzi, R. T., Miley, G. K., de Bruyn, A. G. & Saikia, D. J., 1993. *Mon. Not. R. astr. Soc.*, **264**, 893.
- Lamer, G., Uttley, P. & McHardy, I. M., 2002. *In Prep.*, **000**, 000.
- Lawrence, A. & Elvis, M., 1982. *Astrophys. J.*, **256**, 410.
- Lawrence, A., 1987. *Pub. Astr. Soc. Pacific.*, **99**, 309.
- Liedahl, D. A. & Paerels, F., 1996. *Astrophys. J. Letts.*, **468**, 33.
- Liedahl, D. A., Osterheld, A. L. & Goldstein, W. H., 1995. *Astrophys. J. Letts.*, **438**, 115.
- van Paradijs, J. & Bleeker, J. A. M., eds. *X-Ray Spectroscopy in Astrophysics*, 1999.
- Longair, C., 1997. *High Energy Astrophysics. Vol.1. Particles, Photons and their Detection*, 2nd Edn., Cambridge University Press, Cambridge.
- Magdziarz, P. & Zdziarski, A. A., 1995. *Mon. Not. R. astr. Soc.*, **273**, 837.
- Magorrian, J., Tremaine, S., Richstone, D., Bender, R., Bower, G., Dressler, A., Faber, S. M., Gebhardt, K., Green, R., Grillmair, C., Kormendy, J. & Lauer, T., 1998. *Astron. J.*, **115**, 2285.
- Maisack, M. & Yaqoob, T., 1991. *Astr. Astrophys.*, **249**, 25.
- Matt, G., Brandt, W. N. & Fabian, A. C., 1996. *Mon. Not. R. astr. Soc.*, **280**, 823.
- Matt, G., Guainazzi, M., Maiolino, R., S.Molendi, Perola, G. C., Antonelli, L. A., Bassani, L., Brandt, W. N., Fabian, A. C., Fiore, F., Iwasawa, K., Malaguti, G., Marconi, A. & Poutanen, J., 1999. *Astr. Astrophys.*, **341**, L39.
- Matt, G., Fabian, A. C., Guainazzi, M., Iwasawa, K., Bassani, L. & Malaguti, G., 2000. *Mon. Not. R. astr. Soc.*, **318**, 173.
- Matt, G., Perola, G. C. & Piro, L., 1991. *Astr. Astrophys.*, **247**, 25.

- Miller, J. S. & Antonucci, R. R. J., 1983. *Astrophys. J. Letts.*, **271**, 7.
- Miller, J. S. & Goodrich, R. W., 1990. *Astrophys. J.*, **355**, 456.
- Miller, J. S., Goodrich, R. W. & Mathews, W. G., 1991. *Astrophys. J.*, **378**, 47.
- Moorwood, A. F. M. & Oliva, E., 1990. *Astr. Astrophys.*, **239**, 78.
- Moorwood, A. F. M., Werf, P. V. D., Kotilainen, J. K., Marconi, A. & Oliva, E., 1996. *Astr. Astrophys.*, **308**, L1.
- Morrison, R. & McCammon, D., 1983. *Astrophys. J.*, **270**, 119.
- Morse, J. A., Wilson, A. S., Elvis, M. & Weaver, K. A., 1995. *Astrophys. J.*, **439**, 121.
- Mulchaey, J. S., Mushotzky, R. F. & Weaver, K. A., 1992. *Astrophys. J. Letts.*, **390**, 69.
- Nandra, K. & Pounds, K. A., 1994. *Mon. Not. R. astr. Soc.*, **268**, 405.
- Nandra, K., George, I. M., Mushotsky, R. F., Turner, T. J. & Yaqoob, T., 1997. *Astrophys. J.*, **476**, 70.
- Nayakshin, S. & Kazanas, D., 2001. *Astrophys. J. Letts.*, **553**, L141.
- Netzer, H., 2002. In: *Active Galactic Nuclei: from Central Engine to Host Galaxy Abstract Book, meeting held in Meudon, France, July 23-27, 2002, Eds.: S. Collin, F. Combes and I. Shlosman. To be published in ASP (Astronomical Society of the Pacific), Conference Series, p. 20.*
- Nicastro, F., Fiore, F., Perola, G. C. & Elvis, M., 1999. *Astrophys. J.*, **512**, 184.
- Ogle, P. M., Marshall, H. L., Lee, J. C. & Canizares, C. R., 2000. *Astrophys. J. Letts.*, **545**, L81.
- Osterbrock, D. E., 1978. *Phys. Scripta*, **17**, 285.
- Ott, M., 1995. *Atomic and molecular gas in the starburst galaxy NGC 4945*, Bonn: Rheinische Friedrich-Wilhelms-Universitaet, —c1995.
- Parmar, A. N., Martin, D. D. E., Bavdaz, M., Favata, F., Kuulkers, E., Vacanti, G., Lammers, U., Peacock, A. & Taylor, B. G., 1997. *Astr. Astrophys. Suppl.*, **122**, 309.
- Perola, G. C. *et al.*, 1986. *Astrophys. J.*, **306**, 508.
- Petrucci, P. O., Haardt, F., Maraschi, L., Grandi, P., Matt, G., Nicastro, F., Piro, L., C., G. C. P. G. & Rosa, A. D., 2000. *Astrophys. J.*, **540**, 131.
- Pietsch, W. & Read, A. M., 2002. **384**, 793.
- Pietsch, W., Roberts, T. P., Sako, M., Freyberg, M. J., Read, A. M., Borozdin, K. N., Branduardi-Raymont, G., Cappi, M., Ehle, M., Ferrando, P., Kahn, S. M., Ponman, T. J., Ptak, A., Shirey, R. E. & Ward, M., 2001. *Astr. Astrophys.*, **365**, L174.

- Piro, L., Nicasto, F., Perola, G., Capalbi, M., Cappi, M., Grandi, P., Maraschi, L. & Petrucci, P., 2002. *Astr. Astrophys.*, **In preparation**, 000.
- Pogge, R. W. & De Robertis, M. M., 1993. *Astrophys. J.*, **404**, 563.
- Porquet, D. & Dubau, J., 2000. **143**, 495.
- Porquet, D., Mewe, R., Kaastra, J., Dubau, J. & Raassen, A., 2002. *Astro-ph*, **0204119**.
- Pozdnyakov, L., Sobol, I. & Sunyaev, R., 1983. *Astr. and Space Phys. Rev.*, **2**, 189.
- Pradhan, A. K., Norcross, D. W. & Hummer, D. G., 1981. *Astrophys. J.*, **246**, 1031.
- Protassov, R., van Dyk, D. A., Connors, A., Kashyap, V. L. & Siemiginowskac, A., 2002. *Astrophys. J.*, **571**, 545.
- Rees, M. J., 1984. *Ann. Rev. Astron. Astrophys.*, **22**, 471.
- Reeves, J. N., O'Brien, P. T., Vaughan, S., Law-Green, D., Ward, M., Simpson, C., Pounds, K. A. & Edelson, R., 2000. *Mon. Not. R. astr. Soc.*, **312**, L17.
- Reynolds, C. S., 1997. *Mon. Not. R. astr. Soc.*, **286**, 513.
- Richtmyer, F. K., Kennard, E. H. & Lauritsen, T., 1955. *Introduction to modern physics*, McGraw-Hill Book Company.
- Risaliti, G., Maiolino, R. & Salvati, M., 1999. *Astrophys. J.*, **522**, 157.
- Risaliti, G., 2002. *Astr. Astrophys.*, **386**, 379.
- Rowan-Robinson, M., 1977. *Astrophys. J.*, **213**, 638.
- Sako, M., Kahn, S. M., Paerels, F. & Liedahl, D. A., 2000. *Astrophys. J. Letts.*, **543**, L115.
- Sambruna, R. M., Netzer, H., Kaspi, S., Brandt, W. N., Chartas, G., Garmire, G. P., Nousek, J. A. & Weaver, K. A., 2001. *Astrophys. J. Letts.*, **546**, L13.
- Schachter, J. F., Fiore, F., Elvis, M., Mathur, S., Wilson, A. S., Morse, J. A., Awaki, H. & Iwasawa, K., 1998. *Astrophys. J. Letts.*, **503**, L123.
- Schmidt, M., Hasinger, G., Gunn, J., Schneider, D., Burg, R., Giacconi, R., Lehmann, I., MacKenty, J., Trumper, J. & Zamorani, G., 1998. *Astr. Astrophys.*, **329**, 495.
- Schurch, N. J. & Warwick, R. S., 2002. *Mon. Not. R. astr. Soc.*, **334**, 811.
- Sergeev, V. I., Pronik, S. G. & Sergeeva, E. A., 2001. **554**, 245.
- Smith, D. A. & Done, C., 1996. *Mon. Not. R. astr. Soc.*, **280**, 355.
- Snowden, S. L., 2002. In: *Proceedings of the ESTEC Symposium 'New Visions of the X-ray Universe in*

the XMM-Newton and Chandra Era', p. 3311.

- Spoon, H. W. W., Koornneef, J., Moorwood, A. F. M., Lutz, D. & Tielens, A. G. G. M., 2000. *Astr. Astrophys.*, **357**, 898.
- Strickland, D. K., Heckman, T. M., Weaver, K. A. & Dahlem, M., 2000. *Astron. J.*, **120**, 2965.
- Strüder, L., Briel, U., Dennerl, K., Hartmann, R., Kendziorra, E., Meidinger, N., Pfeffermann, E., Reppin, C., Aschenbach, B., Bornemann, W., Bräuninger, H., Burkert, W., Elender, M., Freyberg, M., Haberl, F., Hartner, G., Heuschmann, F., Hippmann, H., Kastelic, E., Kemmer, S., Kettenring, G., Kink, W., Krause, N., Müller, S., Oppitz, A., Pietsch, W., Popp, M., Predehl, P., Read, A., Stephan, K. H., Stötter, D., Trümper, J., Holl, P., Kemmer, J., Soltau, H., Stötter, R., Weber, U., Weichert, U., von Zanthier, C., Carathanassis, D., Lutz, G., Richter, R. H., Solc, P., Böttcher, H., Kuster, M., Staubert, R., Abbey, A., Holland, A., m. Turner, Balasini, M., Bignami, G. F., Palombara, N. L., Villa, G., Buttler, W., Gianini, F., Lainé, R., Lumb, D. & Dhez, P., 2001. *Astr. Astrophys.*, **365**, L18.
- Takahashi, K., Inoue, H. & Dotani, T., 2002. *Pub. Astr. Soc. Japan.*, **54**, 373.
- Tanaka, Y. *et al.*, 1995. *Nature*, **375**, 659.
- Terashima, Y., Ho, L. C. & Ptak, A. F., 2000. *Astrophys. J.*, **539**, 161.
- Tran, H. D., Miller, J. S. & Kay, L. E., 1992. *Astrophys. J.*, **397**, 452.
- Turner, T. J. & Pounds, K. A., 1989. *Mon. Not. R. astr. Soc.*, **240**, 833.
- Turner, T. J., George, I. M., Nandra, K. & Mushotzky, R., 1997a. *Astrophys. J. Suppl.*, **113**, 23.
- Turner, T. J., George, I. M., Nandra, K. & Mushotzky, R., 1997b. *Astrophys. J.*, **488**, 164.
- Turner, T. J., George, I. M., Nandra, K. & Mushotzky, R., 1998. *Astrophys. J.*, **493**, 91.
- Turner, T. J., Perola, G. C., Fiore, F., Matt, G., George, I., Piro, L. & Bassani, L., 2000. *Astrophys. J.*, **531**, 245.
- Turner, M. J. L., Abbey, A., Arnaud, M., Balasini, M., Barbera, M., Belsole, E., Bennie, P. J., Bernard, J. P., Bignami, G. F., Boer, M., Briel, U., Butler, I., Cara, C., Chabaud, C., Cole, R., Collura, A., Conte, M., Cros, A., Denby, M., Dhez, P., Coco, G. D., Dowson, J., Ferrando, P., Ghizzardi, S., Gianotti, F., Goodall, C. V., Gretton, L., Griffiths, R. G., Hainaut, O., Hochedez, J. F., Holland, A. D., Jourdain, E., Kendziorra, E., Lagostina, A., Laine, R., Palombara, N. L., Lortholary, M., Lumb, D., Marty, P., Molendi, S., Pigot, C., Poindron, E., Pounds, K. A., Reeves, J. N., Reppin, C., Rothenflug, R., Salvétat, P., Sauvageot, J. L., Schmitt, D., Sembay, S., Short, A. D. T., Spragg, J., Stephen, J., Strüder, L., Tiengo, A., m. Trifoglio, Trümper, J., Vercellone, S., Vigroux, L., Villa, G., Ward, M. J., Whitehead, S. & Zonca, E., 2001a. *Astr. Astrophys.*, **365**, L27.

- Turner, T. J., Romano, P., George, I. M., Edelson, R., Collier, S. J., Mathur, S. & Peterson, B., 2001b. *Astrophys. J.*, **561**, 131.
- Ulrich, M., 2000. *Astr. Astrophys.*, **10**, 135.
- Urry, C. M. & Padovani, P., 1995. *Pub. Astr. Soc. Pacific.*, **107**, 803.
- Vainshtein, L. A. & Safronova, U., 1978. *Atomic Data and Nuclear Data Tables*, **21**, 49+.
- Vignali, C. & Comastri, A. R., 2002. *Astr. Astrophys.*, **381**, 834.
- Wang, J., Wang, T. & Zhou, Y., 2001. *Astrophys. J.*, **549**, 891.
- Wang, J., Zhou, Y. & Wang, T., 1999. *Astrophys. J. Letts.*, **523**, L129.
- Wardziński, G. & Zdziarski, A. A., 2001. *Mon. Not. R. astr. Soc.*, **325**, 963.
- Warwick, R. S., Done, C. & Smith, D. A., 1995. *Mon. Not. R. astr. Soc.*, **275**, 1003.
- Warwick, R. S., Koyama, K., Inoue, H., Takano, S., Awaki, H. & Hoshi, R., 1989. *Pub. Astr. Soc. Japan.*, **41**, 739.
- Warwick, R. S., Sembay, S., Yaqoob, T., Maishima, K., Ohashi, T., Tashiro, M. & Kohmura, Y., 1993. *Mon. Not. R. astr. Soc.*, **265**, 412.
- Warwick, R. S., Smith, D. A., Yaqoob, T., Edelson, R., Johnson, W. N., Reichert, G. A., Clavel, J., Magdziarz, P., Peterson, B. M. & Zdziarski, A. A., 1996. *Astrophys. J.*, **470**, 349.
- Warwick, R. S., P. Bernard, J., Bocchino, F., Decourchelle, A., Ferrando, P., Griffiths, R. G., Haberl, F., Palombara, N. L., Lumb, D., Mereghetti, S., Read, A. M., Schaudel, D., Schurch, N., Tiengo, A. & Willingale, R., 2001. **365**, L248.
- Weaver, K. A. *et al.*, 1994a. *Astrophys. J.*, **423**, 621.
- Weaver, K. A., Yaqoob, T., Holt, S. S., Mushotzky, R. F., Matsuoka, M. & Yamauchi, M., 1994b. *Astrophys. J. Letts.*, **436**, 27.
- Weaver, K. A., Gelbord, J. & Yaqoob, T., 2001. *Astrophys. J.*, **550**, 261.
- Weedman, D. W., 1977. *Ann. Rev. Astron. Astrophys.*, **15**, 69.
- Weisskopf, M. C., Brinkman, B., Canizares, C., Garmire, G., Murray, S. & Van Speybroeck, L. P., 2002. *Pub. Astr. Soc. Pacific.*, **114**, 1.
- Wilms, J., Reynolds, C. S., Begelman, M. C., Reeves, J., Molendi, S., Staubert, R. & Kendziorra, E., 2001. *Mon. Not. R. astr. Soc.*, **328**, L27.
- Wilms, J., 1998. *Ph.D. Thesis*, .

- Wilson, A. S. & Nath, B., 1990. *Astrophys. J. Suppl.*, **74**, 731.
- Wilson, A. S. & Tsvetanov, Z. I., 1994. *Astron. J.*, **107**, 1227.
- Wilson, A. S., Ward, M. J. & Haniff, C. A., 1988. *Astrophys. J.*, **334**, 121.
- Xue, S. J., Otani, C., Mihara, T., Cappi, M. & Matsuoka, M., 1999. *Pub. Astr. Soc. Japan.*, **50**, 519.
- Yang, Y., Wilson, A. & Ferruit, P., 2001. *Astrophys. J.*, **563**, 124.
- Yaqoob, T. & Warwick, R. S., 1991. *Mon. Not. R. astr. Soc.*, **248**, 773.
- Yaqoob, T., Warwick, R. S., Makino, F., Otani, C., Sokoloski, J. L., Bond, I. A. & Yamauchi, M., 1993. *Mon. Not. R. astr. Soc.*, **262**, 435.
- Yaqoob, T., Edelson, R., Weaver, K. A., Warwick, R. S., Mushotzky, R. F., Serlemitsos, P. J. & Holt, S. S., 1995. *Astrophys. J. Letts.*, **453**, 81.
- Yaqoob, T., Padmanabhan, U., Dotani, T. & Nandra, K., 2001. *Astro-ph*, **0112318**, 000.
- Yaqoob, T., Warwick, R. S. & Pounds, K. A., 1989. *Mon. Not. R. astr. Soc.*, **236**, 153.
- Yaqoob, T., 1997. *Astrophys. J.*, **479**, 184.
- Yaqoob, T., 1998. *Astrophys. J.*, **500**, 893.
- Young, A. J., Wilson, A. S. & Shopbell, P. L., 2001. *Astrophys. J.*, **556**, 6.
- Zdziarski, A. A., Fabian, A. C., Nandra, K., Celotti, A., Rees, M. J., Done, C., Coppi, P. S. & Madejski, G. M., 1994. *Mon. Not. R. astr. Soc.*, **269**, 55P.
- Zdziarski, A., M. Leighly, K., Matsuoka, M., Cappi, M. & Mihara, T., 2002. *Astrophys. J.*, **573**, in press.
- Zdziarski, A. A., Johnson, W. N. & Magdziarz, P., 1996. *Mon. Not. R. astr. Soc.*, **283**, 193.
- Zdziarski, A. A., Poutanen, J. & Johnson, W. N., 2000. *Astrophys. J.*, **542**, 703.
- Zycki, G. M. M. P., Done, C., Valinia, A., Blanco, P., Rothschild, R. & Turek, B., 2000. *Astrophys. J. Letts.*, **535**, L87.